Hair Bundle Stiffness in the Turtle Utricle: Structural and Regional Variations

Corrie E. Spoon

Dissertation submitted to the faculty of the Virginia Polytechnic Institute and State University in partial fulfillment of the requirements for the degree of

Doctor of Philosophy
In
Biomedical Engineering

J.W. Grant, Chair
J.R. Cotton
H.C. Gabler
K.P. Granata
J-H. Nam
E.H. Peterson

November 19, 2007
Blacksburg, Virginia

Keywords: hair bundle stiffness, utricle, kinocilium

Hair Bundle Stiffness in the Turtle Utricle: Structural and Regional Variations

Corrie E. Spoon

ABSTRACT

Vestibular hair cells are mechanotransducing sensory receptors in the vertebrate inner ear that detect movement and orientation of the head with respect to gravity. The morphologies of their ciliary bundles vary greatly for different species, endorgans, and within the same endorgan. Bundle morphology in the turtle utricle, like other species, demonstrates highly organized regional variations. These structural differences in bundles impact their mechanical behavior and the process of mechanotransduction. To further understanding of the mechanical behavior of hair bundles, this work experimentally measured the stiffness of bundles with differing morphology, the stiffness contribution of interciliary links and the mechanical properties of the kinocilium in the turtle utricle.

The stiffness of hair bundles of varying structure and location along a medial to lateral transect of the utricle was examined. Bundle stiffness was greatest in the striola and demonstrated a systematic decline with location from the line of polarity reversal. The average stiffness of bundles in the striola and extrastriola were 82 ± 46 (n=48) and 9 ± 5 (n=25) μN/m, respectively. The stiff and weak bundles demonstrated characteristic morphologies. The stiffest bundles have short kinocilium, tall stereocilia, and ratios of kinocilium to tallest stereocilia height (KS) close to 1. In contrast, the compliant bundles have tall kinocilium, short stereocilia, and KS ratios ranging from 1.6 – 8. The stiffer bundles also tend to have longer array lengths and steeper slopes. Measurements of bundle stiffness in the turtle utricle are lower than those previously reported which may be attributed to morphological differences between species.

The stiffness contributions of the interciliary links were also examined through their selective removal with exposure to the Ca^{2+} chelator BAPTA and the protease subtilisin. BAPTA treatment reportedly breaks tip, kinocilial and ankle links while subtilisin breaks the shaft and ankle links. Following BAPTA and subtilisin treatments, bundle stiffness reduced by 65 ± 10% and 63 ± 11%, respectively.

The mechanical properties of the kinocilium were measured with novel techniques. Flexural rigidity (EI) was measure while the kinocilium was fixed at the height of the tallest stereocilia using a glass supporting probe. Through both force deflection and a high speed video technique, measured values of EI ranged from 1460 – 6150 $pN \cdot \mu m^2$. The rotational stiffness of the kinocilium about its apical insertion was also measured. Bundles were treated with BAPTA to break the kinocilial links and separate the kinocilium from neighboring stereocilia. Using a force deflection technique, the rotational stiffness of the kinocilium was measured as 120 ± 17 $pN \cdot \mu m/rad$.

Table of Contents

Table of Contents iii
List of Figures v
List of Tables vii

Chapter 1: Introduction 1
1.1 Turtle Utricle 1
1.2 Regional Organization of the Turtle Utricle 2
1.3 Bundle Morphology 4
1.3.1 Bundle Morphology in Striola Zones 2 and 3 5
1.3.2 Bundle Morphology in Extrastriola Zones 1 and 4 6
1.4 Stiffness Measurements 8
1.4.1 Stiffness MeasurementsWith a Flexible Fiber 8
1.4.2 Bundle Stiffness Calculation 9
1.4.3 Photodiode Sensor 9
1.4.4 Flexible Fibers 11
1.4.5 Variations on the Flexible Fiber Technique 12

Chapter 2: Hair Bundle Stiffness Variation with Structure and Location 14
2.1 Introduction 14
2.2 Methods 15
2.2.1 Preparation 15
2.2.2 Stiffness Measurements 16
2.2.3 Glass Fibers 18
2.2.4 Dimensional Measurements of Bundles 19
2.3 Verification of Measurements 21
2.3.1 Accuracy of the Glass Fiber Calibrations 21
2.3.2 Imitation Bundles 22
2.3.3 Stiffness Measurements Over Time 24
2.3.4 The Impact of Fluid Drag on the Calibration Factor 28
2.3.4.1 Temporal Response of the Fiber Tip 29
2.3.4.2 Calibration Factor at Different Frequencies 31
2.4 Results 34
2.4.1 Stiffness vs. Distance From the LPR 34
2.4.2 Bundle Morphology vs. Distance From the LPR 36
2.4.3 Bundle Stiffness vs. Morphology 41
2.5 Discussion 45
2.5.1 Comparison to Previous Stiffness Measurements 46
2.5.2 Comparison with Bullfrog Saccule Bundles 47
2.5.3 Comparison with Turtle Cochlear Bundles 50

Chapter 3: Stiffness Contribution of Interciliary Links 51
3.1 Introduction 51
3.2 Methods 54

3.2.1 Preparation and Solutions 54
3.2.2 Stiffness Measurements 55
3.2.3 Control Experiments 55
3.3 Results 56
3.3.1 Buffered HBSS Control 56
3.3.2 Calcium Free HBSS Control 56
3.3.3 Subtilisin 60
3.3.4 BAPTA 63
3.4 Discussion 66
3.4.1 Stiffness Reduction 66
3.4.2 Observations on Bleb Formation 66

Chapter 4: Mechanical Properties of the Kinocilium 68
4.1 Introduction 68
4.2 Theory 71
4.2.1 Flexural Rigidity 71
4.2.2 Fluid Drag Formulation 72
4.2.3 Rotational Stiffness 75
4.3 Methods 76
4.3.1 Supporting the Kinocilium for Flexural Rigidity Measurements 76
4.3.2 Separating the Kinocilium for Rotational Stiffness Measurements 76
4.3.3 Force Deflection Technique 78
4.3.4 High Speed Video Technique 81
4.4 Results 83
4.4.1 Verification of High Speed Video Technique 83
4.4.2 Properties of the Kinocilium 85
4.5 Discussion 86
4.5.1 Comparison with Motile Cilia 88
4.5.2 Comparison of the High Speed Video and Force Deflection Techniques 89
4.6 Conclusions 89

References 90

List of Figures

Figure 1-1 Diagram of the turtle utricle 1
Figure 1-2 Illustration of bundle polarities in the turtle utricle 2
Figure 1-3 The line of polarity reversal 4
Figure 1-4 Dimensions of the bundle and stereocilia array 5
Figure 1-5 Striola and Extrastriola Bundles 7
Figure 1-6 Photodiode displacement sensor 10
Figure 2-1 Light microscope image of a folded utricle 16
Figure 2-2 Force deflection technique for measuring bundle stiffness 18
Figure 2-3 Bead calibration of glass fibers 19
Figure 2-4 Bundle Dimensions 20
Figure 2-5 Forcing fiber to bundle stiffness ratio vs. percent difference 24
Figure 2-6 Timing of stiffness measurements following injection 25
Figure 2-7 Bundle stiffness measurements over time 26
Figure 2-8 Normalized stiffness vs. time from initial measurements 27
Figure 2-9 Temporal response of the base and tip of the fiber 30
Figure 2-10 Temporal response of the fiber base 31
Figure 2-11 Calibration factor vs. fiber oscillation frequency 32
Figure 2-12 Bundle stiffness vs. distance from the line of polarity reversal 34
Figure 2-13 Box plot of the striola and extrastriola bundle stiffness 35
Figure 2-14 Characteristic Bundle Morphologies 38
Figure 2-15 Bundle morphology varies with macular location 39
Figure 2-16 Bundle stiffness vs. dimensional parameters 42
Figure 2-17 Comparing dimensional parameters of stiff and weak bundles 43
Figure 3-1 Illustrations of the interciliary links in a hair bundle 52
Figure 3-2 Normalized stiffness measurements over time for control experiments 58
Figure 3-3 Pictures of tested bundles before and after control experiments 59
Figure 3-4 Normalized stiffness of four bundles exposed to subtilisin 60
Figure 3-5 Reduction in stiffness of four bundles during exposure to Subtilisin 61
Figure 3-6 Pictures of four bundles before and after subtilsin exposure 62
Figure 3-7 Normalized stiffness of four bundles exposed to BAPTA 63
Figure 3-8 Reduction in stiffness of four bundles during exposure to BAPTA 64
Figure 3-9 Pictures of bundles before and after BAPTA exposure 65
Figure 3-10 Bleb formation in calcium free solution 67
Figure 4-1 Structure of the 9+2 axoneme in cilia 69
Figure 4-2 Cantilever Beam 71
Figure 4-3 Triangularly distributed load on the kinocilium 74
Figure 4-4 Rigid bar pivoting about a rotational spring 75
Figure 4-5 A supported kinocilium for flexural rigidity measurements 77

Figure 4-6 Detached kinocilium for rotational stiffness measurements 78
Figure 4-7 Force deflection technique incorporating dual photodiodes 79
Figure 4-8 Effect of kinocilium loading condition 81
Figure 4-9 Kinocilium return to equilibrium 82
Figure 4-10 Measured flexural rigidity vs. kinocilium height 86

List of Tables

Table 2-1 Bead calibration of constant diameter glass fibers 22
Table 2-2 Summary of imitation bundle study 23
Table 2-3 Dimensional parameters for the stiff and weak bundle populations 44
Table 2-4 Morphology of bundles in the bullfrog saccule and turtle utricle 49
Table 4-1 Measured and calculated properties of constant diameter glass fibers 84
Table 4-2 Measured mechanical properties of the kinocilium 85

Chapter 1: Introduction

1.1 Turtle Utricle

The utriclular macula in turtle has a characteristic scallop shape (Jorgensen 1974). The illustration in Figure 1-1 gives a top view of the left utricle of a turtle, *Trachemys (Pseudemys) scripta*. The number of hair cells in the utricle of *T. scripta* varies with age from ~4000 in prehatchlings to ~12,000 in mature animals (Severensen et al., 2003). The distribution of these hair cells is highly organized with respect to bundle polarity, cell type, and bundle morphology (Jorgensen 1974, Jorgensen 1988, Severensin 2003, Moravec and Peterson 2004, Xue and Peterson 2006).

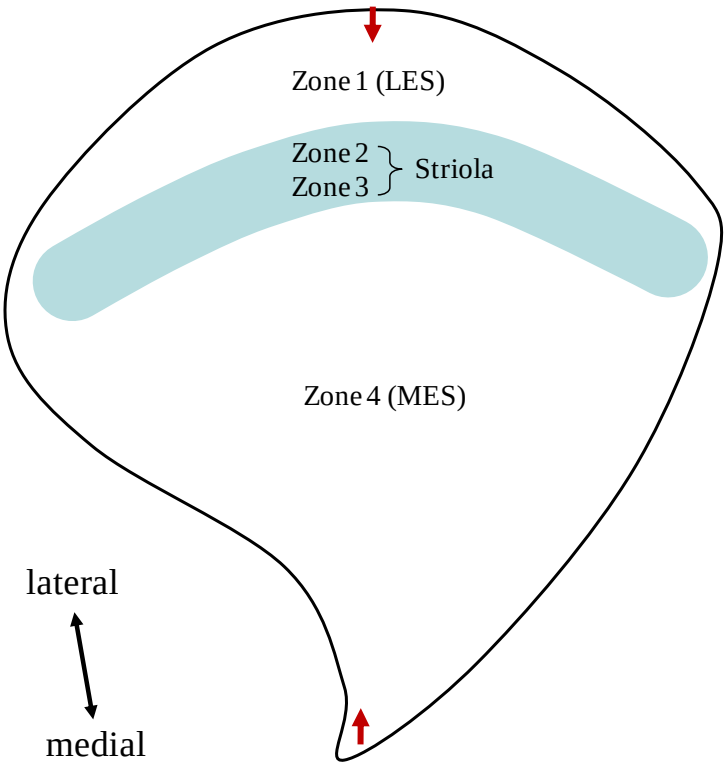

Figure 1-1. Diagram of the turtle utricle.
This illustration is of a left turtle utricle. The utricle can be divided into four regional zones. Zone 1 corresponds to the lateral extrastriola (LES). Zones 2 and 3 make up the striola. Zone 4 corresponds to the medial extrastriola (MES) which occupies the largest percentage of the surface area. The blue band represents the approximate location of the crescent shaped striola. The red arrows indicate a central medial to lateral transect.

1.2 Regional Organization of the Turtle Utricle

The striola in the turtle utricle is crescent shaped and runs parallel to the lateral edge of the macula (Fig. 1-2). It separates the medial extrastriola (MES) and the lateral extrastriola (LES) and accounts for approximately 8% of the total area (Severinsen et al., 2003). The MES and LES account for approximately 63 and 29% of the total area, respectively (Severinsen et al., 2003). The hair bundles are oriented so that their directions of maximal sensitivity, or polarity, fan outward from the medial tip of the utricle to the lateral edge (Fig. 1-2). A somewhat tortuous line of polarity reversal (LPR) exists near the lateral edge of the striola about which the bundle polarities flip (Fig. 1-3). Thus the MES and striolar bundles are oriented with their kinocilium closest to the lateral edge, and the LES bundles are in reverse.

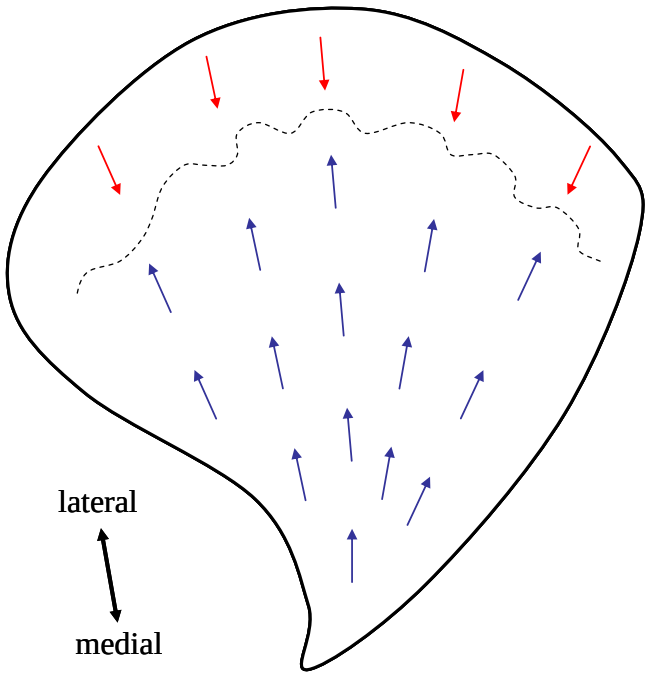

Figure 1-2. Illustration of bundle polarities in the turtle utricle.
Hair bundle polarities, or directions of maximal sensitivities, fan across the surface of the utricular macula. The wavy dashed line represents the line of polarity reversal. Blue and red arrows indicate the sensitivity directions of bundles medial and lateral to the LPR, respectively.

The turtle utricle also exhibits regional organization of type I and II hair cells. Type II hair cells are found in all regions of the utricle, while type I cells are restricted to a single band within the striola (Jorgensen 1988, Severensin 2003, Moravec and Peterson 2004, Xue and Peterson 2006). This single band is a common trait in reptiles versus the double band observed in birds and the widespread distribution in mammals (Jorgensen 1988). Fluorescent labeling of the calyces of type I cells in the turtle utricle demonstrated that the band follows the trajectory of the striola, is 50-60 μm wide and approximately 20-30 μm from the LPR (Moravec and Peterson 2004).

Recent work examining the organization of the turtle utricle designates four regional zones: zone 1 corresponds to the LES, zone 2 to the lateral striola, zone 3 to the medial striola, and zone 4 to the MES (Fontilla and Peterson 2000, Moravec and Peterson 2004, Rowe and Peterson 2006, Xue and Peterson 2006). The striola is divided into zones 2 and 3 where zone 3 corresponds to the band containing type I hair cells.

The neuroepithelium and overlying otoconial membranes also demonstrate regional variations. The neuroepithelium is thicker in the striola than the extrastriola region (Jorgensen 1974, Severinsen et al., 2003, Xue and Peterson 2006). The peak thickness of the striola in turtle has been measured as twice (190 μm) that of the medial and lateral margins of the extrastriola (Fontilla and Peterson 2000). The thickness of the otoconial membranes in the turtle also varies across the macular surface (Xue and Peterson, 2003). In the striola and LES, the otoconial layer is thinnest and has smaller crystals. Conversely, the gel layer is very thin over the MES and thickens over the striola and LES. The column filament layer overlying the neuroepithelium is thinnest over the striola, slightly thicker over the MES and markedly thicker over the LES. This pattern mimics the variation of kinocilium heights across the macular surface, allowing bundle tips to contact the gel layer in the striola. In the extrastriola, several microns of the kinocilium can embed in the OM. Overall, the spatial variation in the otoconial membranes likely alters the stimulus delivered to bundles in different macular locations (Xue and Peterson, 2003).

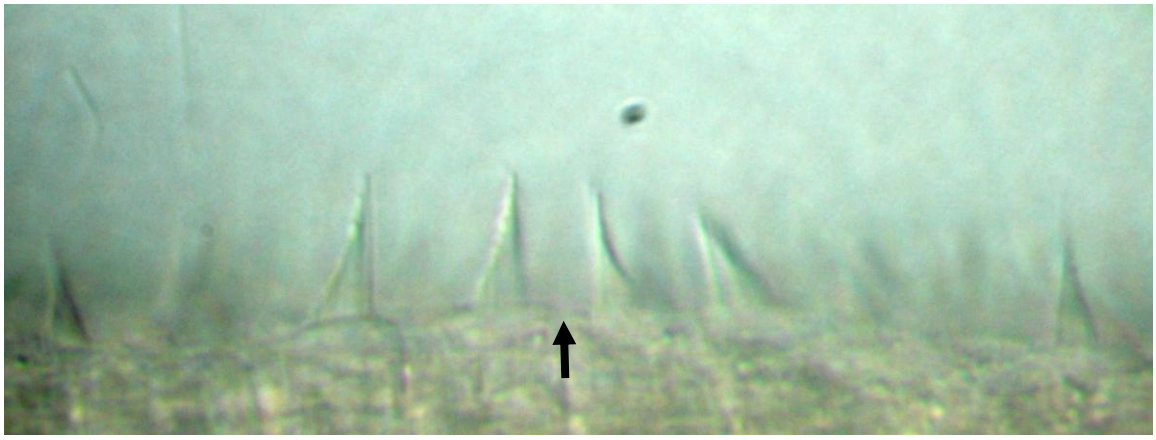

Figure 1-3. The line of polarity reversal.
A light microscopy image of the line of polarity reversal (arrow) in the turtle utricle. The LPR lies along the lateral edge of the striola and defines the line about which the excitatory directions of the hair bundles flip. The bundles to the right and left of the arrow are medial and lateral bundles, respectively.

1.3 Bundle Morphology

Hair cell bundle morphologies in the utricle demonstrate highly organized and distinct regional variations. Bundle morphology in conjunction with macular location and cell type has been quantitatively detailed for the turtle utricle with respect to bundle dimensions (Fontilla and Peterson 2000, Xue and Peterson 2006), number of stereocilia (Moravec and Peterson 2004), and pattern and orientation of the stereocilia array (Rowe and Peterson 2006).

In the following discussion, bundle morphology is described through several parameters shown in Fig. 1-4. Dimensional parameters are all measured in μm and include the kinocilium, tallest stereocilia and shortest stereocilia heights and the length and width of the array. Stereocilia array is a term collectively referring to the number, spacing, and distribution of the stereocilia. Array length is the span of the array in the direction parallel to the excitatory/inhibitory axis of the bundle, while array width is the span perpendicular to the axis. The KS ratio is defined as the height of the kinocilium divided by the height of the tallest stereocilia. Bundle slope refers to the difference between the tallest and shortest stereocilia divided by the array length.

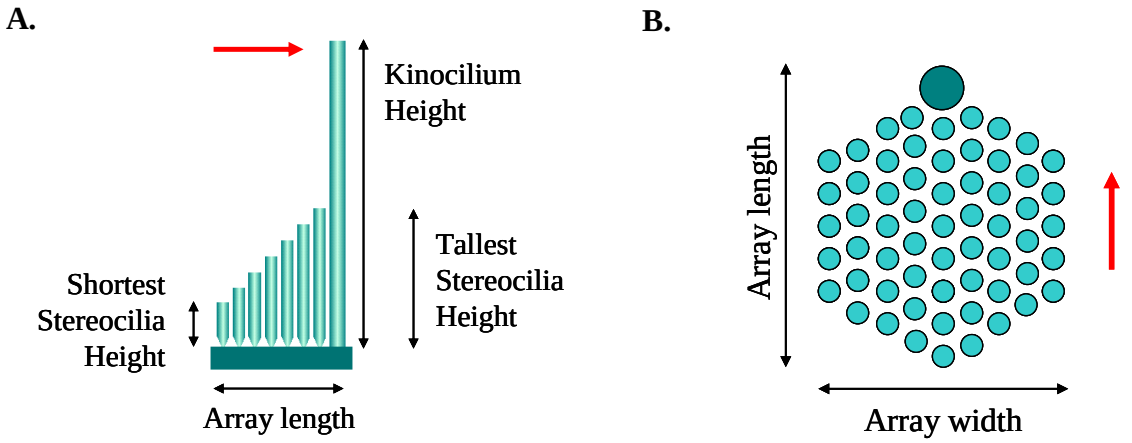

Figure 1-4. Dimensions of the bundle and stereocilia array.
A. A side view illustration of a hair bundle. The four dimensional parameters frequently discussed are labeled. **B.** An illustration of a stereocilia array from a top view. The large dark circle represents the kinocilium, and the smaller lighter circles represent the stereocilia. The two array dimensions are labeled. Red arrows are pointing in the excitatory directions.

1.3.1 Bundle Morphology in Striola Zones 2 and 3

Hair cell bundles in the striola have distinct morphological characteristic when compared to extrastriola bundles (Fig. 1-5). There are also distinctions between striolar bundles in zones 2 and 3 and between type I and type II cells. These distinctions extend to bundle heights and stereocilia arrays.

When compared to extrastriola bundles, striola bundles have much shorter and more homogenous kinocilium heights (Fontilla and Peterson, 2000, Xue and Peterson, 2006). More specifically, zone 2 bundles demonstrate the shortest kinocilia and the most homogenous bundle structures (Xue and Peterson, 2006). The heights of the tallest and shortest stereocilia are greater in zone 2 bundles than in other regions of the macula, and the KS ratios are approximately equal to 1. Zone 3 bundles have kinocilium heights similar to zone 2 bundles, but have significantly shorter array and stereocilia lengths, higher KS ratios, and less steep slopes (Xue and Peterson, 2006). Bundle structure in zone 3 is not as homogenous as in zone 2, in part due to differences between the bundles of type I and II cells. The morphology of type I bundles varies with macular location demonstrating a decrease in the height of the tallest stereocilia and an increase in KS ratio with distance from the line of polarity reversal (Xue and Peterson 2006). In addition,

type I cells have significantly taller stereocilia, longer array lengths, lower KS ratios, and steeper slopes compared to the neighboring type II bundles in zone 3.

Stereocilia number also varies with macular location such that striola bundles have significantly more stereocilia than those in the extrastriola (Moravec and Peterson 2004, Rowe and Peterson 2006). Type I cells have the highest number of stereocilia with an average of 96 ± 17. In addition, type II striola bundles have significantly more stereocilia (60 ± 9) than type II bundles in the adjacent extrastriola (45 ± 11) (Moravec and Peterson 2004). Given the greater stereocilia counts, it is not surprising that the array area is greater in the striola vs. extrastriola bundles. Array width is highly correlated with the array area, being significantly greater in the striola, while the array length demonstrates much less correlation (Rowe and Peterson 2006, Moravec and Peterson 2004). Within the striola, there is spatial variation in the stereocilia number and spacing. Stereocilia number increases and the spacing decrease with medial distance from the LPR (Rowe and Peterson, 2006). Increased spacing in zone 2 may be a result of greater stereocilia shaft diameters as indicated from confocal images (Rowe and Peterson, 2006). Stereocilia spacing in regions outside of zone 2 is relatively homogenous (Rowe and Peterson, 2006).

1.3.2 Bundle Morphology in Extrastriola Zones 1 and 4

As noted in the previous section, the most striking morphological difference between striola and extrastriola bundles is the height of the kinocilium. In a few bundles, the kinocilium heights can exceed 50 µm in zone 1 and 30 µm in zone 4. The median kinocilium heights in zone 1 and zone 4 are 14.5 and 13.4 µm, respectively (Xue and Peterson 2006). The KS ratios of extrastriola bundles are greater than the striola bundles (Xue and Peterson 2006).

Zone 1 hair bundles are especially heterogeneous in structure. The height of the kinocilium and tallest stereocilia are greatest and the array lengths are shortest within this region (Fontilla and Peterson 2000, Xue and Peterson 2006). Consequently, the steepest slopes of stereocilia falloff are observed in zone 1. The slopes are greatest just lateral to the LPR and decrease systematically towards the lateral utricular margin (Xue and Peterson, 2006). Zone 1 bundles are also unique in that they demonstrate the lowest average stereocilia counts (Moravec

and Peterson 2004). A very small population (3-4%) of the lateral bundles closest to the LPR exhibit a striola like structure and may in fact belong to zone 2 (Xue and Peterson 2006). These cells do not stain with calretinin; a trait of zone 2 but not zone 1 hair cells (Xue et al., 2005, Xue and Peterson 2006). Figure 1-5A shows a striola like bundle neighboring a bundle with the more prominent structure in the lateral extrastriola.

Bundles in zone 4 are similar to those in zone 1 in that they have large KS ratios, however they are distinguished by relatively shallow slopes. This trait is observed because the tallest stereocilia are shorter and the array lengths longer in zone 4 than in other regions of the utricle (Xue and Peterson 2006). Within a portion of zone 4 adjacent to the striola, the systematic change in bundle structure with macular location that occurs in the striola continues. Namely, the heights of the tallest stereocilia, the shortest stereocilia and the slope decrease, while the KS ratio increases with distance from the LPR. This systematic change ends about 150-200 µm medial to the LPR. Beyond this transitional region, in the mid to far extrastriola, the structure of the MES bundles are relatively uniform, Fig. 1-5C (Xue and Peterson 2006).

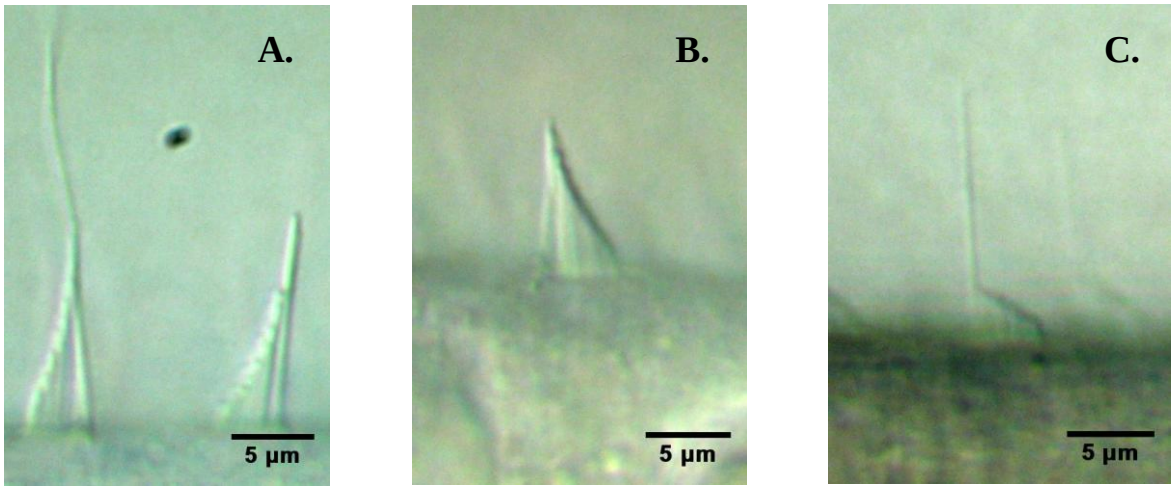

Figure 1-5. Striola and Extrastriola Bundles.
Photographs from differential interference contrast light microscopy showing the characteristic bundle morphologies in the lateral extrastriola (A), the striola (B) and the medial extrastriola (C). The bundle on the right of figure A has a striola like structure and may belong to the striola zone 2. The left bundle in figure A exemplifies the structure of the vast majority of lateral bundles.

1.4 Stiffness Measurements

The mechanical behavior of ciliary hair bundles can be quantified through stiffness measurements: a measure of the bundle's resistance to deflection in response to an applied force. The stiffness of both cochlear and vestibular hair bundles have been reported in literature for a variety of different species. Several different techniques have been employed to quantify bundle stiffness. Most of these techniques involve artificial deflection of the bundle through a flexible glass fiber, a fluid jet, or an atomic force microscope. In the most frequently employed method, the bundle is deflected with a flexible glass fiber of known stiffness. This technique has been applied to hair cell bundles of the guinea pig cochlea (Strelioff and Flock 1984), turtle cochlea (Crawford and Fettiplace, 1985), frog saccule (Ashmore 1984, Howard and Ashmore 1986, Howard and Hudspeth 1987, Howard and Hudspeth 1988, Jaramillo and Hudspeth 1993), and cultured mouse cochlea (Kossl et al., 1990). Others have employed a fluid jet to deflect the hair bundles of isolated chick cochlear cells (Szymko et al., 1992) as well as vestibular and cochlear cells of the neonatal mouse (Geleoc et al., 1997). Bundle stiffness has also been measured by applying force to the individual stereocilia of rat cochlear hair cells through the cantilever probe of an atomic force microscope (Langer et al., 1997). In another technique, the stiffness of unperturbed bundles was evaluated by measuring the bundle's Brownian motion through optical differential interferometery. Through this technique, the stiffness of hair bundles from the bullfrog saccule (Denk et al., 1989) and chick utricle (Bashtanov et al., 2004) have been measured.

1.4.1 Stiffness Measurements With a Flexible Fiber

Measurements of bundle stiffness using a flexible glass fiber are performed under a light microscope. The bundle is manipulated by an extremely fine glass fiber orthogonally attached to a rigid probe or shank. The stiffness of the fiber is independently determined. The fiber is positioned horizontally and its free end is placed against the hair bundle. The probe attached to the opposite end is displaced a known distance, usually with a piezoelectric actuator. The displacement of the whisker tip in contact with the bundle is measured with a photodiode sensor. The force applied to the bundle can be determined from the stiffness and flexion of the glass fiber. In turn, the applied force and bundle deflection are used to quantify the bundle stiffness.

1.4.2 Bundle Stiffness Calculation

The mechanical stiffness (k) of a ciliary bundle can be determined by applying a force (F) and measuring the resulting deflection (δ) (Eq. 1).

$$k = \frac{F}{\delta} \tag{1}$$

Typically, bundles were deflected in their excitatory direction by placing the tip of a flexible glass fiber in contact with the top of the bundle and displacing the base of the fiber. Measurements are taken of the fiber base displacement (δ_{base}) and the resulting bundle deflection (δ_{tip}) from which the deflection of the fiber (δ_F) can be determined (Eq. 2).

$$\delta_F = \delta_{base} - \delta_{tip} \tag{2}$$

Because the contact forces between the bundle and the fiber are equal and opposite, Eq. 3 is true,

$$k_B \delta_{tip} = k_F \delta_F \tag{3}$$

where k_B and k_F are the stiffness of the bundle and fiber, respectively. Substituting Eq.2 into Eq. 3 gives an equation for bundle stiffness (Eq. 4) where all terms on the right hand side of the equation can be measured experimentally.

$$k_B = k_F \left(\frac{\delta_{base}}{\delta_{tip}} - 1 \right) \tag{4}$$

1.4.3 Photodiode Sensor

The photodiode sensors used to measure displacement at the tip of the fiber consist of two rectangular photodiodes positioned side by side (Fig. 1-6). The magnified image of the bundle and fiber tip, is projected onto the photodiodes such that the fiber's tip is aligned with the gap separating the photodiodes. Typically, the image is magnified 700-1000X. Movement of the fiber alters the distribution of light on the photodiodes. As the magnified image of the fiber

passes between the two photodiodes, their differential voltage output is proportional to the position of the fiber. The photodiode sensors are capable of measuring bundle displacements on a nanometer scale. With the exception of an early work by Strelioff and Flock, 1984, measurements of bundle stiffness employing a flexible glass fiber have incorporated a photodiode sensor.

The photodiode sensor is calibrated in at least one of two ways. In one technique, the shank of a freely moving fiber is displaced a known distance and the corresponding voltage change from the diodes is recorded. The probe movement for calibration has consisted of step displacements (Crawford and Fettiplace, 1985) and triangular waveforms of 0.5 – 5 Hz (Howard and Ashmore, 1996). In a second technique, a piezoelectric bimorph displaces the photodiodes as the fiber remains stationary. Some investigators have employed both techniques (Howard and Hudspeth, 1987, Howard and Hudspeth 1988, Kossl et al., 1990, Russel et al., 1992).

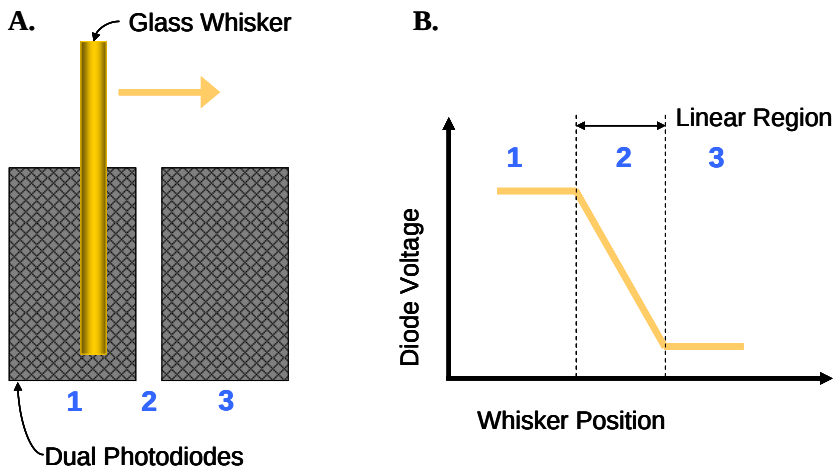

Figure 1-6. Photodiode displacement sensor.
A) Diagram representing a magnified glass fiber moving across a dual array of photodiodes. The numbers 1, 2, and 3 represent the diode on the left, the gap separating the diodes, and the diode on the right, respectively. **B)** An idealized plot of the photodiode output voltage vs. the position of the glass fiber. A linear region exists where the fiber moves between the two diodes (2). The experiments are performed within the linear region.

1.4.4 Flexible Fibers

The flexible fibers used for manipulating hair bundles are fabricated by drawing glass rods into fibers with varying dimensions and stiffnesses depending on the requirements of the specific investigation. Fibers with diameters ranging from 200 nm to 4 μm and lengths varying from 100 μm to 2 mm have been used. The stiffness of the fibers reported in literature range from 60 – 3,300 μN/m. In some cases, the fibers were sputter coated with approximately 100-300 nm of gold to improve their optical contrast (Howard and Hudspeth 1987, Howard and Hudspeth 1988). Clean fibers, frequently acid cleaned, are reported to adhere to the membranes of hair bundle and to the kinocilia bulb of frog saccular bundles (Howard and Ashmore 1986, Howard and Hudspeth 1987, Howard and Hudspeth 1988, Jarmillo and Hudspeth 1993).

The stiffness values of the glass fibers are traditionally determined through one of three methods. In one of the most frequently employed methods, acrylic spheres of known density are hung on the end of a horizontally positioned fiber (Howard and Ashmore 1986, Howard and Hudspeth 1987, Howard and Hudspeth 1988, Kossl et al., 1990, Russel et al., 1992, Jaramillo and Hudspeth 1993, Ricci et al., 2000). From the size and density of the spheres and the length and vertical displacement of the fiber, the fiber stiffness can be determined. In a second method, the stiffness of the whisker is determined solely from the mechanical properties of the glass, the Young's modulus, and the fiber dimensions using an equation for a cantilevered beam (Strelioff and Flock 1984, Crawford and Fettiplace 1985). The third technique frequently employed measures the Brownian motion of the fiber tip from which the stiffness and damping coefficient can be inferred (Howard and Hudspeth 1987, Howard and Hudspeth 1988, Marquis and Hudspeth 1997, Jaramillo and Hudspeth 1993). Many authors have chosen to use two of the techniques described above to verify their fiber stiffness results.

To accurately measure bundle stiffness, the relative stiffness between the fiber and the bundle should fall within an acceptable range. The calculation of bundle stiffness relies on a detectable difference between the base and tip displacements of the fiber. The fiber must be weak enough to flex slightly when manipulating the bundle. If the fiber were too weak relative to the bundle, the displacement at the distal tip of the fiber would approach zero. In addition, slight rotational movements of the distal tip due to severe flexion of the fiber might be detected

by the photodiode sensor. It would be impossible to distinguish such movements from translational displacements at the tip.

Few authors specifically mention the relative stiffness between the stimulating fiber and the bundle. Howard and Ashmore (1986) specify that their measurements were more accurate when the ratio of fiber to bundle stiffness was between 0.2 and 2 (bundle measurements were 0.5 – 5X the stiffness of the whisker). Howard and Hudspeth (1987) reported that the ratios of fiber to bundle stiffness were between 0.1 and 0.5. Other authors do not specify a range of fiber to bundle stiffness ratios, but approximate values can be inferred from the minimum and maximum fiber and bundle stiffness values that were reported. With a few exceptions, the fiber to bundle stiffness ratios were between 0.07 and 6.

The requirements of individual investigations dictate the dimensions of the fibers. Viscous drag increases with increasing length and diameter of the fiber. Studies examining the instantaneous and adaptive responses of bundles require minimal viscous drag to enable faster temporal responses. To fabricate fibers of appropriate stiffness with faster temporal response, the diameters were considerable reduced and the lengths shortened. Fibers used to measure only the steady state bundle stiffness ranged in diameters from 0.5 – 4 μm and had lengths between 0.1 – 2 mm (Strelioff and Flock 1984, Crawford and Fettiplace 1985, Howard and Ashmore 1986, Kossl et al., 1990). For measurements of the instantaneous stiffness, the fibers were reduced to diameters as small as 200-300 nm and lengths of 100 - 200 μm (Howard and Hudspeth 1987, Howard and Hudspeth 1988, Jarmillo and Hudspeth 1993). Both types of bundle stiffness measurements, steady state and instantaneous, were performed with fibers in a similar range of stiffness.

1.4.5 Variations on the Flexible Fiber Technique

Jaramillo and Hudspeth (1993) developed a displacement-clamp technique to measure the forces generated in the bundle in response to a displacement stimulus. As in the traditional force deflection technique, the bundle was deflected with a flexible fiber and a photodiode sensor monitored the position of the fiber's tip in contact with the bundle. Through negative feedback, a piezoelectric stimulator adjusted the base position of the fiber to maintain a steady bundle

displacement. The force required to maintain a constant bundle position was measured from the fiber's flexion and stiffness. It reflected the magnitude and timing of forces generated in the hair bundle by the gating springs and adaptive motors. The first displacement-clamp experiment indicated that the gating springs account for at least a third of the dynamic bundle stiffness and that the tension in each gating spring of a resting bundle is approximately 8 pN (Jaramillo and Hudspeth, 1993).

The displacement-clamp technique has been very useful in examining the active properties of the hair bundle. Benser et al. in 1996, improved the temporal resolution of the displacement clamp system which enabled recording of the forces associated with the fast twitch. Rapid positive bundle deflections elicit a mechanical twitch transpiring in a few milliseconds. The twitch is biphasic: consisting of an initial movement in the positive direction and a secondary movement in the negative direction. The displacement clamp measurements demonstrated that the bundle exerts a biphasic force corresponding to the mechanical twitch and working against the external load of the fiber.

In another variation of the flexible fiber technique, the motion of the hair bundle rather that the fiber tip was detected by the photodiode sensor (Ricci et al., 2000, 2002). Care was taken to align the long axis of the tallest stereocilia with the optical axis of the microscope. This allowed the hair bundles to behave as "light pipes" whose movement was detectable by the photodiode sensor at very high magnifications. A vertically oriented flexible fiber positioned at the height of the shortest stereocilia was used to stimulate the hair bundles. The microscope was then focused on the tips of the stereocilia, above the focal plane of the flexible fiber, and that image was projected onto the photodiodes. As with the flexible fiber, displacement of the bundle was proportional to the differential output of the photodiodes. The location of force application was lower than the measurements of the bundle tip deflection. As a result, the translational stiffness, as it would have been measured with the fiber positioned at the top of the bundle, was approximated by assuming the bundles pivot about their insertions (Crawford and Fettiplace 1985).

Chapter 2: Hair Bundle Stiffness Variation with Structure and Location

2.1 Introduction

Measurements of hair cell bundle stiffness from this study are distinct from previous works in several ways. First, the stiffness of hair bundles in the turtle utricle has not been previously reported. Secondly, stiffness was examined in conjunction with bundle morphology. Stiffness measurements were made on bundles with a variety of different structures including bundles in which the kinocilium projects far above the tallest stereocilia. The stiffness of these types of bundles, KS ratios greater than 1, have not been previously reported. Thirdly, stiffness was examined in conjunction with the bundle's macular location and comparisons between the striola and extrastriola regions were made.

2.2 Methods

2.2.1 Preparation

Experiments were performed on isolated utricular macula of turtles, *Trachemys (Pseudemys) scripta elegans*. Carapace lengths ranged from 3.75 to 5.75 in. Animals were euthanized via 0.5 ml injections of Euthosal (390 mg pentobarbital sodium and 50 mg phenytoin sodium per ml) in compliance with guidelines of the Virginia Tech Animal Care and Use Committee. Utricles were extracted and maintained at room temperature in oxygenated Hanks' Balanced Salt Solution buffered with 10 mM HEPES (HBSS: without phenol red, 1.26 mM $CaCl_2$, 0.493 mM $MgCl_2$, 0.407 $MgSO_4$, 5.33 mM KCl, 0.441 mM KH_2PO_4, 4.17 mM $NaHCO_3$, 137.93 mM NaCl, 0.338 mM Na_2HPO_4, 5.56 mM D-Glucose). The solution had a pH of 7.2 and an osmolarity of 300 mOsm. With the otoconial membrane (OM) still intact, utricles were folded along a medial to lateral transect and securely pinned in an experimental chamber. Folding with the OM removed produced bundle damage. An eyelash was used to gently peel the OM away without enzymatic digestion. We chose not to use enzymatic digestion to avoid potential damage to the structural components of the bundles such as the intercilliary links. This preparation enabled a side view of bundles in all four zones along the folded edge of the epithelium (Fig. 2-1). The side view accommodated measurements of bundle heights and distances from the LPR. Only bundles that appeared healthy and intact, with no visible signs of damage, were tested. The bundles were viewed with differential interference contrast (DIC) using a Zeiss Axioskop with 10X eyepieces, 100X liquid immersion objective (1.0 NA), and an oil immersion condenser (1.4 NA). The microscope was located on a vibration isolation table.

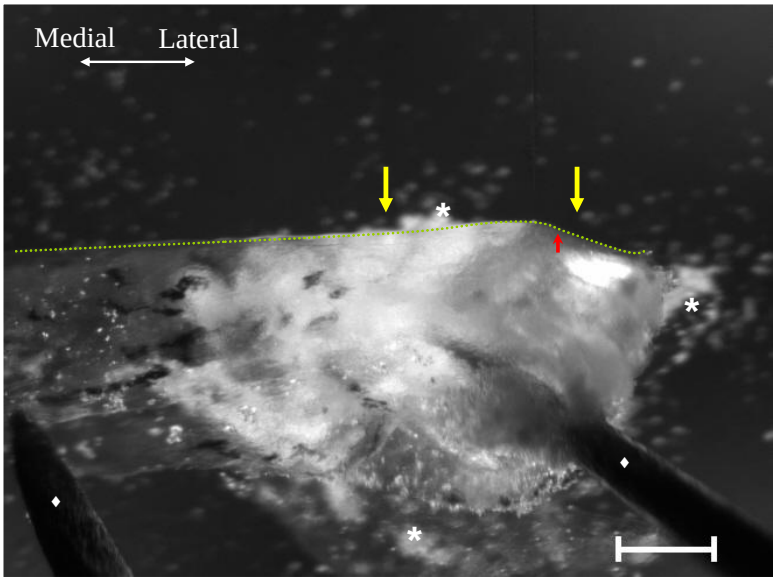

Figure 2-1. Light microscope image of a folded utricle.
The utricle was folded along a medial to lateral transect and secured with metal pins (♦). The otoconial membrane was peeled away, but a few otoconia crystals remain on the microscope slide. These appear as white clumps of crystals (*) and scattered white flecks. The green dotted line indicates the folded edge. Stiffness measurements were taken along a 400 μm portion of the transect, between the yellow arrows, spanning the striola and parts of the medial and lateral extrastriola. The approximate location of the LPR is marked with the red arrow. The scale bar represents 200 μm.

2.2.2 Stiffness Measurements

Bundle stiffness was measured using a well established force-deflection technique in which the bundle is deflected by a flexible glass fiber of known stiffness (Crawford and Fettiplace, 1985). From the fiber's stiffness (k_f), base (δ_{base}) and tip (δ_{tip}) deflections, the bundle's stiffness was determined from Eq. 1. This equation is derived from the force balance relationship between the tip of the glass fiber and the bundle.

$$k_b = k_f \left(\frac{\delta_{base}}{\delta_{tip}} - 1 \right) \quad (1)$$

Displacements of the fiber tip were measured using a pair of photodiodes housed on the camera port of the microscope. The rectangular photodiodes are positioned side by side and the gap separating them was aligned with the projected image of the fiber (magnified 100X). As the magnified image of the fiber passed between the two photodiodes, their differential output voltage is proportional to the position of the fiber.

The base of the fiber was sinusoidally oscillated using a piezoelectric linear actuator (Burleigh, PZS-050) with a peak-to-peak amplitude of 1 μm and a frequency of 0.5 Hz. Displacements of the fiber's base were measured using a fiber optic displacement sensor (EFPI: extrinsic Fabry-Perot interferometer, Luna Innovations, Blacksburg, VA) with a resolution of 1 nm that was secured to the linear actuator. The horizontally oriented fiber was brought into contact with bundles projecting from the folded edge of the macula such that the long axis of the fiber was parallel with that of the kinocilium (Fig. 2-2). This orientation ensured that the fiber contacted only one bundle, even in densely populated regions. The tip of the fiber was positioned as close to the top of the kinocilium as possible while still maintaining contact, typically 1 - 2 μm from the top. Bundles were pushed in their excitatory direction from their resting position with each oscillation.

The oscillating fiber was in contact with the bundle for 30 sec. trials. Immediately following each trial, the fiber was retracted to a position just above the bundle in the same horizontal plane. The fiber was oscillated free from contact, at the same amplitude and frequency, for 30 sec. to calibrate the photodiodes. Signals from both the photodiodes and the EFPI were recorded in LabVIEW 7.0 (National Instruments) and sampled at 1 kHz. The data was filtered in MATLAB 7.0.4 (The MathWorks, Inc.) with a 4^{th} order lowpass digital Butterworth filter. Also in MATLAB, the peak-to-peak displacements of the fiber's base and tip were extracted from the recorded data. Bundle stiffness was calculated from the deflection of each oscillation and averaged to determine the bundle stiffness from that trial. At least three trials were performed and averaged for each hair bundle tested.

The employed procedure yields a steady-state or passive measurement of bundle stiffness. The time course of the bundle deflections, 1 sec, is much greater than that required for measuring the active response of the bundle, i.e. the instantaneous stiffness

measured within 0.75 – 1.25 ms after deflection. It should also be noted, that no bundle relaxation was observed within or between the 30 sec. trials.

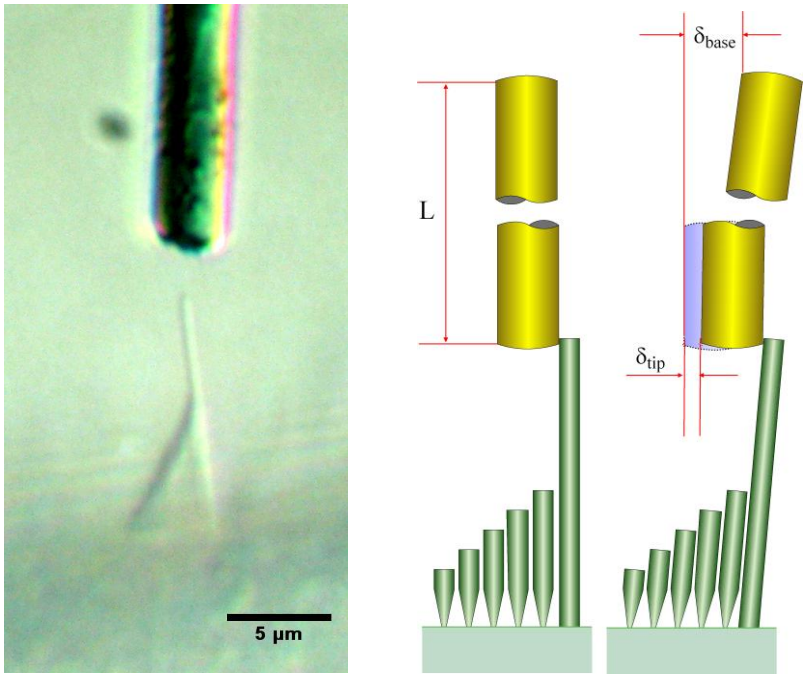

Figure 2-2. Force deflection technique for measuring bundle stiffness.
A horizontally oriented flexible glass fiber (gold rod) was brought into contact with the tip of the kinocilium. The whisker length (L) is much greater than the height of the bundle. Displacements of the whisker base (δ_{base}) and kinocilium tip (δ_{tip}) are measured.

2.2.3 Glass Fibers

Flexible glass fibers were made from borosilicate glass rods pulled to tip diameters ranging from 2.3 – 5.9 µm and trimmed to lengths of 1.34 – 4.12 mm. Their stiffness ranged from 19 – 433 µN/m. The fibers were sputter coated with 100 – 200 Å of gold to improve their optical contrast. Preliminary studies showed that sputter coated fibers produced a 3 fold increase in the distance of the photodiodes linear operating region.

The glass fibers were calibrated by statically attaching polymethyl methacrylate microbeads (30 – 100 µm) to the horizontally positioned fiber (Fig. 2-3). While viewed

with a micro forge at 35X, measurements were made of the fiber's vertical deflection (δ), fiber length (l), bead diameters, and the distance of the beads from the fiber tip (a_i). The fiber stiffness (k_F) was determined with an equation for a cantilevered beam, Eq. 2, with multiple point loads (Merkle, 2000). The weight of the bead (W_i) was determined from the bead volume and density (1190 kg/m^3). The number of beads attached to the whisker (n) typically ranged from 1 to 4.

$$k_F = \frac{\sum_{i=1}^{n} W_i \left(1 - \frac{3a_i}{2l} + \frac{a_i^3}{2l^3}\right)}{\delta} \tag{2}$$

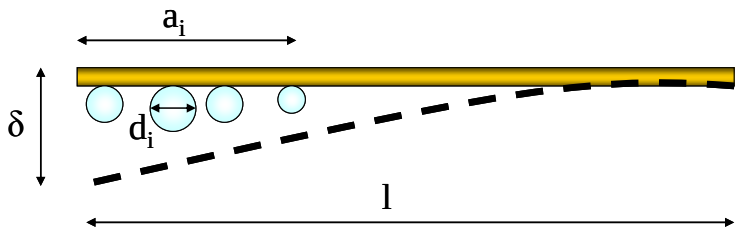

Figure 2-3. Bead calibration of glass fibers. Four parameters were measured during the bead calibrations of fiber stiffness: the fiber length (l), vertical deflection (δ), bead diameters (d_i) and the position of the beads from the fiber tip (a_i).

2.2.4 Dimensional Measurements of Bundles

High resolution digital pictures were taken of each bundle tested. Using ImageJ software (NIH, public domain), bundle dimensions and the location relative to the line of polarity reversal were measured. Measured dimensions include the heights of the kinocilium, tallest and shortest stereocilia, and array length (Fig. 2-4). The KS ratio (height of the kinocilium divided by the height of the tallest stereocilia) and slope (difference in the height of the tallest and shortest stereocilia divided by array length)

were calculated for each bundle. Distance from the LPR was measured as the distance from the kinocilium of the tested bundle to the kinocilium of the medial bundle at the LPR in the same focal plane. A fifth bundle dimension, the array width, could not be accurately measured since the folded preparation positions the bundles on their side. Array width describes the depth of the stereocilia array when viewed from the side and is perpendicular to the excitatory direction.

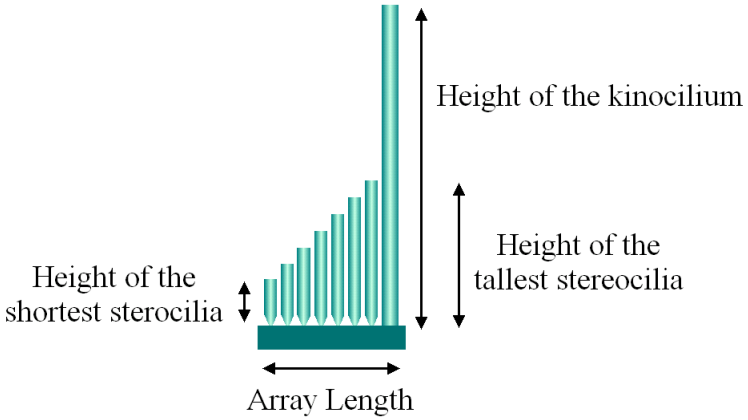

Figure 2-4. Bundle Dimensions.
Four bundle dimensions were measured to characterize the bundle morphology. From these dimensions, the KS ratio and slope were calculated.

2.3 Verification of Measurements

2.3.1 Accuracy of the Glass Fiber Calibrations

The stiffness of a cantilever beam of constant diameter can be determined through Eq. 3 when the Young's modulus (E), length (L), and diameter (d) are known. To assess the accuracy of the bead calibration in determining the stiffness of glass fibers, it was desirous to compare the bead calibration results with values obtained through Eq. 3. The fibers fabricated in the lab for testing typically vary in diameter along their length, so it was necessary to obtain fibers of uniform diameter for the comparison.

$$k_F = \frac{3\pi d^4 E}{64 L^3} \tag{3}$$

Constant diameter glass fibers of ≤ 10 μm are not readily available. The techniques for pulling glass fibers used in our laboratory were insufficient for producing glass fibers of constant diameter. Commercially available glass fibers could not be found in the correct size range. The best source we found for appropriate fibers proved to be fiberglass insulation. The insulation was dissolved in acetone, and straight glass fibers of uniform diameter (≈ 10 μm with maximum variations of 0.34 μm) were extracted. These fibers were then glued orthogonally to a thin glass rod, and the fiber stiffness was determined through both the bead calibration technique and Eq. 3. General purpose glass fibers, like those used in insulation, have a Young's modulus of 76-78 GPa (Wallenberger et al., 2001). A modulus of 77 GPa was used to calculate fiber stiffness. The fiber diameters were measured in ≈1 mm increments along the fiber's length, and the average was used in the stiffness calculation. The diameter variations and stiffness results from 3 fibers are presented in Table 2-1. For fibers 1 and 3, the bead calibrations differed from the formula values by < 11%. The second fiber had a higher percent difference of 18%, and it also had the largest variation in diameter along its length. One explanation for the high percent difference is that the variation in the fiber diameter may have resulted in an overestimation of the stiffness determined through Eq. 3 as the actual

fiber stiffness would be reduced by the thinner regions. On a whole, the analysis of constant diameter fibers demonstrated that the bead calibrations are an accurate measure of fiber stiffness.

			stiffness (μN/m)		
Fiber	diameter (μm)	length (mm)	calculated	bead calibrated	% difference
1	10.71 ± 0.27(8)	6.37 ± 0.05 (3)	577	530 ± 149 (4)	8
2	9.22 ± 0.34(8)	5.91 ± 0.10 (3)	397	327 ± 13 (4)	18
3	10.13 ± 0.24 (5)	4.50 ± 0.01 (3)	1310	1170 ± 162 (4)	11

Table 2-1. Bead calibration of constant diameter glass fibers.
The dimensional properties of constant diameter fibers were used to calculate fiber stiffness through Eq. 3 (Young's modulus = 77 GPa). The percent differences of the bead calibrations from the calculated stiffness values are given.

2.3.2 Imitation Bundles

To verify the accuracy of our measurement system, the stiffness of imitation bundles were measured. Glass fibers that were fabricated and calibrated through the same process previously described served as the imitation bundles. They were positioned opposite the forcing fiber, and their stiffness was measured through the same technique used to determine bundle stiffness. The accuracy of the measurement system was assessed as the percent difference between the photodiode system and the bead calibration measurements of the imitation bundle stiffness.

A total of 7 glass fibers were incorporated in this process with stiffness values of 7.6, 17, 44, 50, 168, 327, and 1170 μN/m. From these fibers, 17 different forcing fiber and imitation bundle combinations were tested (Table 2-2). Results showed that accuracy depends on the relative stiffness between the forcing fiber and the imitation bundle (Fig. 2-5). When the ratio of forcing fiber to imitation bundle stiffness was greater than 0.17 the percent difference in the photodiode system and the bead calibrated stiffness was ≈10% or less. When the ratio of forcing fiber to bundle stiffness was less than 0.17, the accuracy greatly reduced to percent differences between 30 and 90%.

These results suggest that fibers lose the capability of deflecting bundles that are approximately 6 times or more than their own stiffness. The relatively weak fibers simply do not produce sufficient bundle movement to be detected by the photodiode system.

As a precaution, all bundle stiffness measurements reported were made with a ratio of fiber to bundle stiffness greater than or equal to 1 (ie. the stiffness of the glass fiber was the same or greater than the bundle).

Bead calibrated stiffness (μN/m)		Force-deflection stiffness (μN/m)		
Forcing fiber (k_F)	Imitation bundle (k_{IB})	Imitation bundle	% difference	k_F / k_{IB}
7.6 ± 1.0 (3)	44 ± 5 (5)	42 ± 9 (5)	4.5	0.17
	327 ± 13 (4)	74 ± 24 (6)	77.4	0.02
	1170 ± 162 (4)	126 ± 77 (5)	89.2	0.01
17 ± 2 (4)	7.6 ± 1.0 (3)	8.0 ± 1.1 (6)	-5.3	2.24
	44 ± 5 (5)	42 ± 10 (5)	4.5	0.39
	327 ± 13 (4)	165 ± 47 (4)	49.5	0.05
	1170 ± 162 (4)	266 ± 96 (6)	77.3	0.01
50 ± 6 (5)	7.6 ± 1.0 (3)	7.6 ± 0.6 (6)	0.0	6.58
	44 ± 5 (5)	44 ± 4 (6)	0.0	1.14
	327 ± 13 (4)	220 ± 39 (6)	32.7	0.15
	1170 ± 162 (4)	782 ± 61 (7)	33.2	0.04
168 ± 40 (6)	7.6 ± 1.0 (3)	7.2 ± 0.7 (8)	5.3	22.11
	44 ± 5 (5)	44 ± 5 (8)	0.0	3.82
	327 ± 13 (4)	292 ± 25 (6)	10.7	0.51
	1170 ± 162 (4)	752 ± 245 (6)	35.7	0.14
327 ± 13 (4)	1170 ± 162 (4)	1092 ± 57 (5)	6.7	0.28
1170 ± 162 (4)	327 ± 13 (4)	294 ± 64 (7)	10.1	3.58

Table 2-2. Summary of imitation bundle study.
Stiffness measurements of the forcing fibers and imitation bundles, avg. ± std. dev. (n), are given. Imitation bundle stiffness was determined through both bead calibrations and the force deflection technique employing the photodiode measurement system. The percent difference in the results of the force deflection method from the bead calibration technique is presented. The ratio of the forcing fiber to imitation bundle stiffness (k_F/k_{IB}) is also presented.

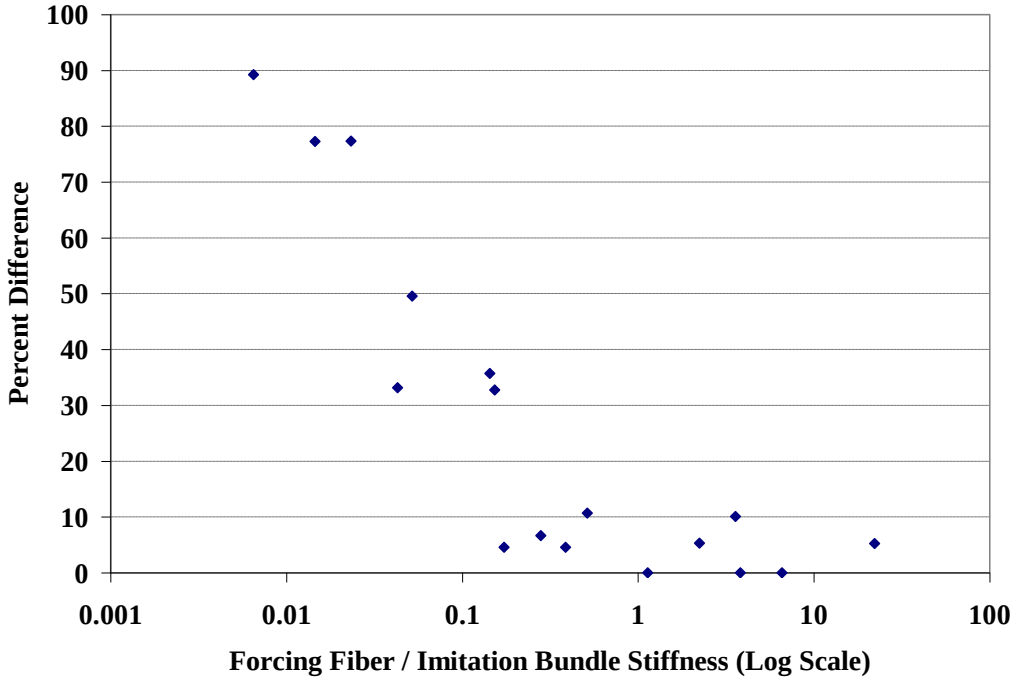

Figure 2-5. Forcing fiber to bundle stiffness ratio vs. percent difference. The ratio of forcing fiber to imitation bundle stiffness plotted against the percent difference between the photodiode and bead calibrated measurements of the imitation bundle stiffness. Absolute value of the percent difference is plotted.

2.3.3 Stiffness Measurements Over Time

The experiments for measuring bundle stiffness extended for long periods of time. Figure 2-6 shows the quantity of measurements taken within a given hour after the turtles were injected with Euthosal. The majority of measurements, 73%, were taken within 4 to 8 hours of injection. A few measurements were taken up to 9.5 hours following injection. In general, 3 to 4 hours were required between injection and the first bundle measurements for utricle extraction, folding and removal of the otoconial membrane.

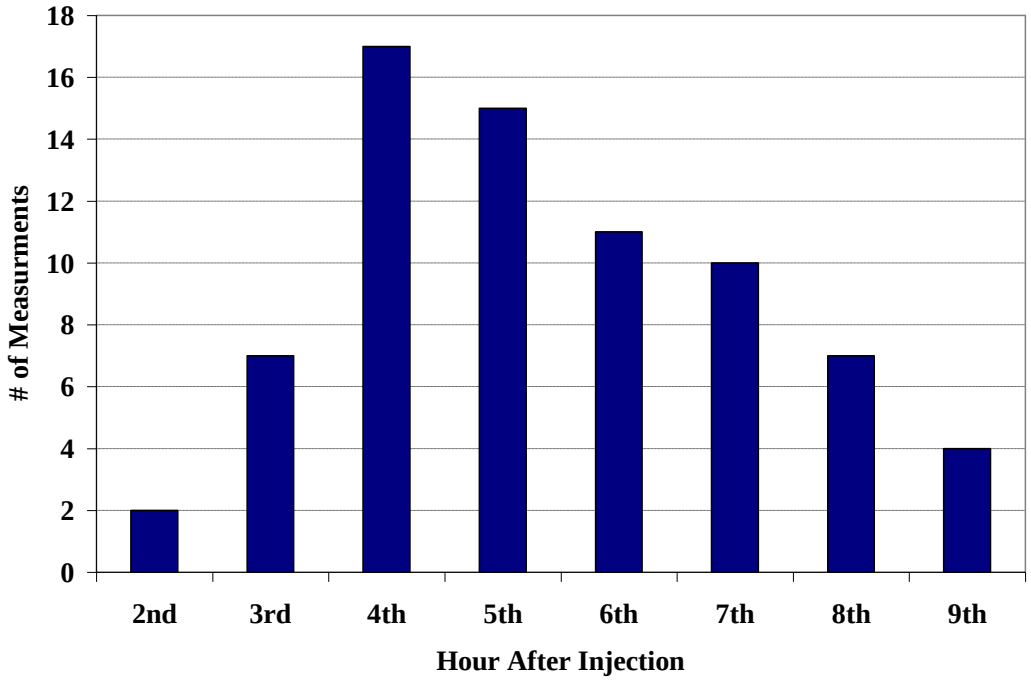

Figure 2-6. Timing of stiffness measurements following injection.
The plot shows the distribution of bundle stiffness measurements taken in a given hour following the euthanizing injection.

It was necessary to determine whether the preparations deteriorated causing the bundle stiffness to decline over the course of the experiments. To examine this, two striola bundles were measured repeatedly up to 9 hours following the injection. Stiffness measurements on the first bundle began 3.5 hours after the euthanasing injection, and 9 measurements were taken over the course of 5 hours. For the second bundle, measurements began 4.25 hours after injection and were repeated 8 times over the course of 5 hours. Figure 2-7 shows the measured stiffness values of both bundles plotted against the time from the initial measurement. Each measurement reported is the average of 4-5 trials.

For both bundles, stiffness did not decline in measurements taken up to 9 hours after the injection. The small fluctuations observed in stiffness measurements over time reflect the imprecision of the measurements system; a downward trend over time is not observed.

These results also show quantitatively the expected error of the bundle stiffness measurements. The average stiffness of the first bundle was 82 ± 17 (n=9) μN/m. The percent difference of the individual measurements from this average ranged from 0.7 – 19.5 %. The average stiffness of the second bundle was 103 ± 15 (n=8) μN/m, and the percent difference of the individual measurements were between 0.9 – 21.7 % from the average.

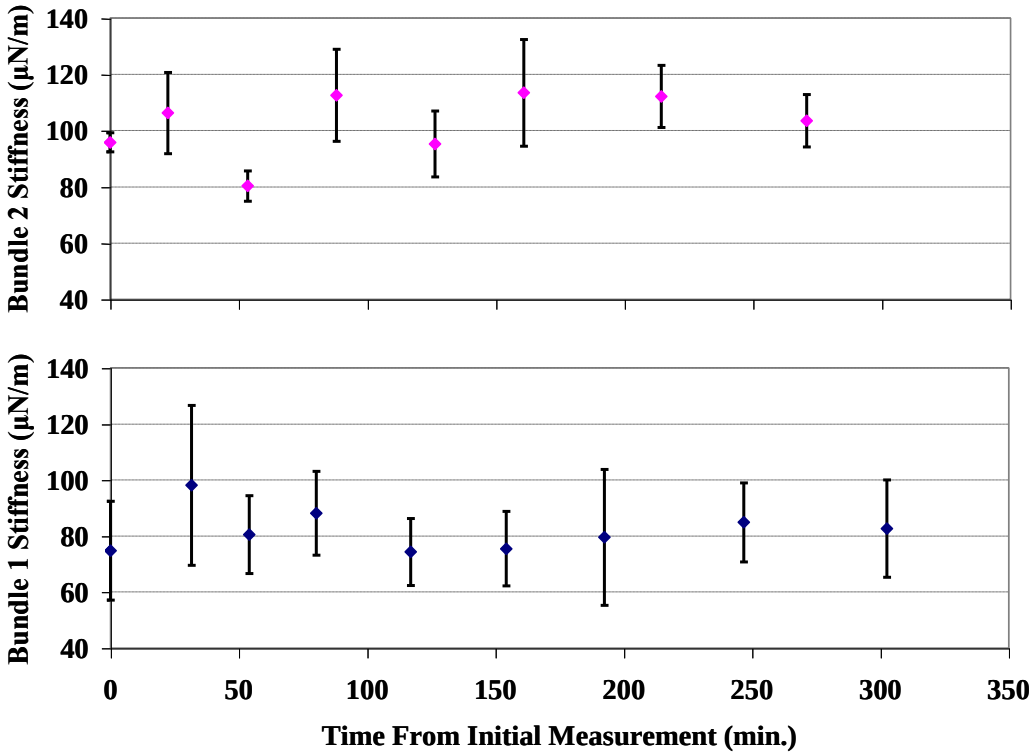

Figure 2-7. Bundle stiffness measurements over time.
Stiffness versus the time measurements were taken relative to the initial measurement for bundles 1 (blue) and 2 (pink). Each point plotted is an average of 4-5 measurement trials. Error bars represent the standard deviations.

Figure 2-8 plots the stiffness measurements over time of both bundles normalized to their average values. The majority of the measurements repeated over time were less than or equal to ±10% of the average value, represented by the blue shaded region of the plot. Once per bundle, the percent difference of a measurement reached 20% the average value. This indicates that the bundle stiffness measurements have a maximum expected error of 20%. The results of the imitation bundle study demonstrated that for forcing fiber to imitation bundle stiffness ratios greater than 0.17 the error was approximately 10%. The repeated measurements over time demonstrate that measurements on real bundles have a slightly higher expected error.

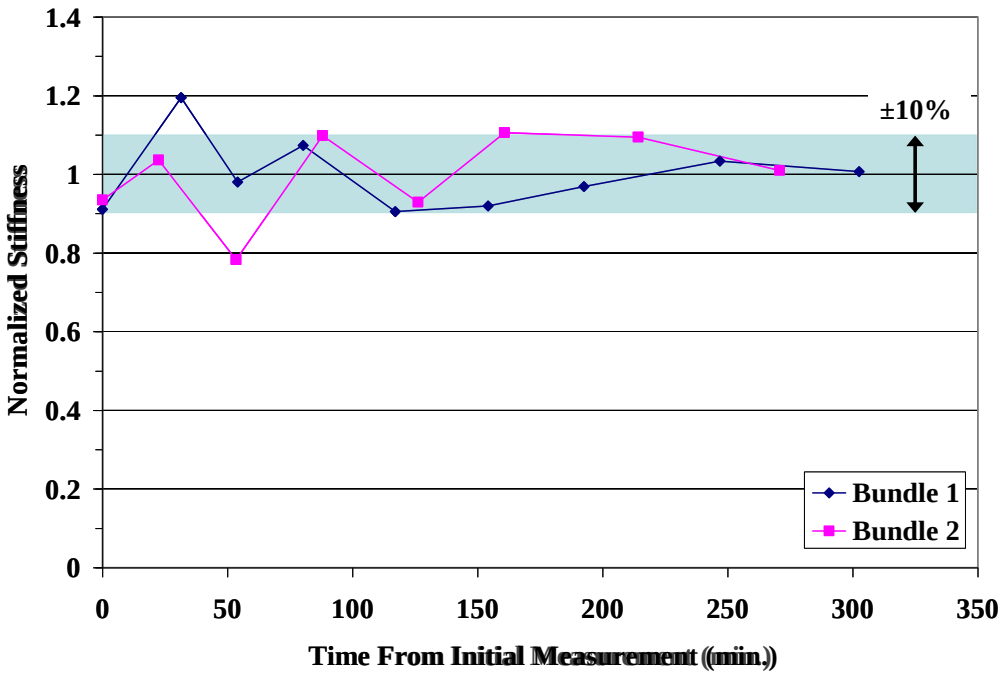

Figure 2-8. Normalized stiffness vs. time from initial measurements.
The individual stiffness measurements of bundles 1 and 2 were normalized to their average values. The shaded blue area represents ±10% of the average stiffness (normalized to 1). Only 1 measurement from each bundle varies more than 10% from the average value.

2.3.4 The Impact of Fluid Drag on the Calibration Factor

To calibrate the photodiode device, the glass fiber oscillates free from bundle contact and an image of the fiber tip is projected onto the diodes. The calibration process assumes that the fiber does not bend, and that the displacement at the fiber tip is equivalent to the applied base displacement. The calibration factor (CF) relates the unattached fiber tip displacements, measured as voltage change of the photodiodes (ΔV), to the displacement applied at the fiber base (ΔX), $CF = \Delta V / \Delta X$. If drag on the fiber reduced the tip displacement, the CF would be erroneously small (Eq. 4). This would lead to underestimations of tip deflection during bundle measurements leading to an underestimation of bundle stiffness.

$$\frac{\downarrow \Delta V}{\Delta X} = \downarrow CF \tag{4}$$

Equations 5 and 6 demonstrate how an underestimation of the CF would lead to a low calculation of bundle stiffness (k_B). Bundle stiffness is determined from the fiber's stiffness (k_F), tip displacement while contacting the bundle (δ_{tip}) and base displacement (δ_{base}). The δ_{tip} is determined from the change in diode voltage when the fiber is contacting the bundle ($\Delta V_{contact}$) and is dependent on the calibration factor (Eq. 5). Drag on the fiber when it is in contact with the bundle is assumed negligible because resistance from the fluid is much smaller than the resistance of the bundle (ie. $\Delta V_{contact}$ is not reduced by fluid drag).

$$\frac{\Delta V_{contact}}{\downarrow CF} = \uparrow \delta_{tip} \tag{5}$$

$$k_B = k_F \left(\downarrow \frac{\delta_{base}}{\delta_{tip}} - 1 \right) \tag{6}$$

Displacements of the whisker tip produce a change in the voltage output of the photodiodes that is converted to a distance through the calibration factor. Thus, the displacement of the fiber tip can not be determined independent of the calibration factor. As a result, it is difficult to directly measure whether the displacement of the fiber tip is reduced by drag. Two tests were performed to determine if fluid drag inhibits the movement of an oscillating fiber. 1) The temporal response of the fiber tip was compared to that of the fiber base during oscillations. A time delay between the fiber tip and base would demonstrate that the fluid drag was inhibiting the movement of the tip. 2) The peak to peak amplitude of the fiber tip displacements was examined over a range of frequencies. A drag affect would manifest as a decrease in tip deflection with increasing frequency.

2.3.4.1 Temporal Response of the Fiber Tip

To determine the impact of drag on the fiber tip deflection, the temporal response of both the base and tip of an oscillating fiber were examined. The base of the fiber is driven by a piezoelectric linear actuator, and its displacement is measured with the EFPI fiber optic sensor secured to the actuator. The output of the EFPI, piezoelectric driver and photodiodes were recorded while the fiber (K_F = 7.6 μN/m) oscillated a distance of 1 μm at 0.5 Hz in distilled water. In separate trials, the photodiodes were used to record the displacement of the fiber tip (Fig. 2-9) and, after repositioning the fiber, the displacements of the fiber base (Fig. 2-10). The fiber selected for these tests is weaker, by a factor of at least 2.5, than the fibers used to measure bundle stiffness. This was done to exaggerate any negative fluid drag affects.

The time points corresponding to the minimums and maximums of the sinusoidal outputs were compared to determine relative delay in the fiber movements measured by the three devices. There was a slight difference in the temporal response of the two devices measuring base displacement. Compared to the driver output, the EFPI min and max points were delayed by 105 ± 3 ms (150 oscillations). The EFPI is physically attached to the piezoelectric driver and so this delay was not expected. The delay in the

EFPI output may be related to frictional resistance in the EFPI fiber optic sensor or to computational time within the EFPI device. The results also showed that the fiber tip, measured with the photodiodes, was delayed from the fiber base. For the fiber tip, the min and max points were delayed from the driver by 304 ± 4 ms (105 oscillations). When the photodiodes were used to measure the response of the fiber base, there was a delay of only 34 ± 1 ms (45 oscillations). This demonstrated that the delay at the fiber tip is not inherent to the photodiode device. These results suggest that the tip of the fiber is slightly delayed as a result of viscous drag through the fluid. The next step is to determine if fluid drag also reduces the magnitude of the tip displacement.

Since the base of the whisker is not impacted by fluid drag, it may seem reasonable to calibrate the photodiodes using the fiber base. That would eliminate concerns about whether drag inhibited the movement of the tip and altered the calibration factor. However, the diameter at the base and tip of the fiber are not always consistent and resultantly would have different calibration factors.

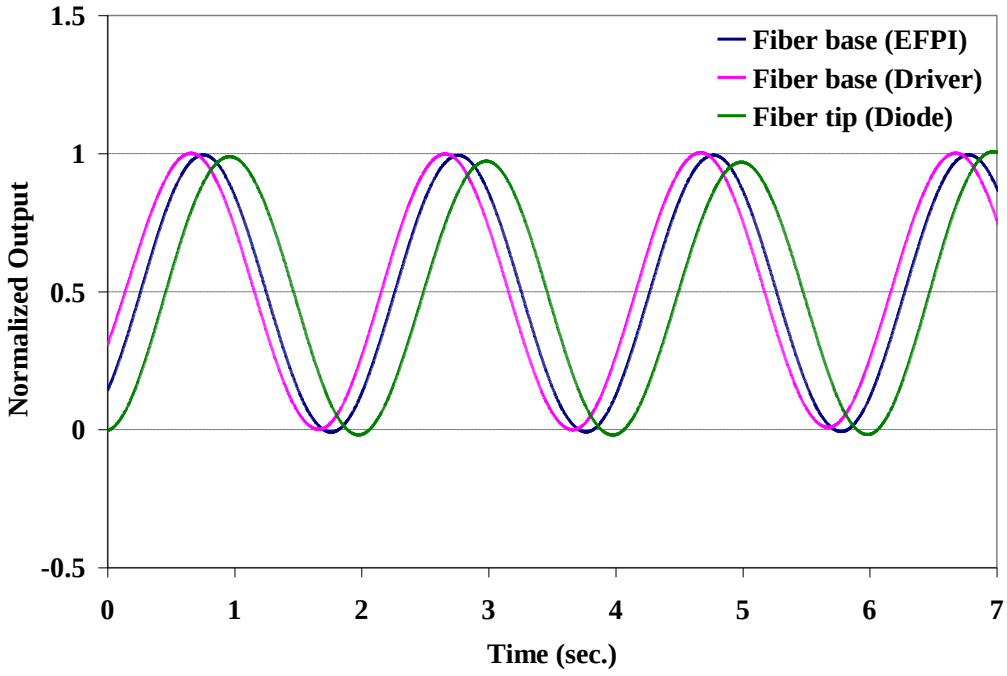

Figure 2-9. Temporal response of the base and tip of the fiber.
Temporal response of the fiber's base and tip shows that the tip lags the base during oscillations at 0.5 Hz. The fiber base movement is monitored by the output of the EFPI and linear actuator driver. The fiber tip movement is recorded with the photodiodes. The output of all three devices has been normalized.

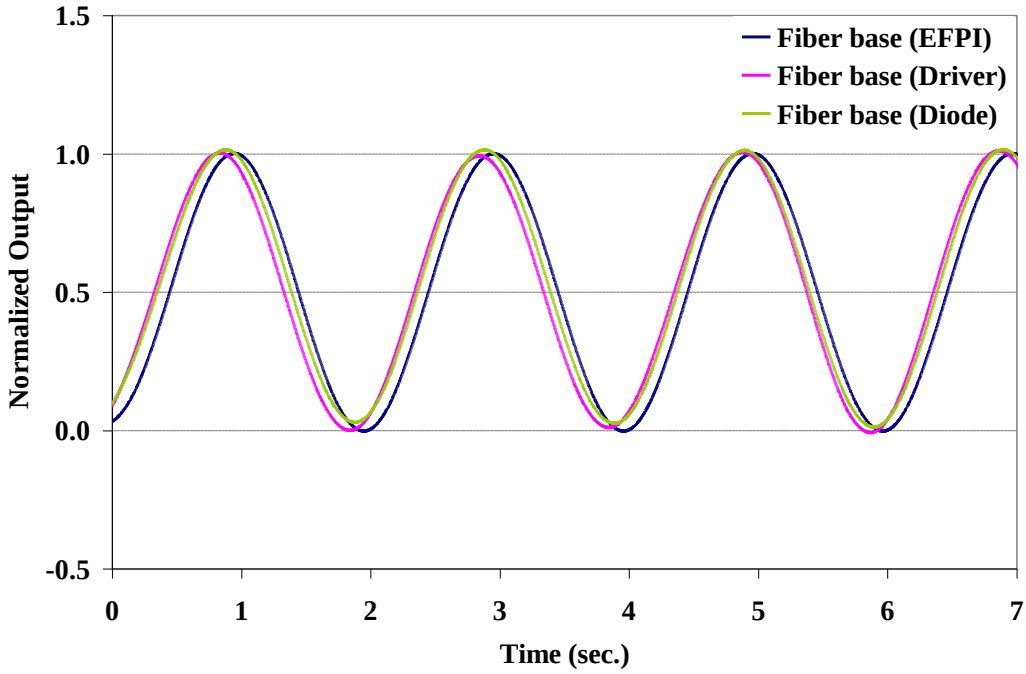

Figure 2-10. Temporal response of the fiber base.
Temporal response of the fiber base was monitored with three different devices: the EFPI, piezoelectric driver, and photodiodes. The fiber was repositioned so that its base was projected onto the photodiodes. The output of all three devices has been normalized.

2.3.4.2 Calibration Factor at Different Frequencies

The movement of the fiber tip was recorded with the fiber oscillating at different frequencies. The calibration factors at different frequencies were examined because they indicate whether the tip displacement decreased relative to the input base displacement with increasing frequency. The results also indicate a range of frequencies for which the drag effect was negligible.

Two series of test were run in which the peak to peak change in the EFPI and photodiode outputs were examined over different frequencies. In the first series, the fiber was oscillated at frequencies of 0.05, 0.1, 0.5, 1, and 5 Hz. The second series examined frequencies between 0.1 and 1 Hz in increments of 0.1 Hz. The results demonstrate that the calibration factor decreased with an increase in frequency (Fig. 2-11). This indicates

that the movement at the fiber tip is progressively less than the base movement as the frequency increases.

The standard deviation of calibrations at the lowest two frequencies, 0.05 and 0.1 Hz, were very large. This suggests that the fiber should not be oscillated below 0.2 Hz for stiffness measurements. At frequencies between 0.2 and 0.5 Hz, the calibration factor fluctuated between a range of 0.52 and 0.56 mV/µm. At frequencies above 0.5 Hz, the calibration factor consistently decreased with increasing frequency.

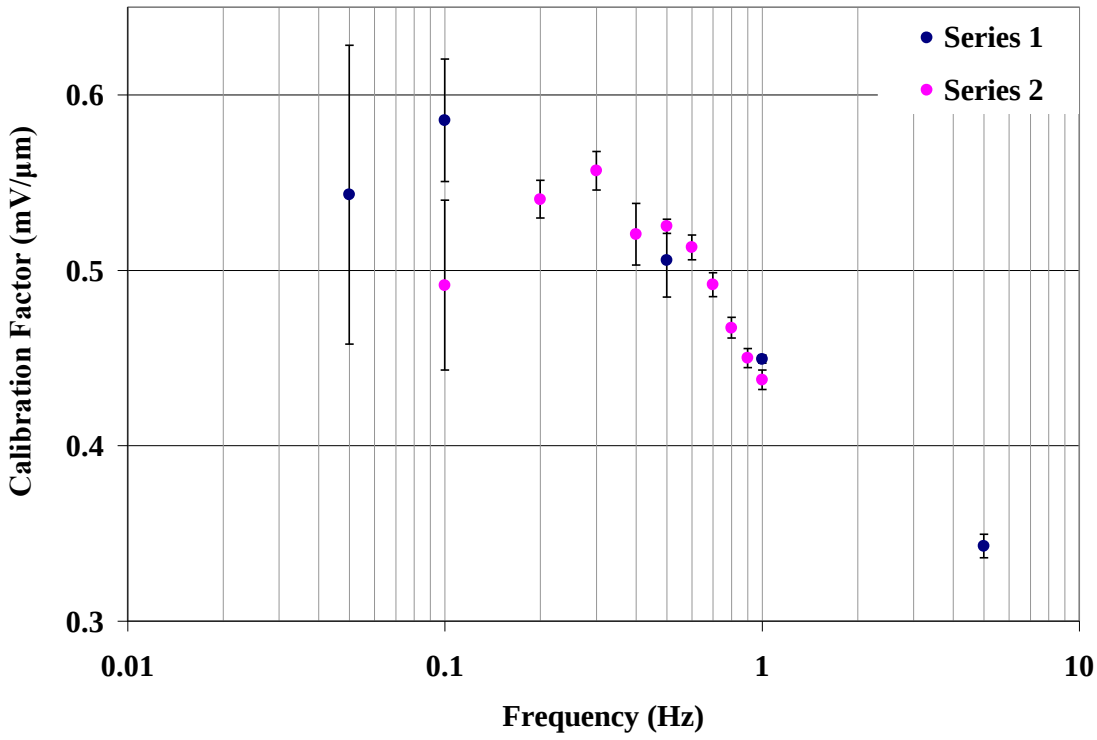

Figure 2-11. Calibration factor vs. fiber oscillation frequency.
A plot of calibration factor vs. frequency determined from both sets of tests. The standard deviations are very high at 0.5 and 0.1 Hz. Error bars indicate the standard deviations of at least three trials at each frequency.

Ten successive calibration trials were performed at 0.5 Hz to estimate the precision of the calibration technique. The factors determined from these trials ranged in value from 0.54 to 0.57 mV/µm. This 0.03 mV/µm range in CF at the same frequency is very close to 0.04 mV/µm range measured between 0.2 and 0.5 Hz. These results

suggest that within the precision of the calibration technique, a change in frequency between 0.2 and 0.5 Hz does not greatly impact the calibration factor. Furthermore, it indicates that fluid drag on the oscillating glass fiber is not inhibiting motion at our testing frequency of 0.5 Hz.

The impact of the observed variation in calibration factors on the calculation of stiffness was investigated using data from bundle measurements. The calibration factor from a stiffness measurements of a striola (70.13 μN/m) bundle were altered by ± 0.04 mV/μm. This resulted in a ±7.4 μN/m or 10% change in the stiffness

These frequency tests were performed with a weak fiber (K_F = 7.6 μN/m). Fibers used for bundle stiffness measurements ranged from 19 – 433 μN/m. The analysis was performed on a weak fiber to exaggerate the fluid drag affect. As the impact of drag on this weak fiber did not impair the calibration process, one can assume that the impact on stiffer fibers would be even less.

2.4 Results

2.4.1 Stiffness vs. Distance From the LPR

Stiffness measurements were taken of 73 bundles positioned along a central medial to lateral transect of 21 utricles. Measurements were taken along a ≈400 μm portion of the transect including the striola and portions of the medial and lateral extrastriola. Figure 2-12 shows that within the examined region, bundle stiffness varies greatly with bundle location. The stiffest bundles are found within 50μm medial and several microns lateral to the LPR. Lateral to the LPR, bundle stiffness decreases drastically within a short distance. On the medial side of the LPR, bundle stiffness is markedly heterogeneous and declines systematically with distance from the LPR to the medial extrastriola.

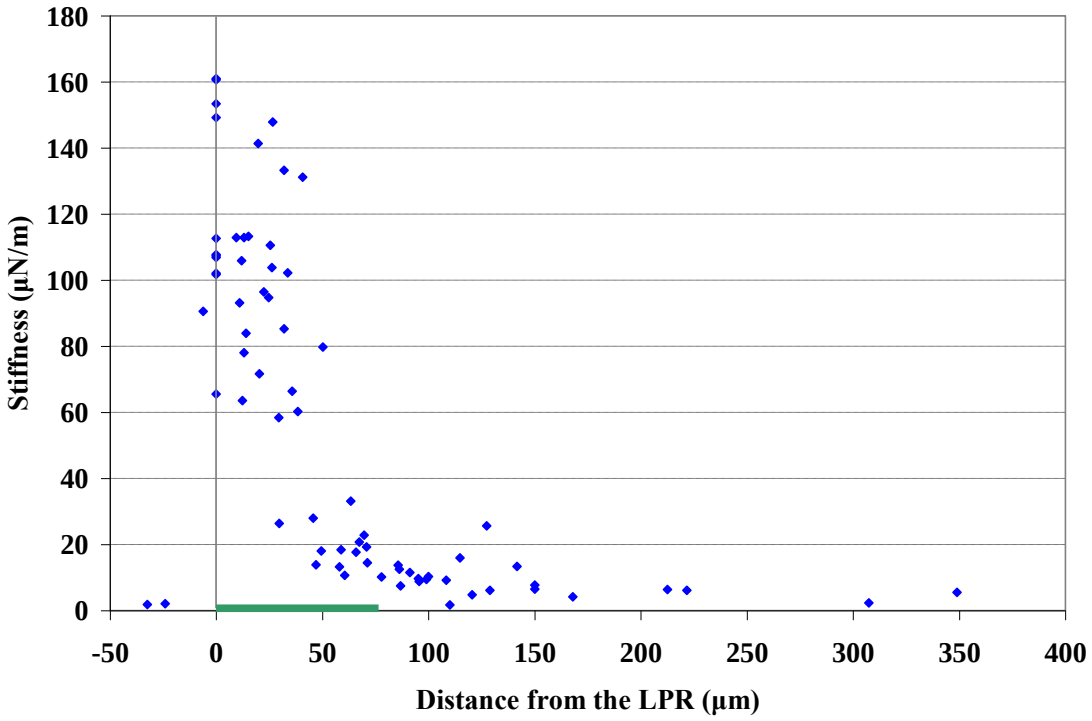

Figure 2-12. Bundle stiffness vs. distance from the line of polarity reversal.
The measured bundle stiffness systematically decreased with the bundle location from the LPR. The vertical grey line represents the LPR and the green bar along the x-axis represents the approximate width of the striola (75 μm).

For statistical analysis, bundles were separated into striola and extrastriola groups. Medial bundles less than 75µm from the LPR and a single lateral bundle (k=91 µN/m) were classified as striola bundles. Light microscopy does not enable clear visualization of the nerve endings to detect the striola edge. However, fluorescent labeling of nerve calyces using confocal microscopy has shown that the striola in the turtle utricle is approximately 75 µm wide and may contain a few lateral bundles that demonstrate striola like morphologies (Xue and Peterson, 2006). The box plot in Fig. 2-13 shows the means, standard deviations, and quantiles of stiffness in the striola and extrastriola bundles. In the striola, there was a 150 µN/m range (11-161 µN/m) in bundle stiffness. Stiffness of the extrastriola bundles had a smaller range of 23 µN/m (2 – 25 µN/m). The mean bundle stiffness in the striola (82 ± 46, n=48) and extrastriola (9 ± 5, n=25) regions were significantly different ($p<0.001$, Wilcoxen Ranked Sum). The variation of stiffness within each region is much greater than the expected error of the measurements and is attributable to differences in bundle structure.

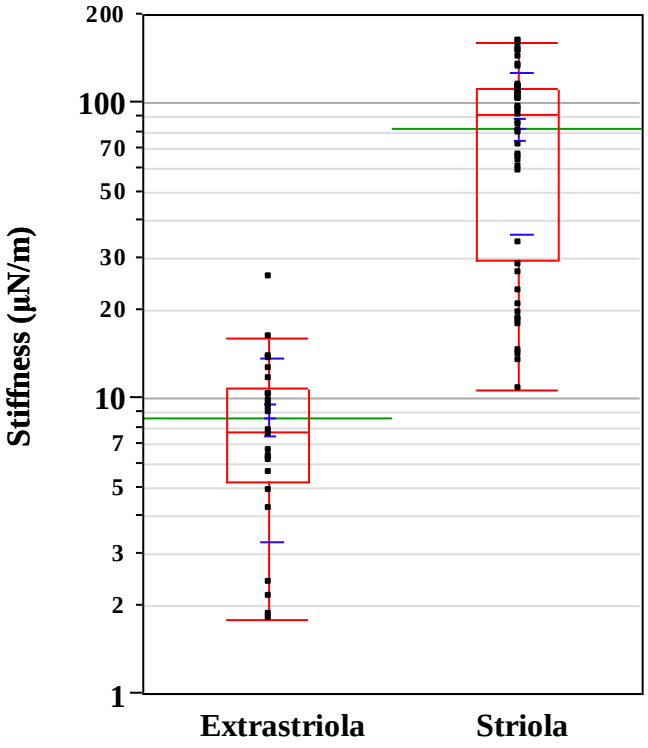

Figure 2-13. Box plot of the striola and extrastriola bundle stiffness. The stiffness axis is plotted on a log scale. The green bars represent the means and blue bars the standard deviations. The top and bottom edges of the red boxes represent the 75th and 25th quantiles. The red mid line of the box is the median. Extended red lines, or whisker, represent 1.5 times the interquartile range (75th – 25th quantiles).

2.4.2 Bundle Morphology vs. Distance From the LPR

Bundle morphology was characterized through 4 measured and 2 calculated dimensional parameters: kinocilium height, tallest and shortest stereocilia heights, array length, KS ratio, and slope. Each parameter demonstrated systematic variation with distance from the LPR (Fig. 2-15). The variations were consistent with published data measured from confocal microscope images (Xue and Peterson, 2006). The array lengths Fig. 2-15 E are slightly greater than the published data, however their definitions differ slightly. In the current work, the array length is defined as the distance from the shortest stereocilia to the kinocilia. In published data, it is the distance from the shortest stereocilia to the tallest stereocilia (Xue and Peterson, 2006).

Figure 2-15 A-C shows the heights of kinocilium, tallest stereocilia, and KS ratio plotted against the distance from the LPR. In the striola, kinocilium heights were shortest, the tallest stereocilia heights were greatest, and the KS ratios were close to 1. These three dimensional parameters were relatively homogenous within the first 25 μm medial to the LPR. This is in agreement with data from the confocal study demonstrating homogeneity of bundle structure in zone 2, the 15-25 μm wide band on the medial side of the LPR. Within the region 25 to ≈100 μm medial to the LPR, the heights of the kinocilium and tallest stereocillia systematically increased and decreased, respectively, corresponded to an increase in the KS ratio with increasing distance from the LPR. In this transitional region, bundle morphology progressively changes from characteristicly striola to medial extrastriola structures. In the extrastriola region 100 μm medial to the LPR, the kinocilium projected far above the tallest stereocilia giving KS ratios around 3 - 5. The variation in kinocilium and tallest stereocilia heights was very small in the far medial extrastriola. Only three lateral extrastriola bundles were examined. One, positioned -6 μm from the LPR, resembled the striola bundle morphology with a 8.9 μm tall kinocilium and KS of 1.1. Bundles with this morphology are far less prevalent in the lateral extrastriola and are always in close proximity to the LPR. The other two lateral bundles, positioned -20 – -30 μm from the LPR, were representative of the majority of lateral bundles. Their kinocilium were very tall (42.9 and 44.1 μm), and their tallest stereocilia were moderately tall (5.4 and 6.0 μm).

Figure 2-15 D-F shows the height of the shortest stereocilia, the array length, and the slope plotted against distance from the LPR. Within the striola, heights of the shortest stereocilia spanned a wide range (0.6 – 3.3 μm). In the extrastriola, heights of the shortest stereocilia were less varied and considerably shorter (all but two < 1.5 μm). Array lengths appeared to decrease with distance from the LPR within the striola, and slightly increase with progression into the medial extrastriola. Bundle slopes were greatest in the striola. Over a short distance (~75 μm) immediately adjacent to the striola, slopes decreased with distance from the LPR. In the medial extrastriola beyond 150 μm from the LPR, the variation in slope was small.

The characteristic morphologies of bundles from the striola, medial and lateral extrastriola are demonstrated by the light microscope images in Fig. 2-14. The bundles are viewed from the side with DIC optics.

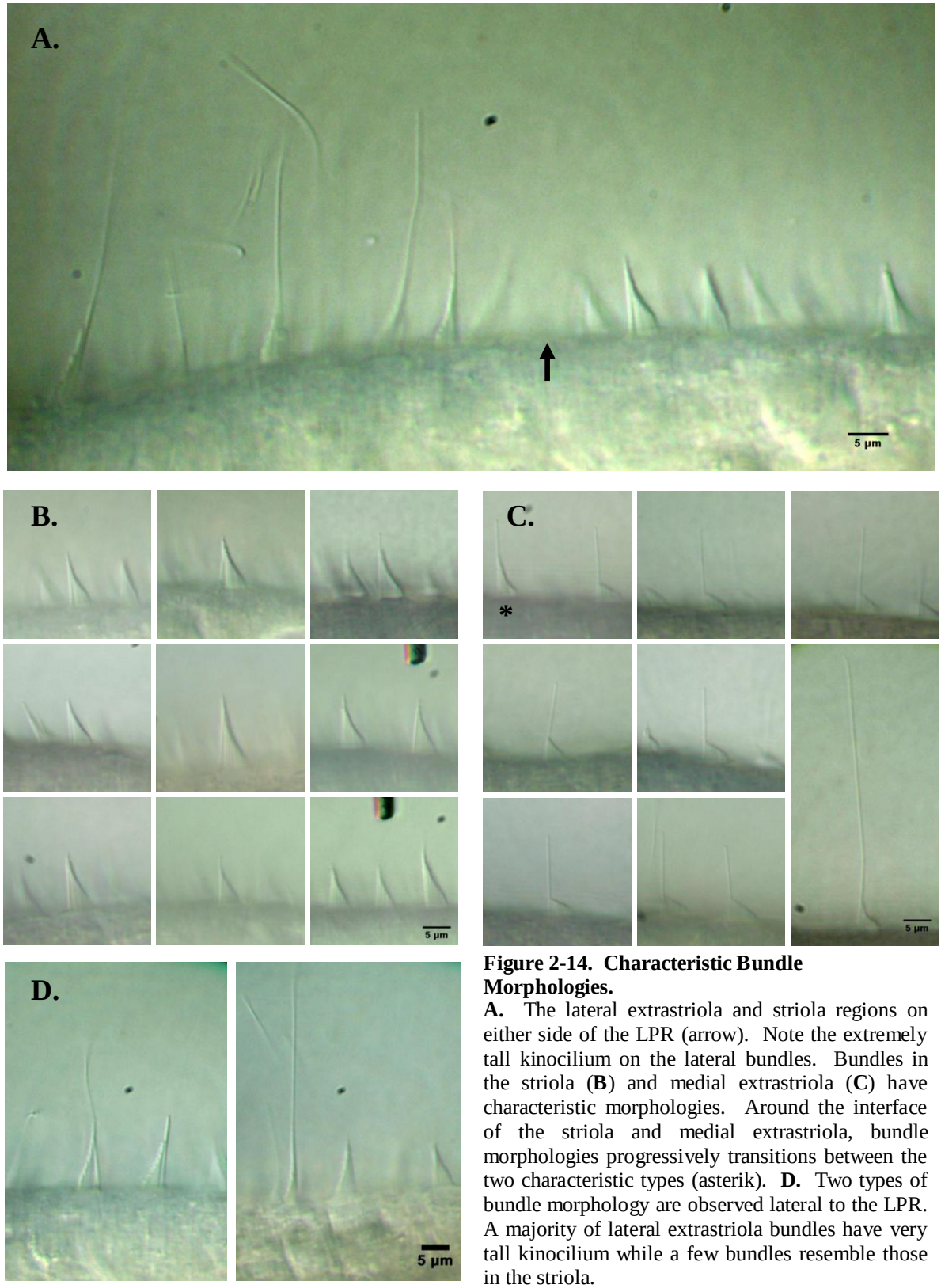

Figure 2-14. Characteristic Bundle Morphologies.
A. The lateral extrastriola and striola regions on either side of the LPR (arrow). Note the extremely tall kinocilium on the lateral bundles. Bundles in the striola (**B**) and medial extrastriola (**C**) have characteristic morphologies. Around the interface of the striola and medial extrastriola, bundle morphologies progressively transitions between the two characteristic types (asterik). **D.** Two types of bundle morphology are observed lateral to the LPR. A majority of lateral extrastriola bundles have very tall kinocilium while a few bundles resemble those in the striola.

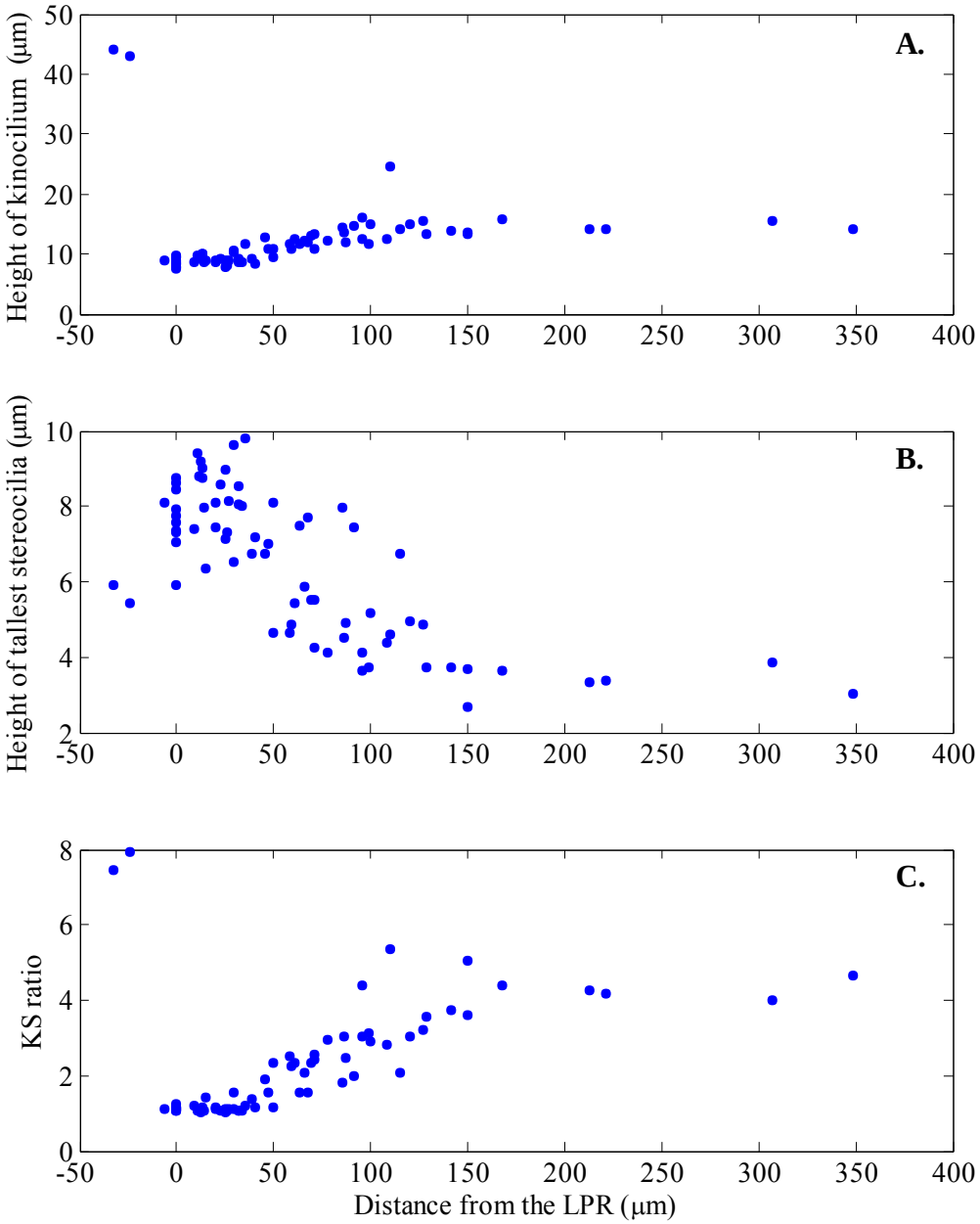

Figure 2-15 A-C. Bundle morphology varies with macular location.
Measurements of kinocilium and tallest stereocilia heights and calculations of the KS ratio change with distance from the LPR (x=0). Positive and negative LPR distances correspond to medial and lateral directions, respectively.

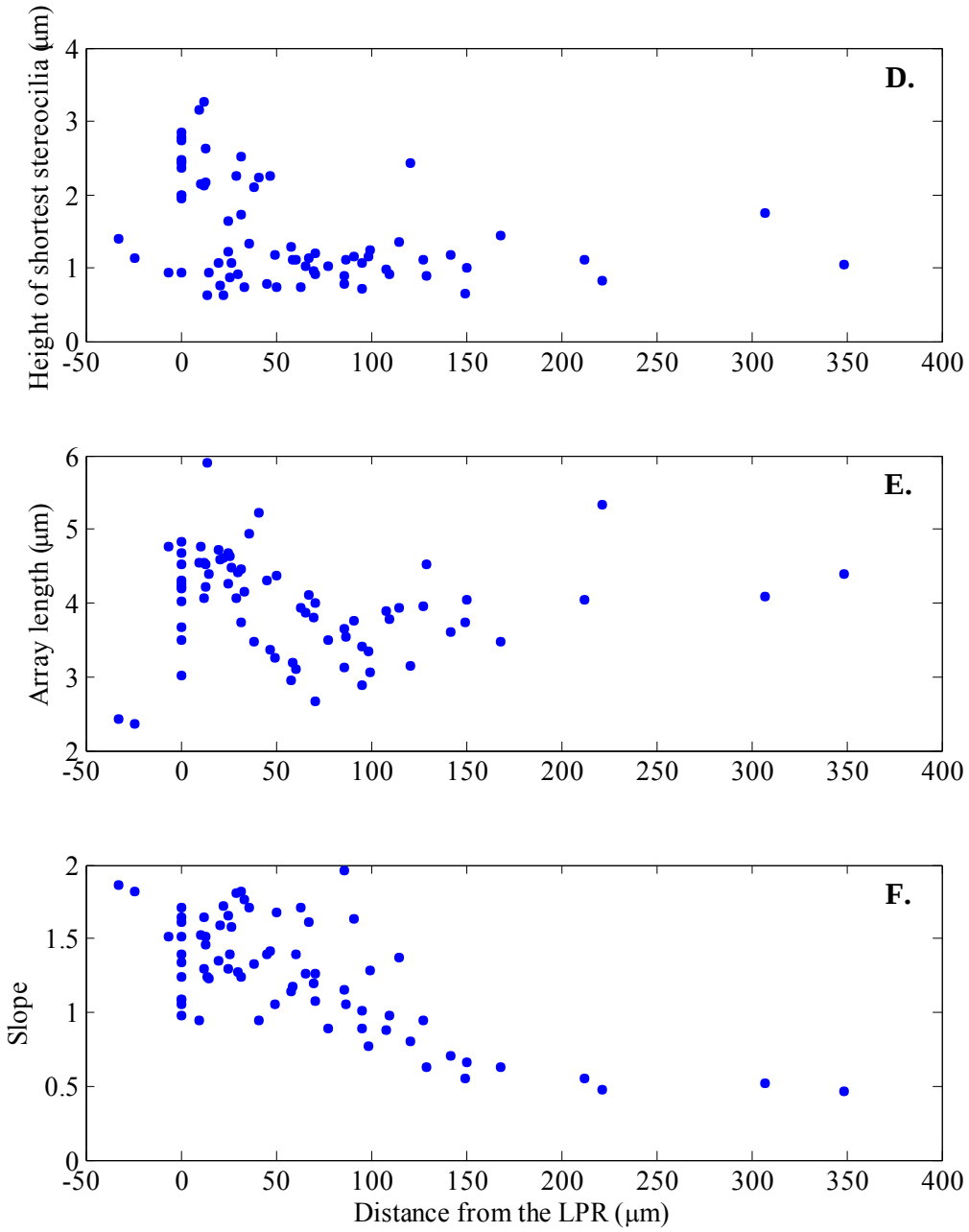

Figure 2-15 D-F. Bundle morphology varies with macular location.
Measurements of shortest stereocilia heights, array lengths and calculations of the slope change with distance from the LPR (x=0). Positive and negative LPR distances correspond to medial and lateral directions, respectively.

2.4.3 Bundle Stiffness vs. Morphology

The variation in bundle stiffness coincides with alterations in bundle structure along the medial to lateral transect. In Fig. 2-16, bundles with stiffness values greater than 50 μN/m are plotted in red while weaker bundles are blue. The plots demonstrate that the stiff and weak bundles have characteristic morphologies. Morphological distinctions between the stiff and weak bundles are clearly visualized when they populate distinct regions along the x-axis of the scatter plots. The three structural parameters which demonstrate the clearest distinction between stiff and weak bundles are the height of the kinocilium, height of the tallest stereocilia, and KS ratio. The stiffest bundles have short kinocilium, long tallest stereocilia, and KS ratios close to 1. The weaker bundles have KS ratios ranging from 1.6 - 8. Figure 2-17 further illustrates the morphological characteristics of the stiff and weak bundles.

The height of the shortest stereocilia, array length, and slope populate overlapping regions along the x-axis and demonstrate less clear distinctions between stiff and weak bundles. The shortest stereocilia of stiff bundles are often tall, but not always. Half of the stiff bundles had shortest stereocilia of 2 μm or greater. For the weaker bundles, all but three of the shortest stereocilia were less that 1.5 μm. The array lengths and slopes of the stiff and weak bundles have considerable overlap, but the stiff bundles tend to have longer array lengths and steeper slopes than the weak bundles.

The mean values of each of the 6 dimensions were significantly different between the weak and stiff bundle populations. The dimensional measurements and p-values for the statistical tests between the weak and stiff bundles are summarized in Table 2-3. The stiff bundles had significantly shorter kinocilium, taller stereocilia, longer array lengths, lower KS ratios, and steeper slopes than the weaker bundles. In addition, all of the stiff bundles were located in the striola within 50 μm from the LPR.

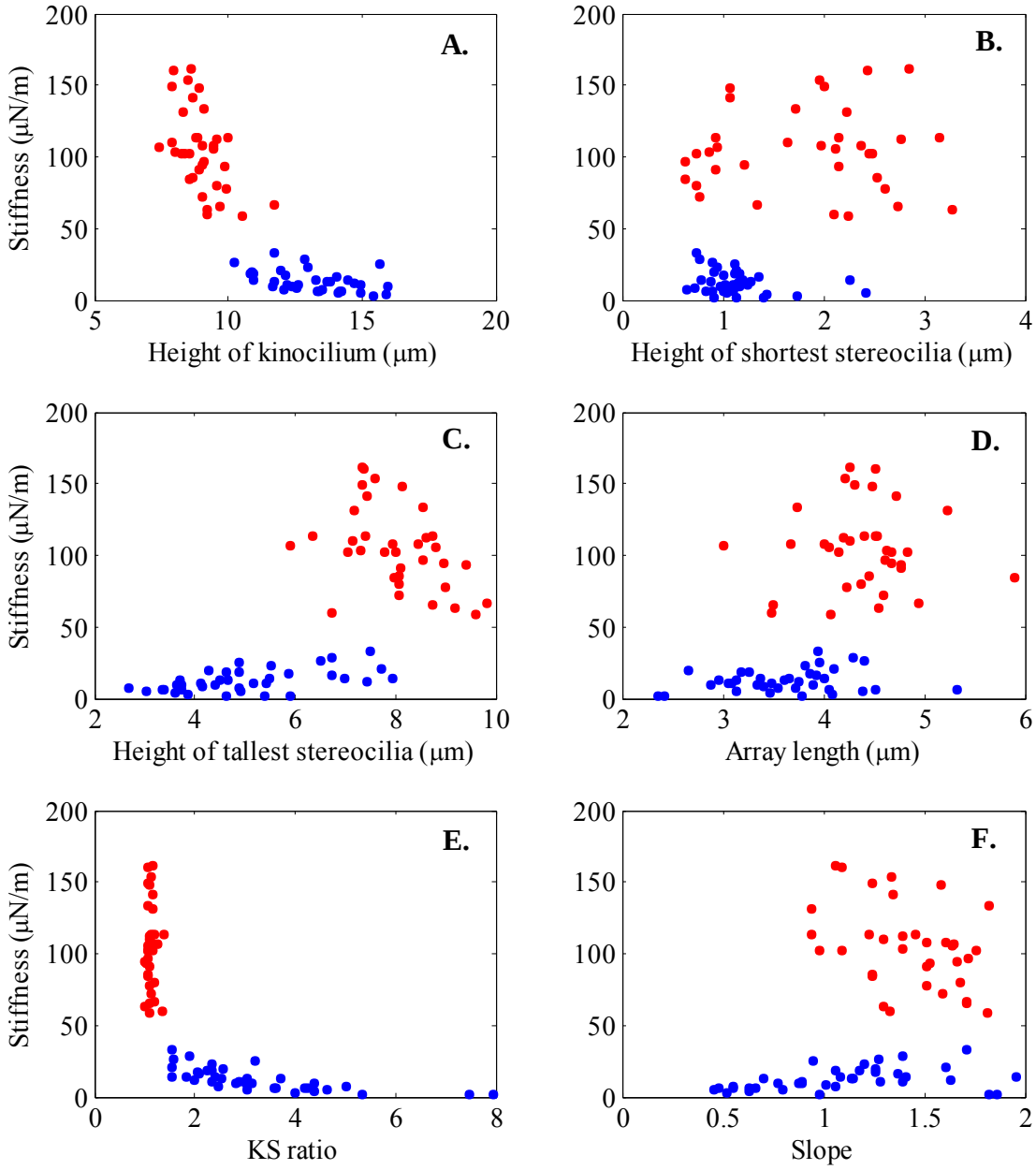

Figure 2-16. Bundle stiffness vs. dimensional parameters.
The stiffest bundles are plotted in red ($k \geq 50$ μN/m) and the weaker bundles are plotted in blue. Heights of the kinocilium, tallest stereocilia, and the KS ratio show clear morphological distinctions between stiff and weak bundles. Height of the shortest stereocilia, array length, and slope have less clear distinctions.

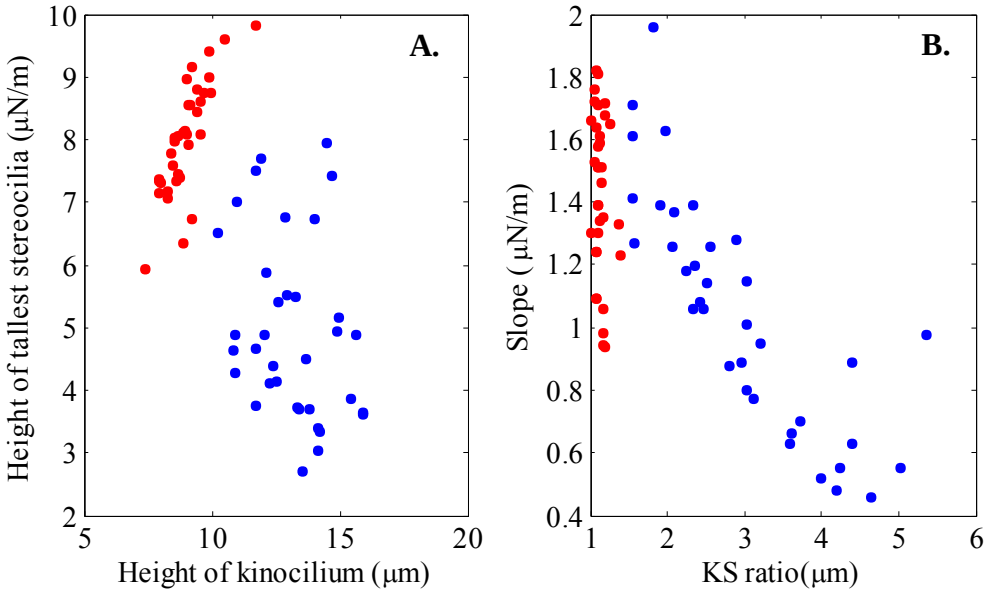

Figure 2-17. Comparing dimensional parameters of stiff and weak bundles. Bundles with stiffness greater than 50 μN/m are plotted in red and weaker bundles are blue. **A**. Stiff bundles have shorter kinocilium and long tallest stereocilia. **B.** The KS ratios of stiff bundles are approximately 1 and they have steeper slopes. In weaker bundles the slope decreased as the KS ratio increases.

	Stiff Bundles k > 50 µN/m (n= 35)	Weak Bundles k < 50 µN/m (n=38)	p-value
Kinocilium height			
mean ± std. dev.	9.0 ± 0.8	15.1 ± 7.2	< 0.0001
95% confidence interval	8.7 - 9.3	12.7 - 17.4	
range	7.4 - 11.7	10.2 - 44.1	
Tallest stereocilia height			
mean ± std. dev.	8.0 ± 0.9	5.0 ± 1.4	< 0.0001
95% confidence interval	7.7 - 8.3	4.5 - 5.5	
range	5.9 - 9.8	2.7 - 7.9	
Shortest stereocilia height			
mean ± std. dev.	1.8 ± 0.8	1.1 ± 0.4	0.0014
95% confidence interval	1.6 - 2.1	1.0 - 1.2	
range	0.6 - 3.3	0.6 - 2.4	
Array length			
mean ± std. dev.	4.4 ± 0.5	3.6 ± 0.6	< 0.0001
95% confidence interval	4.2 - 4.6	3.4 - 3.8	
range	3.0 - 5.9	2.4 - 5.3	
KS ratio			
mean ± std. dev.	1.1 ± 0.1	3.2 ± 1.5	< 0.0001
95% confidence interval	1.1 - 1.2	2.7 - 3.7	
range	1.0 - 1.4	7.9 - 1.5	
Slope			
mean ± std. dev.	1.4 ± 0.3	1.1 ± 0.4	0.0002
95% confidence interval	1.3 - 1.5	1.0 - 1.2	
range	0.9 - 1.8	0.5 - 2.0	
Distance from LPR			
medial range	0 - 50.1	29.7 - 348.9	--
lateral range	- 6.3 (n=1)	- 24.0, -32.5 (n=2)	

Table 2-3. Dimensional parameters for the stiff and weak bundle populations. The four measured and two calculated dimensional parameters are summarized and the range of their distances from the LPR given. All six parameters were significantly different between the weak and stiff bundles. The p-values from Wilcoxen ranked sum tests are given in the far right column.

2.5 Discussion

This work contributes three major findings. The first is that hair bundle stiffness varies systematically with macular location in the turtle utricle. Bundle stiffness progressively declines with distance from the LPR in both the medial and lateral directions. The striola bundles were found to be significantly stiffer than those in the extrastriola.

The second major finding is that bundle stiffness and structure co-vary. The stiffest bundles in the turtle utricle have short kinocilia and tallest stereocilia of approximately the same height. Their KS ratios are less than 1.5. The weakest bundles in the turtle utricle have tall kinocilium projecting far above the tallest stereocilia giving them KS ratios ranging from 1.6 to 8.0. Stiffer bundles also tend to have longer array lengths and steeper slopes than the weak bundles. The average stiffness of the stiff and weak bundle populations were 105 ± 29 μN/m (n=35) and 12 ± 8 μN/m (n=38), respectively.

Measurements of bundle stiffness from all three regions were taken over a short distance, roughly 2/5, of the central medial to lateral transect. The stiffest bundles, having stiffness greater than 50 μN/m, were all located within 6 μm lateral and 50 μm medial to the LPR. Stiffness within this region was fairly homogenous, but demonstrated a slight downward trend with increasing distance from the LPR. Around the interface of the striola and medial extrastriola regions, bundle morphology progressively transitioned. Within this region, kinocilium and KS ratios increased while bundle slopes and array length decreased with distance from the LPR. Bundle stiffness within this transition region decreased more rapidly with distance from the LPR. The medial extrastriola bundles demonstrated a leveling in stiffness decline for bundles located further than 150 μm from the LPR. Based on the consistency of bundle structure in the medial extrastriola, we expect that bundle stiffness would demonstrate no further decline beyond the point where our measurements ended. Previous work on the turtle utricle has shown that the location specific variation in bundle structure observed along the central medial to lateral transect also exists along posteriorly and anteriorly oriented radial transects (Xue and Peterson 2006). Consequently, we expect that the systematic variation in

bundle stiffness measured along the central transect would pivot about the medial end and fan across the macular surface.

The third major finding is that hair bundle stiffness in the turtle utricle is lower than values reported in literature for both the cochlear and vestibular organs of other species. The only exception is an early work that measured the stiffness of bullfrog saccule bundles in the range of 22 - 380 μN/m (Ashmore 1984). Extensive efforts were taken to verify the accuracy of our measurement system to ensure that the lower values of stiffness in the turtle utricle were not in error. These efforts included verification of the bead calibration technique for determining fiber stiffness, an imitation bundle study using calibrated glass fibers, repeated measurement of bundles over time and analysis of fluid drag on the fiber. All efforts produced positive confirmation of our results. Perhaps the most convincing evidence for the accuracy of our measurement system comes from the imitation bundle study. These results demonstrated that the stiffness of calibrated glass fibers could be measured with an error of $\leq 10\%$. Repeated measurements on bundles over time demonstrated that the error occasionally increased to 20% for measurements on actual bundles though one out of eight times the error was within 10%. A discussion of the reasonability of lower bundle stiffness in the turtle utricle is presented in the next sections.

2.5.1 Comparison to Previous Stiffness Measurements

The most common preparation for bundle stiffness measurements in the past has been the frog saccule. A majority of these measurements were made using the force deflection technique incorporating a glass fiber (Ashmore 1984, Howard and Ashmore 1986, Howard and Hudspeth 1987, Howard and Hudspeth 1988, Jarmillo and Hudspeth 1993, Marquis and Hudspeth 1997, Martin et al., 2000). The steady state stiffness of bullfrog saccule bundles measured by force deflection is typically around 600 – 700 μN/m. These reported values are the average stiffness of multiple bundles, and the standard deviations are large (220 – 360 μN/m). The average stiffness of unperturbed bullfrog saccule bundles, measured from the Brownian motion, was slightly lower at 341 μN/m, n=73 (Denk et al., 1989). The steady state stiffness of hair bundles from the turtle cochlea were also measured using the flexible glass fiber technique and yielded values

comparable to those from the bullfrog saccule (Crawford and Fettiplace 1985). The stiffness of the turtle cochlear bundles ranged from 200 – 1000 μN/m with an average of 590 ± 250 μN/m. Bundle stiffness has also been measured in a variety of mammalian species and in avians. These preparations include the guinea pig cochlea (Steriloff and Flock 1984), mouse cochlea and otolith organs (Kossl et al., 1990, Geleoc et al., 1997), rat cochlea (Langer et al., 2001), and chick cochlea and utricle (Szymko et al., 1992, Bashtanov et al., 2004). Several different measurement techniques were employed with these preparations including force deflection with a glass fiber, fluid jet stimulation, analysis of the Brownian motion, and atomic force microscopy. The results demonstrated that cochlear bundles in mammals are typically very stiff with values on the order of 10^3 μN/m. The cochlear and vestibular bundles from chick and vestibular bundles of the mouse had stiffness values similar to the steady state values in the bullfrog saccule and turtle cochlear.

The structure of hair cell bundles varies greatly among species, endorgans, and within a single endorgan. It is clear that these structural variations contribute greatly to the differences in bundle stiffness that are reported in literature. As our work demonstrates, the dimensional parameters of individual bundles impact their stiffness. The stiff bundles in the turtle utricle are similar to bullfrog saccule and turtle cochlea in general structure; they have hexagonal or circular stereociliary arrays and KS ratios close to one. In the following sections, the morphology of the three bundle types are discussed and compared. There are morphological differences that likely contribute to the lower bundle stiffness observed in the turtle utricle. Bundles with structures resembling the weaker extrastriolar bundle types in the turtle utricle have not previously been measured.

2.5.2 Comparison with Bullfrog Saccule Bundles

In the bullfrog saccule, two regionally organized bundle types are observed. The more predominate bundles are in the central region and have a consistent structure which is distinct from the peripheral 2 - 4 rows of bundles (Lewis and Li 1973, Hillman 1976, Lewis and Li 1975). The central bundles have kinocilium equal in height to the tallest stereocilia with a prominent bulb on the distal end. Measurements of bundle stiffness are

taken from these large types of bundles, and the location is frequently specified as the abneural margin of the sacculus (Howard and Ashmore 1986, Howard and Hudspeth 1987, Howard and Hudspeth 1988). The peripheral bundles in the bullfrog saccule have tall kinocilium (5 - 7 μm), short stereocilia (~1 - 3 μm) and no bulb (Hillman 1976).

Table 2-4 lists dimensional properties and stereocilia counts of bundles from the bullfrog saccule and the stiff bundle population from the turtle utricle. Unless specified, measurements were taken from DIC light microscope images of living hair cells. The measurements of the bullfrog saccule bundles are from large hair cells typical of those used for physiologic recordings (Jacobs and Hudspeth 1990). The mean heights of the tallest stereocilia are very similar between the two species, but the mean shortest stereocilia height in the bullfrog is almost twice that in the turtle. Bullfrog bundles also demonstrate a pronounced tenting evidenced by the angles of the tallest and shortest stereocilia. In the turtle utricle, the tallest and shortest stereocilia were almost perpendicular to the apical cell surface. The inter-stereociliary spacing in the bullfrog bundles is approximately 2 times greater than that in the turtle. The spacing is also approximately two times greater than the stereocilia diameter (~450 nm) in the bullfrog saccule bundles (Jacobs and Hudspeth 1990). Since the distal ends of the stereocilia are pulled together by tip and other interciliary links (Jacobs and Hudspeth 1990), the large spacing at the apical insertion contributes greatly to the observed tenting. The stereocilia counts of the bullfrog and striolar type II turtle bundles are both close to 60, however the less prevalent type I turtle bundles can have very high counts close to 100. Since bundles from the two species have similar stereocilia counts and the bullfrog stereocilia have greater spacing, it follows that the bullfrog bundles are relatively wider than in the turtle. The morphology of the bullfrog bundles are distinct from the turtle's in that the shortest stereocilia are quite tall, the outer stereocilia lean inward by 20-30 degrees from perpendicular, and the stereocilia are widely spaced. These characteristics, producing a large base with tented stereocilia, all suggest that the bullfrog saccule bundle would have a greater resistance to translational deflection, stiffness, than those in turtle utricle.

	Bullfrog Saccule	Turtle Utricle
Steady state bundle stiffness (μN/m)	~600 - 700	105 ± 29 (35)
Kinocilium height (μm)		9.0 ± 0.8 (35)
Tallest stereocilia height (μm)	8.4 ± 0.2 (20)	8.0 ± 0.9 (35)
Shortest stereocilia height (μm)	3.5 ± 0.2 (20)	1.8 ± 0.8 (35)
Angle of tallest stereocilia (degrees)	101 ± 1 (14)	~90
Angle of shortest stereocilia (degrees)	70 ± 2 (14)	~90
Inter-stereociliary spacing (μm)	0.94 ± 0.02 (14) [1]	0.48 ± 0.03 [3]
Number of stereocilia	60 ± 2 (20) [2]	zone 2-type II: 60.8 ± 8.3 (71) [3] zone 3-type II: 55.4 ± 11.2 (14) zone 3-type I: 95.9 ± 16.7 (94)

1. Mean spacing along a row of 4 - 5 stereocilia in a bundle's plane of bilateral symmetry.
2. Stereocilia counts were measured from freeze-fracture and transverse-section micrographs.
3. Measured from confocal micrographs taken at the base of utricular bundles from *Trachemys (Pseudemys) scripta*.

Table 2-4. Morphology of bundles in the bullfrog saccule and turtle utricle.
All dimensional measurements, except those footnoted with 2 and 3, were taken from DIC light microscope images of living hair cells. The angle of the tallest and shortest stereocilia is measured as the counter-clockwise angle from the apical cell surface. The morphologies of the bullfrog saccule were reported by Jacobs and Hudspeth 1990. Kinocilia heights were not specified for the bullfrog saccule bundles, but the bulbed kinocilium is known to be of equal height with the tallest stereocilia in these bundle types. The inter-stereociliary spacing at the base of the turtle utricular bundle was reported by Nam et al., 2006. The stereocilia counts in the turtle utricle are from Moravec and Peterson 2004. The dimensions of bundles in the turtle utricle are from the stiff population of bundles that have stiffness > 50 μN/m, KS ratios < 1.5, and are located within 50 μm from the LPR.

2.5.3 Comparison with Turtle Cochlear Bundles

Within the basilar papilla of turtle, there are four distinct bundle types which are regionally organized (Hackney et al., 1993). The basilar membrane portion of the papilla contains pyramidal shaped bundles in the central region and steeple-shaped bundles at the basal and apical ends. Bundles were classified as steeple shaped if they possessed steeper slopes than the pyramidal bundles and had heights two times greater than the bundle's base diameter. For both pyramidal and steeple shaped bundles, the kinocilium are approximately the same as the tallest stereocilia, and bundle heights vary from 7.5 - 8 μm at the apex to around 4.5 μm at the base. Bundles from the apical and basal limbal regions demonstrate tall kinocilium (10 - 14 μm) projecting far above tallest stereocilia (4 – 5 μm). Intermediate bundle shapes are observed between the basilar membrane and limbal regions of the papilla in which the KS ratios transition between the two extremes. Bundles in the basilar membrane region of the papilla contain between 60 – 100 stereocilia. The number of stereocilia has been shown to increase from 62 ± 3 in the apical fifth to 89 ±18 in the basal fifth of the region (Hackney et al., 1993). Stiffness measurements were taken of bundles located in the basilar membrane region of the papilla, though precise locations are not specified (Crawford and Fettiplace 1985).

The dimensional properties of the turtle cochlear bundles imaged with DIC light microscopy are not recorded in literature, so a comparison like that presented above is not possible. What we do know about the turtle cochlear bundles whose stiffness has been measured, is that their kinocilium heights were 6-7 μm (Crawford and Fettiplace 1985). This is 2 -3 μm shorter than the mean kinocilium height of the stiffest group of bundles in the turtle utricle (Table 2-4). From the experimentally collected data on turtle utricular bundles, stiffness increases greatly for small reduction in kinocilium height (Fig. 2-16A). Experimentally measured bundle stiffness in the turtle cochlea ranged from 200 - 1000 μN/m (Crawford and Fettiplace, 1985) while the stiff population in the utricle ranged from 58 – 161 μN/m. The kinocilium height vs. bundle stiffness results suggest that hair bundles in the turtle utricle may be less stiff than the cochlear bundles because their bundles are taller.

Chapter 3: Stiffness Contribution of Interciliary Links

3.1 Introduction

The stereocilia in the hair bundle are connected to each other and to the kinocilium through several different types of interciliary links. The location of these links, including the tip, kinocilia, horizontal top connectors, shaft and ankle connectors, are illustrated in Fig. 3-1. The tip links stretch at an angle from the distal ends of the stereocilia up to the side of a neighboring taller stereocilia (Osbourne et al., 1984, Pickles et al., 1984). Unlike the other types of links, all the tip links in a bundle are oriented in the same direction. They run parallel or up to ±30 degrees to the excitatory axis depending on whether their stereocilia demonstrate tight or loose packing, respectively (Bagger-Sjoback and Takumida 1988). Kinocilial links connect the kinocilium to the 4-5 neighboring stereocilia usually over a short distance near the tip of the bundle. In bullfrog saccule bundles, the kinocilial links are spaced at ~40 nm intervals over a 1 μm distance near the distal end of the kinocilium (Hillman 1969, Jacobs and Hudspeth 1990). In turtle auditory bundles, the kinocilial links are found at the distal tip and along the kinocilium shaft (Hackney et al., 1993). The horizontal top connecters join the distal ends of the stereocilia a short distance below the tip links. The horizontal top connectors have been observed in bullfrog saccule bundles (Jacobs and Hudspeth, 1990), in the striola bundles of the chick utricle (Goodyear and Richardson, 1992) and in the mouse cochlea (Goodyear et al., 2005). Shaft links are very fine strands connecting the membranes of neighboring stereocilia, and their distribution has been shown to vary between striola and extrastriola hair cells (Goodyear and Richardson 1992, 1999). In utricular chick bundles, shaft links are distributed over the entire surface of extrastriola bundles and are limited to the basal regions of striola bundles (Goodyear and Richardson 1992). The final type of link, the ankle link, connects stereocilia just above their apical insertions. They are described as web-like strands near the apical surface (Goodyear and Richardson 1992, 1999) approximately 1 μm from the cuticular plate (Jacobs and Hudspeth 1990).

Many studies have demonstrated that different sets of interciliary links are selectively removed with exposure to the Ca^{2+} chelator BAPTA and the proteolytic

enzyme subtilisin. The tip links are rapidly removed (within 10 sec) during BAPTA exposure which concurrently eliminates mechanotransduction in the cell (Assad et al., 1991, and Crawford et al., 1991). BAPTA exposure also removes the kinocilial links within 10 sec (Goodyear and Richardson 2003) and more gradually removes the ankle links (< 10 min) (Goodyear and Richardson 1999). The shaft and upper lateral connectors remain intact following BAPTA treatments. Shaft links are removed along with ankle links following 20 min exposure to the enzyme subtilisin (Goodyear and Richardson 1999). The tip, kinocilial and horizontal top connectors resist digestion from the protease subtilisin (Goodyear and Richardson 1999, 2003).

A study performed by Bashtanov et al., 2004, took advantage of the selective removal of the interciliary links to determine their contributions to the overall bundle stiffness. Utricular striola bundles in the chick were independently and sequentially

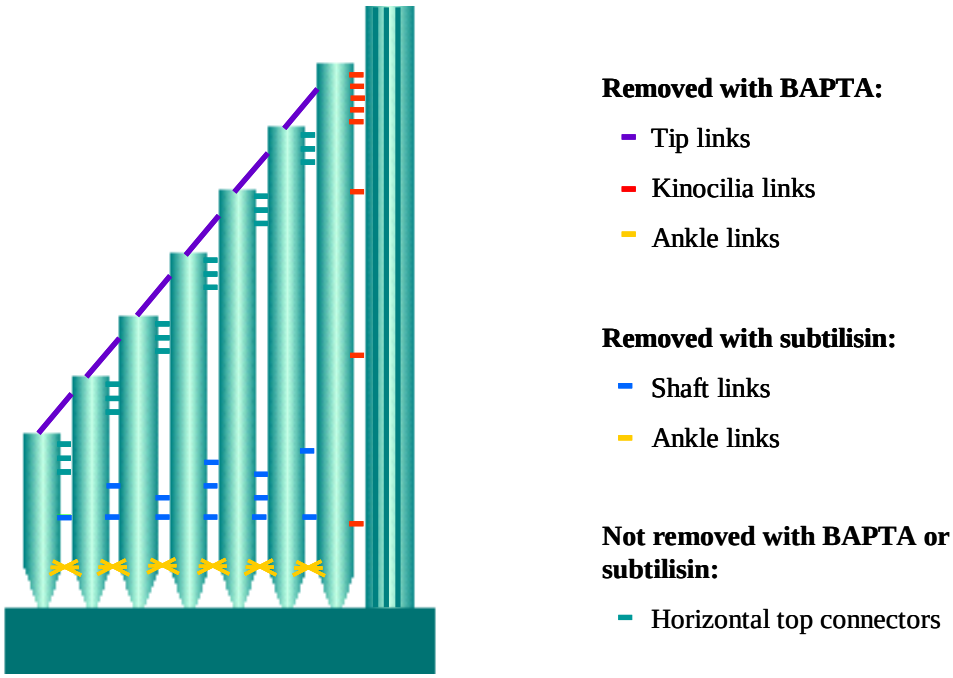

Figure 3-1. Illustrations of the interciliary links in a hair bundle.
Five types of intercilliary links are found in hair cell bundles. The tip, kinocilia and ankle links are broken from exposure to the Ca^{2+} chelator BAPTA. Shaft and ankle links are broken from exposure to the protease subtilisin. The upper lateral links are not sensitive to either BAPTA or subtilisin.

treated with BAPTA and subtilisin. Bundle stiffness was measured before and after the treatments to determine the resulting percent reduction. The reduction of stiffness following BAPTA treatment demonstrated that the tip, kinocilial and ankle links jointly contribute 43% to the overall bundle stiffness. Reduction following subtilisin treatment indicated that the combined contribution of shaft and ankle links is 48%.

The current study repeats the work of Bashtanov et al., 2004, on striola bundles in the turtle utricle. The same concentrations of BAPTA and subtilisin were used to treat the hair bundles and a similar protocol was followed. The methods for measuring bundle stiffness are quite different. Bashtanov et al., used DIC interferometry to measured the Brownian motion of unperturbed bundles. Bundle stiffness in the turtle utricle was measured with a force deflection technique incorporating a flexible glass fiber. The chick striola bundles have greater stiffness (900 ± 500 μN/m, n=102) than those in the striola of the turtle as presented in chapter 2 (82 ± 46, n=48)

We sought to measure the stiffness contribution of the interciliary links so that species specific information could be incorporated into a finite element model of a hair cell from the turtle utricle (Nam et al., 2006, Grant et al., 2007). In addition, we sought to demonstrate that the interciliary links were intact in our preparations of the turtle utricle. Our bundle stiffness measurements from the turtle are lower than those of other species reported in literature, so it was desirable to demonstrate that the interciliary links were not damaged. A reduction in stiffness following BAPTA and subtilisin treatments comparable to that observed in the chick utricle provides strong evidence that the interciliary links are initially intact in our experimental preparations.

3.2 Methods

3.2.1 Preparation and Solutions

Turtle utricles were prepared as described in the methods of chapter 2. Once excised, the utricles were folded along a medial to lateral transect and pinned. The otoconial membrane was peeled away, and the bundles were viewed from the side. A total of six preparations were used for this study: two for each of the BAPTA and subtilisin treatments and two for controls. All measurements were made on striola bundles.

Two types of Hank's Balanced Salt Solutions (HBSS) were purchased for use in these experiments: standard HBSS and Ca^{2+} and Mg^{2+} free HBSS (Gibco, Invitrogen). Both solutions were buffered with 10mM HEPES and were titrated with NaOH to a pH of 7.2. Their osmolarity was 300 mOsm. The buffered standard HBSS was used to maintain solutions during dissections and during initial stiffness measurements. The standard HBSS was also used to prepare a 50 mg/L solution of subtilisin (Protease Type XXIV, Sigma-Aldrich) approximately 4 hours prior to use. Preparation of the BAPTA treatment required a Ca^{2+} free solution. For this, the buffered Ca^{2+} and Mg^{2+} free HBSS was used with 0.9 mM $MgCl_2$ added. A 5 mM solution of BAPTA (1,2-bis(2-Aminophenoxy)ethane-N,N,N',N'-tetraacetic acid tetrasodium salt, Sigma-Aldrich) was prepared in the Ca^{2+} free HBSS solution. The BAPTA solution was prepared in plastic containers on the day of the experiment and was protected from light. All solutions were perfused with medical grade oxygen prior to specimen exposure.

The compositions of the purchased HBSS solutions are as follows: standard HBSS contained 1.26 mM $CaCl_2$, 0.493 mM $MgCl_2$, 0.407 $MgSO_4$, 5.33 mM KCl, 0.441 mM KH_2PO_4, 4.17 mM $NaHCO_3$, 137.93 mM NaCl, 0.338 mM Na_2HPO_4, 5.56 mM D-Glucose, and no phenol red. The Ca^{2+} and Mg^{2+} free HBSS contained 5.33 mM KCl, 0.441 mM KH_2PO_4, 4.17 mM $NaHCO_3$, 137.93 mM NaCl, 0.338 mM Na_2HPO_4, 5.56 mM D-Glucose, and no phenol red.

3.2.2 Stiffness Measurements

Measurements of bundle stiffness were made using the force-deflection technique discussed in chapter 2. Initial stiffness measurements were made while specimens were bathed in buffered HBSS prior to treatment with BAPTA or subtilisin. Following treatments, measurements were repeated up to 3 hours or until the bundles demonstrated visible signs of damage. This resulted in 3-6 measurements per bundle. As described in chapter 2, each stiffness measurement is an average of 3-5 trials in which the bundle was sinusoidally deflected for 30 seconds at a peak-to-peak amplitude of 1 μm and 0.5 Hz. Stiffness measurements were taken as frequently as possibly while alternating between two bundles (ie. 3-5 trials on one bundle followed by 3-5 trials on a second bundle, then back to the first). As a result, the time increments between measurements are not constant. On average, the acquisition time for 3-5 trials was 8 minutes.

After the initial stiffness measurements in standard HBSS, the fluid in the slide compartment (≈1.5 mL) was exchanged with the treatment solutions at a rate of 0.5 mL/min using a peristaltic pump. Prior to the BAPTA treatment, the chamber was flushed with Ca^{2+} free HBSS to prevent chelation of Ca^{2+} in the standard HBSS that would dilute the treatment. Because standard HBSS is the stock for the subtilisin solution, a flush was not required prior to its exchange. To ensure a complete and undiluted exchange with treatment solution, 3 times the volume of the fluid compartment was pumped through the slide. The exchange process required 9 minutes. The exposure time record started with the beginning of the exchange. Once the fluid exchange was completed, the pump supplying fresh oxygenated solution was shut off for the remainder of the experiment. Control experiments in HBSS demonstrated that this deprivation of oxygen did not induce a decline in bundle stiffness.

3.2.3 Control Experiments

Separate control experiments were performed for both the subtilisin and BAPTA treatments. For the subtilisin control, preparations were bathed in buffered HBSS. The BAPTA control was performed in Ca^{2+} and Mg^{2+} free Hanks' Balanced Salt Solution with 0.9 mM $MgCl_2$ and 10mM HEPES added, the base solution for the BAPTA treatment. Initial stiffness measurements for both controls were performed in the

buffered HBSS. The fluid in the experimental chamber was then exchanged with fresh buffered HBSS and Ca^{2+} free HBSS for the subtilisin and BAPTA controls, respectively. Stiffness measurements were then repeated 5 times over the course of approximately 3 hours.

3.3 Results

3.3.1 Buffered HBSS Control

The stiffness of two bundles bathed in buffered HBSS demonstrated no reduction in stiffness over 3 hours of measurement. Figure 3-2 shows the stiffness measurements normalized to the initial value. All but one of the measurements were within ±18% of the initial value. The exception was a 30% increase from the initial value. As discussed in chapter 2, the error of our bundle stiffness measurements was quantified as 20%. Except for the 30% increase, the stiffness change of all measurements were within the range of expected error. We conclude that the bundle stiffness did not decrease over the course of 3 hours while bathed in buffered HBSS. Pictures of the bundles taken after the initial measurements and 5 hours later are shown in Fig. 3-3. The appearance of the bundles did not change with time, and no visible signs of damage are observed.

3.3.2 Calcium Free HBSS Control

Following exposure to Ca^{2+} free HBSS, measurements of a bundle over time showed a gradually decline in stiffness (Fig. 3-2). The measurements taken in the first 80 minutes of exposure show a maximum 16% decline in stiffness. Since the percent change is still within the 20% expected error range, it does not conclusively indicate an actual decline in bundle stiffness. The downward trend continues, however, and by 170 minutes there is a definite stiffness reduction of 50%. The appearance of the bundle tested also changed with prolonged exposure to Ca^{2+} free HBSS. Figure 3-3 shows that after 3 hours of exposure the bundle leaned backwards about 15 degrees and a small bleb appeared behind the kinocilium. The leaning may have contributed to the decrease in measured stiffness.

The mechanism for stiffness reduction due to a lack of calcium is not known. However, the results demonstrate that the lack of calcium for prolonged periods of time can impact the bundle integrity and stiffness. As a result, it is difficult to tease apart the reduction in stiffness caused by a lack of Ca^{2+} and that caused by the presence of the chelator BAPTA. The removal of tip links following BAPTA exposure occurs very rapidly (Assad et al., 1991). For this reason and in consideration of the long term effect of Ca^{2+} deprivation, only the first post treatment measurements were used to determine the reduction in bundle stiffness from BAPTA exposure. The first post treatment measurements were taken within 20 – 40 minutes from the start of the exchange.

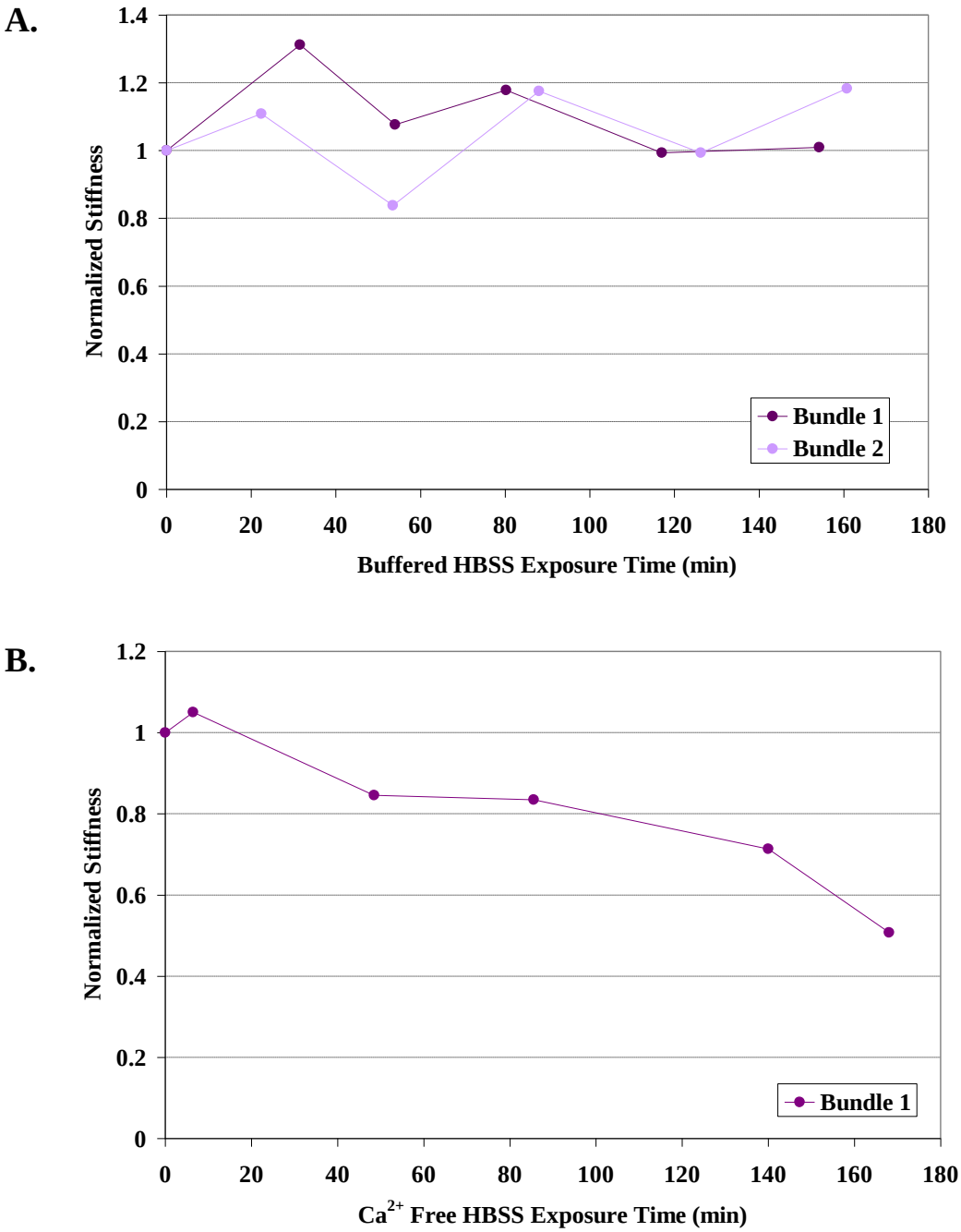

Figure 3-2. Normalized stiffness measurements over time for <u>control</u> experiments. Stiffness measurements were normalized to the initial stiffness value. **A.** The stiffness of bundles did not change with prolonged exposure to buffered HBSS. **B.** Bundles exposed to Ca^{2+} free HBSS demonstrated a gradual decline in stiffness.

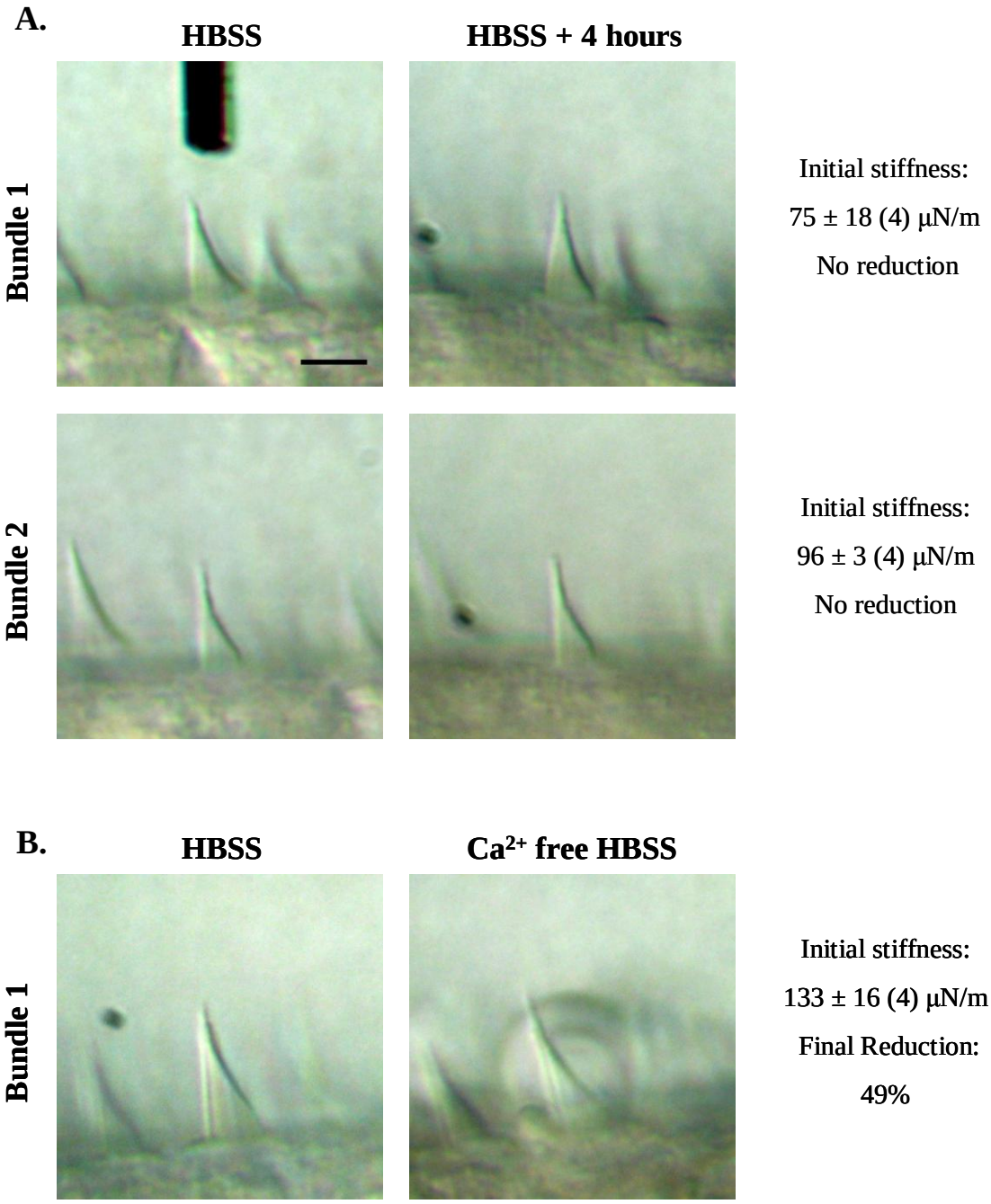

Figure 3-3. Pictures of tested bundles before and after control experiments.
A. Two bundles before (left) and after (right) exposure to buffered HBSS had no visible signs of alteration. **B.** The bundle was visibly altered following prolonged exposure to Ca^{2+} free HBSS; the bundle leaned backwards and a small bleb formed behind the kinocilium. Larger blebs in different focal planes distort the image. The scale bar in the upper left (5 μm) applies to all.

3.3.3 Subtilisin

Stiffness measurements of four bundles were made before and after treatment with subtilisin. In all four bundles, the treatment resulted in a stiffness reduction (Fig. 3-5). Figure 3-4 shows the stiffness measurements normalized to the pre-treatment value. A large reduction in stiffness was observed in measurements taken at least 60 minutes from the initial exposure. The percent reductions of individual bundles were found by averaging measurements of each bundle taken after 60 minutes exposure. For bundles 1 – 4, the stiffness reduction was 68, 47, 68 and 70 %, respectively. The average reduction of the 4 bundles resulting from subtilisin treatment was 63 ±11 %.

Pictures of the tested bundles were taken before subtilisin treatment, while bathed in HBSS, and after 3 hours of subtilisin treatments (Fig. 3-6). In the 1st, 2nd, and 4th bundles, visible damage to the bundles and surrounding epithelium is observed. The damage is indicated by blebs on the bundle, and sectioning or splitting of the bundle. Measurements were terminated with visible signs of bundle damage.

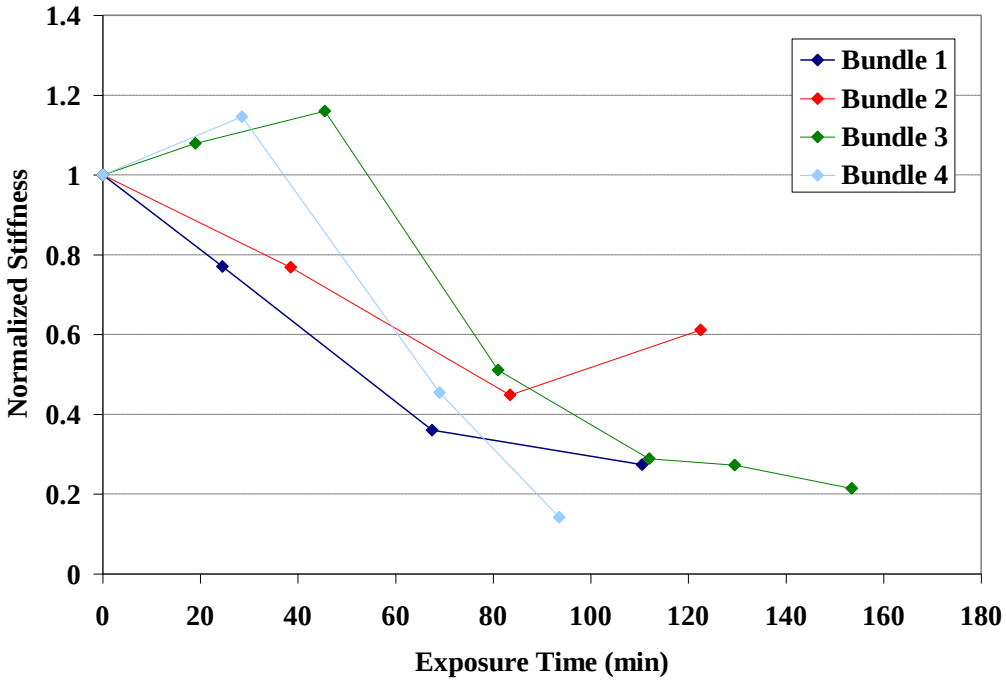

Figure 3-4. Normalized stiffness of four bundles exposed to subtilisin.
Stiffness measurements were normalized to the initial measurements taken in buffered HBSS.

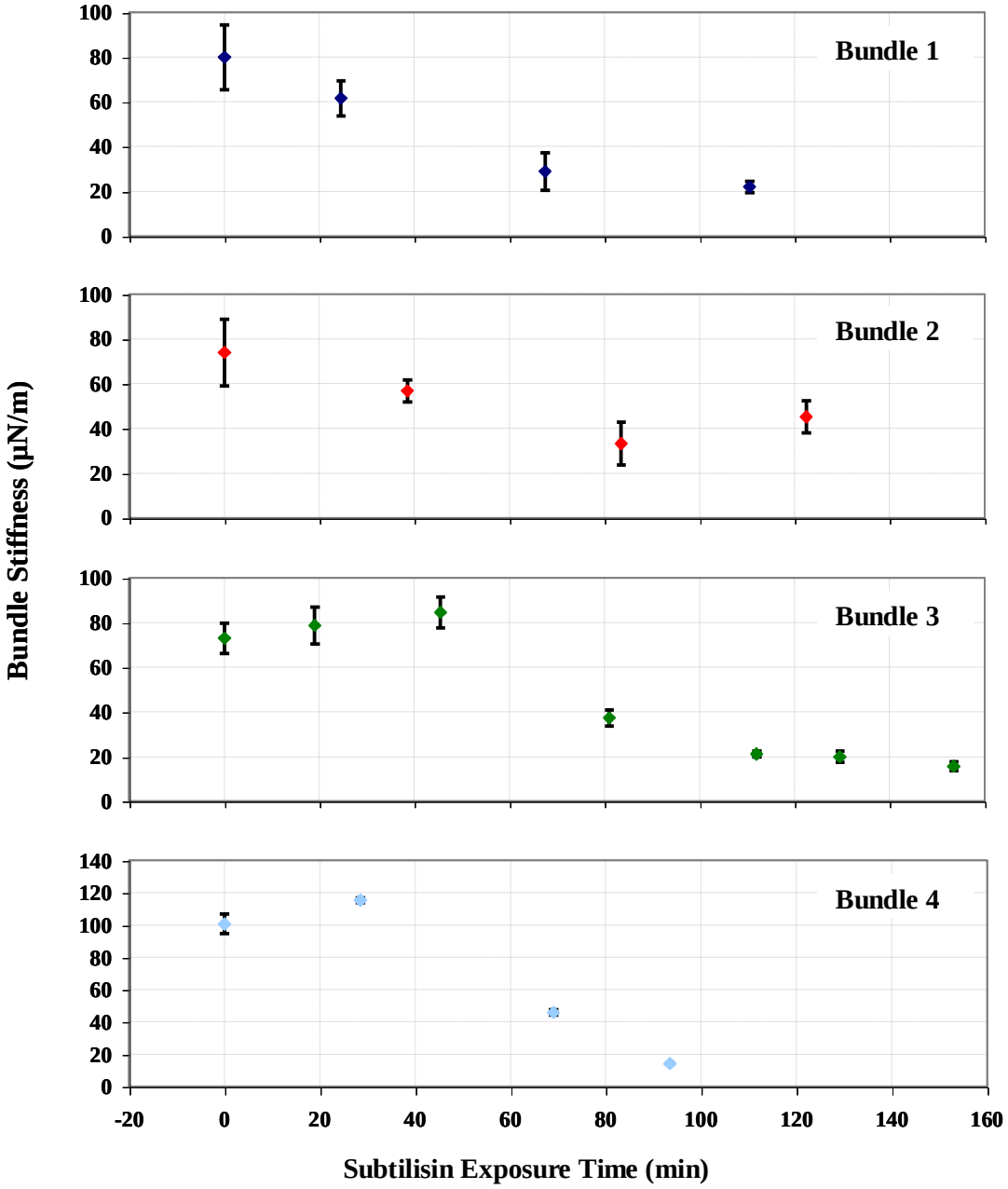

Figure 3-5. Reduction in stiffness of four bundles during exposure to Subtilisin. Each data point is the average stiffness of 3-4 trials plotted at the mid time point for the duration of those trials. The error bars represent the standard deviation of the trials. The initial stiffness measurements made in buffered HBSS prior to subtilisin exposure are plotted at 0 min.

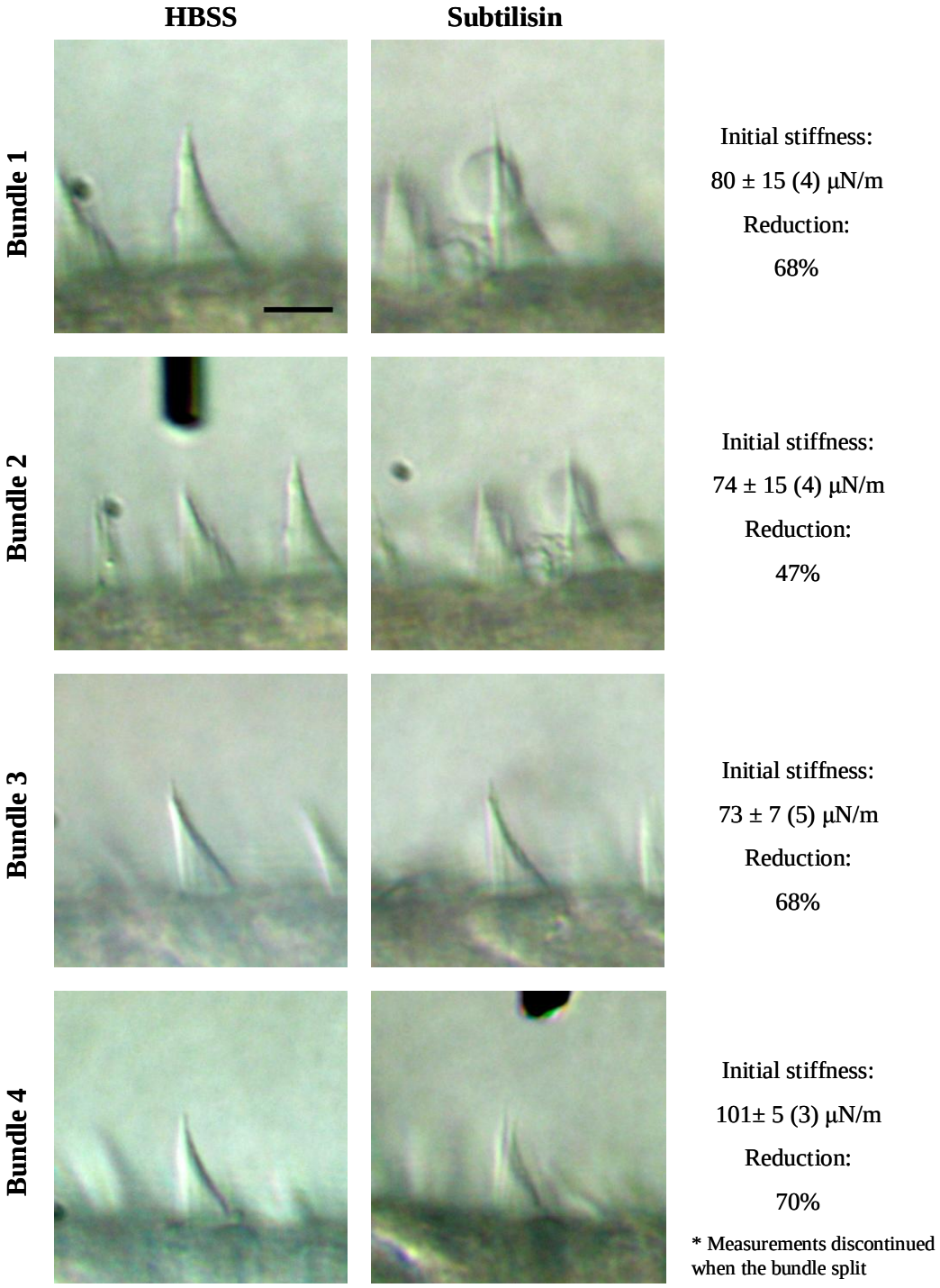

Figure 3-6. Pictures of four bundles before and after subtilsin exposure.
Pictures taken prior to treatments (left) were taken while the bundles were bathed in buffered HBSS. After 3 hours of subtilisin treatment, visible signs of bundle damage are observed in bundles 1, 2, and 4 (right). The percent reduction in stiffness is the average of the measurements taken after 60 minutes of exposure. The scale bar in the upper left image (5 µm) applies to all.

3.3.4 BAPTA

Stiffness measurements of four bundles were taken before and after treatment with BAPTA. Within the time required to take the first post treatment measurement (20 – 40 minutes), the stiffness of all the bundles was greatly reduced (Fig. 3-8). Additional measurements in time showed no further decline. Measurements of treated bundles normalized to the initial measurement in buffered HBSS are shown in Fig 3-7. The first post treatment measurements of bundles 1 – 4 had stiffness reductions of 53, 70, 75 and 62 %, respectively. The average reduction of the four bundles following BAPTA exposure was 65 ± 10 %.

Pictures of the tested bundles before treatment and after 2.5 – 3 hours of BAPTA exposure are shown in Fig. 3-9. For all bundles tested, there are no visible signs of bundle damage resulting from the BAPTA treatments. However, it should be noted that exposure to BAPTA resulted in considerable bleb formation on the surface of the epitheliums tested. Observations regarding blebs are briefly discussed at the end of the chapter.

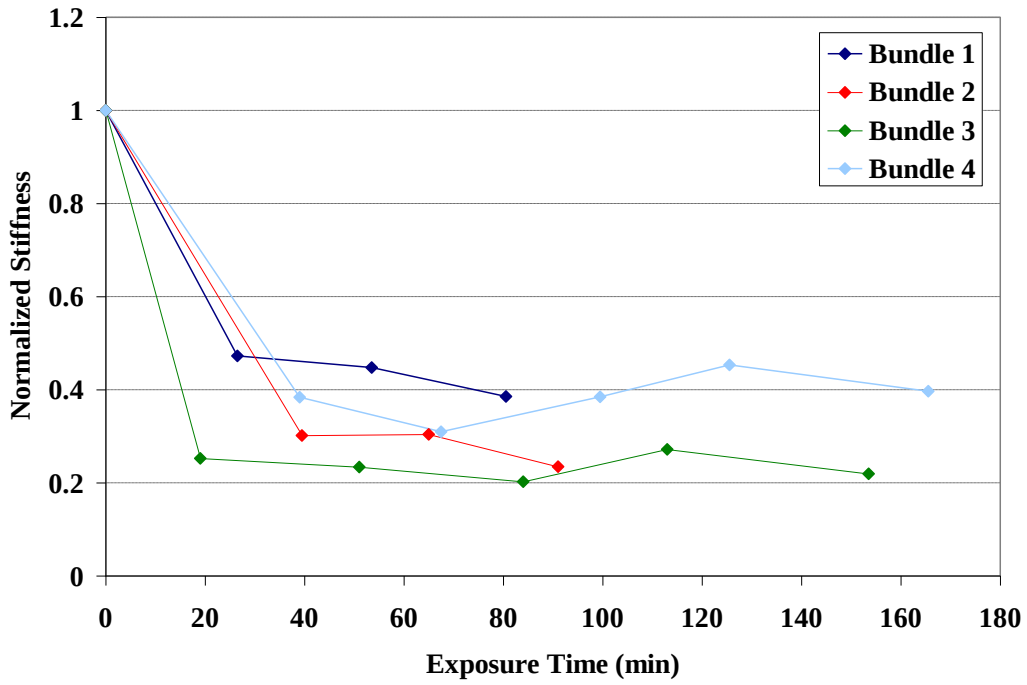

Figure 3-7. Normalized stiffness of four bundles exposed to BAPTA.
Stiffness measurements were normalized to the initial measurement taken in buffered HBSS.

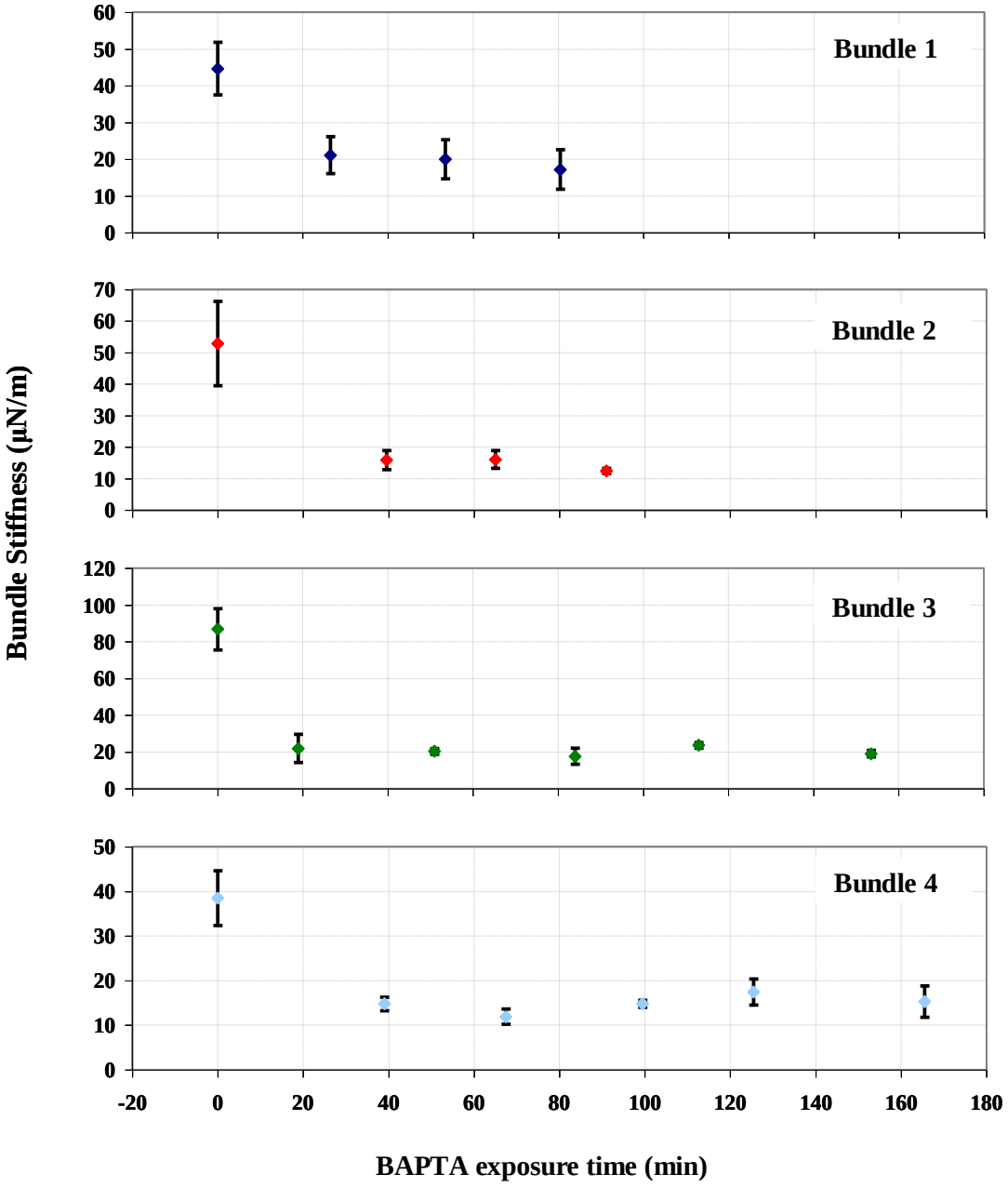

Figure 3-8. Reduction in stiffness of four bundles during exposure to BAPTA. Each plotted point is the average stiffness of 3-4 trials plotted at the mid time point for the duration of those trials. Error bars represent the standard deviation of those trials. The initial stiffness measurements made prior to BAPTA exposure are plotted at 0 min.

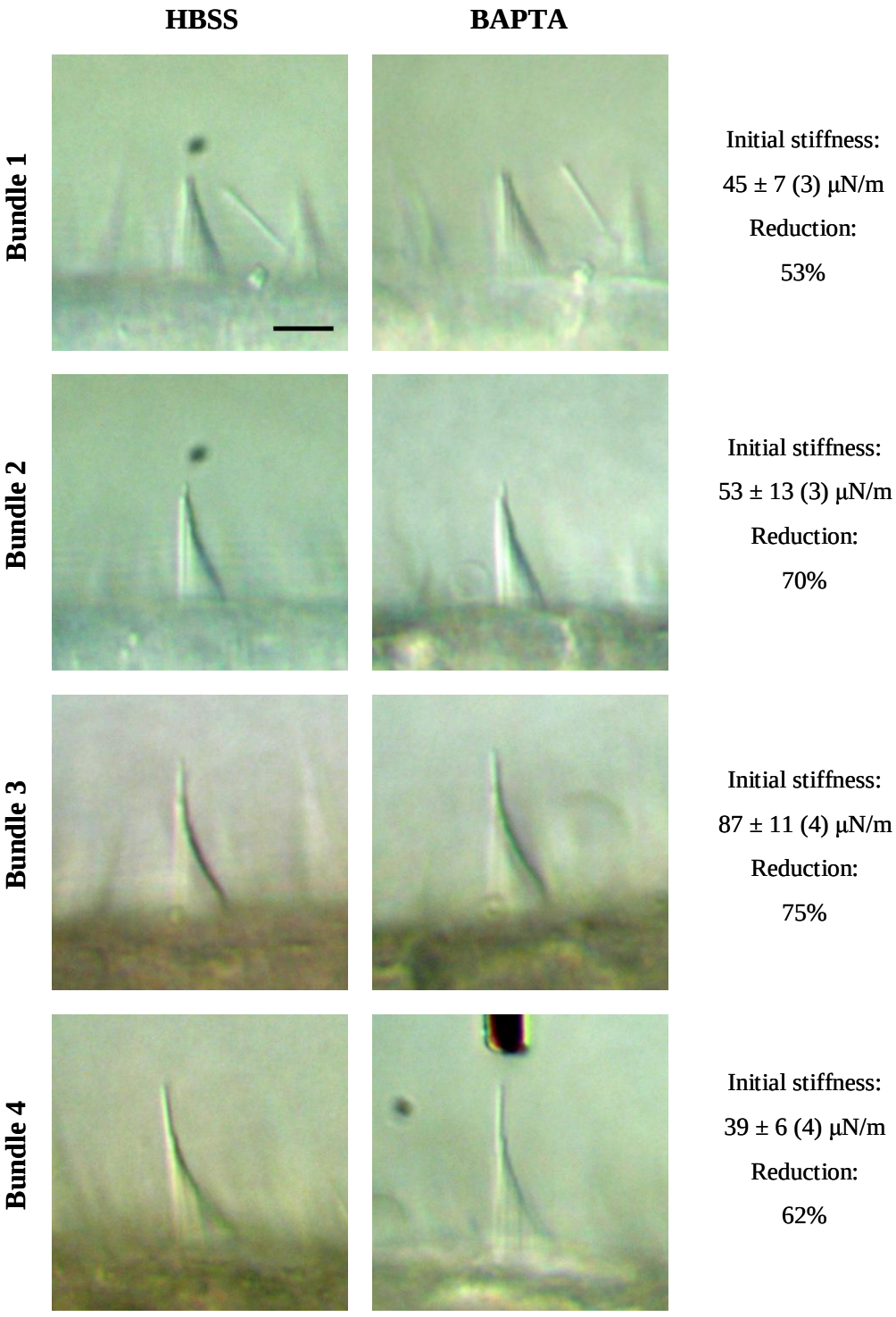

Figure 3-9. Pictures of bundles before and after BAPTA exposure. Pictures in the left column were taken after the initial measurements in buffered HBSS. Those in the right column were taken after BAPTA exposure. The images demonstrate that there were no signs of severe damage in the tested bundles. Small blebs are seen near bundles 2 and 3. The percent reductions of the first measurements taken following BAPTA exposure are presented. The scale bar in the upper left picture (5μm) applies to all.

3.4 Discussion

3.4.1 Stiffness Reduction

When turtle utricular bundles were treated with subtilisin, a reduction in stiffness occurred somewhere between 40 and 60 minutes of exposure. The average reduction in bundle stiffness after 1 hour of exposure was 63 ± 11% of the initial value. Bashtanov et al., 2004 measured a 48% reduction in the stiffness of chick utricular bundles following 40 minutes of subtilisin exposure. Measurements made up to 90 minutes after the initial exposure demonstrated a further decline of less than 25% (Bashtanov et al., 2004).

Following BAPTA treatment, the stiffness of turtle utricular bundles reduced by 65 ± 10% in the time required to make the first post treatment measurement (20-40 min). The stiffness of the chick utricular bundles were reduced by 43% following just 10 minutes of treatment and showed no significant reduction in stiffness up to 30 additional minutes of BAPTA exposure. The static stiffness of bullfrog saccular bundles following treatment with 5 mM BAPTA also demonstrated approximately 40 – 70% reduction from initial measurements (Marquis and Hudspeth, 1997).

The reduction in bundle stiffness following BAPTA and subtilisin treatments in the turtle utricle are greater but comparable to those measured by Bashtonov et al., 2004, for the chick utricle. We measured a slightly greater reduction in stiffness due to BAPTA than for subtilisin treatment which was reversed for measurements in the chick utricle. Our sample sizes, however, were considerably smaller (4 vs. 27-35), so a rigorous comparison is not appropriate. Overall, these results provide strong evidence that the interciliary links are intact in our turtle utricle preparations and are not inadvertently damage during removal of the otoconial membrane.

3.4.2 Observations on Bleb Formation

With exposure to Ca^{2+} free media and BAPTA solution, spherical blebs were observed on the surface of the epithelium. Within 15 minutes of exchange with Ca^{2+} free HBSS, there were blebs behind the kinocilium of many bundles. These are also noticed with BAPTA treatments. The blebs appear smooth, clear, and are on average 8 microns in diameter (Fig 3-10). They appear to grow over time and were found predominately in

the striola. Shi et al. 2005 discusses bleb formation on inner hair cells bathed in standard artificial perilymph due to an influx of Na^{+}. They reported that the blebs occurred without signs of cellular apoptosis or necrosis. The blebs observed in our preparation match the description of those observed by Shi et al. with respect to size and position behind the kinocilium. We are not certain what mechanism is responsible for the bleb formation or how a lack of Ca^{2+} in solution would produce results similar to those seen due to an influx of Na^{+}.

Figure 3-10. Bleb formation in calcium free solution.
During exposure to Ca^{2+} free HBSS and BAPTA solutions, blebs quickly formed on the surface of the epithelium behind the kinocilium.

Chapter 4: Mechanical Properties of the Kinocilium

4.1 Introduction

Vestibular hair bundles are composed of multiple stereocilia and a single kinocilium. The stereocilia are arranged in rows of increasing height with the kinocilium eccentrically positioned at the tall end of the bundle. During early stages of development, the kinocilium is present in hair bundles of all types; being centrally located among immature stereocilia before migrating to one side of the cell (review: Goodyear et al., 2006). In many species, including mammals and birds, the kinocilia of cochlear bundles are lost during maturation. Kinocilia in the extrastriola or peripheral regions of otolith organs and in the semicircular canals can be markedly taller than the stereocilia. In turtle utricle, the height of the kinocilia varies with location from about 10 μm in the striola, approximately the same height as the tallest stereocilia, to heights of 40+ μm laterally (Fontilla and Peterson, 2000, Peterson and Xue 2006). Kinocilia in canal bundles can reach heights of 100 μm.

The presence of a kinocilium is not a prerequisite for hair cell mechanotransduction as is readily observed in mammalian cochlear bundles. Additionally, this was demonstrated in the bullfrog saccule by detaching the kinocilium from the adjacent stereocilia without dislocating its apical insertion. (Hudspeth and Jacobs 1979). Deflections in the excitatory direction and even stretching of the separated kinocilium produced no intracellular receptor potential. With the kinocilium held flat against the epithelium, deflection of the stereociliary portion of the bundle produced normal receptor potentials. These results support the notion that the role of the kinocilium in mature bundles of vestibular organs is to transmit deflection of the otoconial membrane and cupula to the rest of the bundle. The kinocilia and basal body have been shown to have a role in development (Shobkowicz et al., 1995).

The kinocilium possesses a microtubule core which makes it the only true cilia in the hair cell bundle (Lewis et al., 1985). The term stereocilia is a misnomer since these structures are composed of actin fibrils. The kinocilium core consist of nine doublet tubules in a circumferential periphery surrounding 0 - 2 single tubules. The presence of

central tubules varies with species (Wersäll and Bagger-Sjöbäck 1974, Lewis et al., 1985), and in some cases reportedly varies along the kinocilium shaft (Engstrom et al., 1972, Kikuchi et al., 1989, Kikuchi et al., 1988). The 9+2 microtubule arrangement, also called the axoneme, is the classic configuration of motile or beating cilia such as the sperm flagellum and cilia of the respiratory tract (Fig. 4-1) (Cooper 2000). The 9+2 kinocilium configuration is found in the vestibular hair bundles of turtles (unpublished, Dr. Peterson), and fish (Flock and Duval 1965). In mammals, the central tubules can be lacking or incomplete as seen in vestibular bundles of guinea pig and mice (Kikuchi et al., 1989, Kikuchi et al., 1988). In the cochlea of mice, while present, a majority of kinocilia demonstrate a 9+0 form and a smaller percentage (3-14%) have a 9+2 form (Sobkowicz et al., 1995). The same study showed that immature and regenerating kinocilia frequently displayed an 8+1(double) arrangement where a peripheral doublet tubule apparently displaced to the center of the structure.

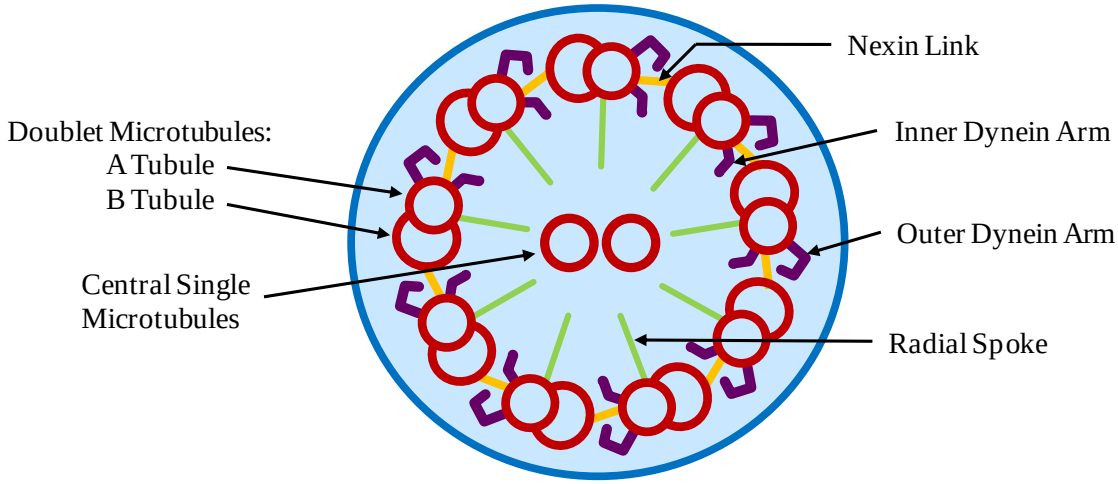

Figure 4-1. Structure of the 9+2 axoneme in cilia.
A diagram illustrating a cross section of the axoneme. Nine peripheral doublet microtubules surround two single tubules. The doublet tubules contain an A tubule with 13 protofilaments and an incomplete B tubule with 10 – 11 protofilaments. The peripheral doublets connect to each other through nexin links and to the central tubules through radial spokes. An inner and outer dynein arm interacts with neighboring peripheral tubules.

In the classical 9+2 axoneme of motile cilia, the nine doublet microtubules on the periphery are each composed of a complete microtubule of 13 protofilaments (A tubule in Fig. 4-1) adjoined to an incomplete tubule of 10 - 11 protofilaments (B tubule of Fig. 4-1) (Cooper, 2000). The peripheral doublets connect to each other through the protein nexin, and connect to the two central tubules through radial spokes. The peripheral doublets interact through a motor protein, dynein, which has both inner and outer arms. Hydrolysis of ATP powers the dynein motors producing sliding between the microtubules. The relative sliding of the microtubules works against the nexin links and generates the force that propels the motile cilia (Cooper, 2000). Though kinocilia share a similar microtubule configuration with the motile cilia, they have been shown to lack the inner dynein arms (Kikuchi et al., 1989). The outer dynein arms were present in the kinocilia, but it is the inner arms which are essential for motility in cilia (Kikuchi et al., 1989).

The kinocilia and motile cilia are also similar in that both are anchored in a basal body (Cooper 2000, Flock and Duvall 1965). The basal body of the kinocilium is found just below the apical surface of the cell in a notch of the cuticular plate (Hillman 1969, Flock and Duvall, 1965). Unlike the stereocilia which insert into the rigid cuticular plate (Hillman, 1969), the kinocilium inserts into a more compliant material. However, the kinocilium remains upright even when the filamentous connections between it and neighboring stereocilia are broken. Even after separated kinocilia were pinned to the epithelial surface, they returned to an upright position within seconds of release (Hudspeth and Jacobs, 1979). This evidence indicates that the insertion of the kinocilium possess an inherent stiffness.

The purpose of this work is to measure the flexural rigidity of the kinocilia and the rotational stiffness of their insertions. Kinocilia derive their structural integrity from the microtubule core. The flexural rigidity (EI) of other cilia with a 9+2 axoneme has been measured in the past (Baba 1972, Okuno and Hiramoto 1979, Ishijima and Hiramoto 1994). The EI of the kinocilia has not been previously measured and is possibly different due to the lack of dynein arms. The rotational stiffness of the kinocilium about its apical insertion has not been previously measured.

4.2 Theory

Two mechanical properties of kinocilia were measured experimentally. These properties include the flexural rigidity (EI) of the kinocilium, measured with two separate techniques, and the rotational stiffness about its apical insertion. A force deflection technique was used to measure both the EI and rotational stiffness. Additionally, the EI was measured using high speed video to track the return of kinocilia following release from large deflections.

4.2.1 Flexural Rigidity

Flexural rigidity of a beam describes the beam's resistance to bending. It is the product of the Young's Modulus (E) of the material multiplied by the beams area moment of inertia (I). The flexural rigidity (EI) of a cantilever beam can be determined from its vertical deflection (δ) when a known force (F) is applied a distance L from the fixed end (Eq. 1). In this situation, δ is the vertical deflection of the beam at the position of force application (Fig. 4-2). Equation 1 applies when the EI is constant along the length of the beam and the end is fixed.

$$EI = \frac{FL^3}{3\delta} \tag{1}$$

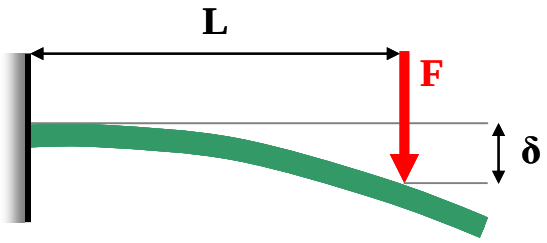

Figure 4-2. Cantilever Beam.
A cantilever beam with a force (F) applied at length (L) from the fixed end. The vertical deflection at the point of force application is represented by δ. To measure EI, the kinocilia were modeled as vertical cantilever beams with force applied a short distance from their tip.

In the first technique for measuring EI, the kinocilium was modeled as a vertically oriented cantilever beam. The base of the kinocilium was fixed at the height of the tallest stereocilia and a force was applied a short distance from the kinocilium tip. From measurements of the applied force, resulting tip deflections and height of force application, the EI of the kinocilium was determined through Eq. 1.

Modeling the kinocilium as a simple cantilevered beam makes the following assumption: the EI is constant along the kinocilium shaft and the kinocilium behaves as a linearly elastic, homogenous and isotropic material. Considering the 9+2 microtubule structure, it is reasonable to assume that the diameter of the kinocilium is uniform along its length and hence the moment of inertia is constant. However, the microtubular structure also means that the kinocilium is not homogenous and therefore the modulus is not constant at all points of a cross section. Consequently, we define an effective modulus for the cross section and assume that it does not change along the kinocilium shaft. It is currently not known to what extent the individual microtubules slide past one another during kinocilium bending. The likelihood of relative sliding between microtubules suggests the kinocilium does not behave as an isotropic material. In the past, a mathematical model of a single stereocilia investigated the impact of transversely isotropic properties on stereocilia deflection (Cotton and Grant, 2004). The study demonstrated that as stereocilia height is increased, the difference in tip deflections for anisotropic versus isotropic models decreased. For stereocilia heights greater than 10 μm, the isotropic model underestimated the tip deflection by less than 10%. Since the projection of the kinocilia above the tallest stereocilia in bundles examined in this study is generally greater than or equal to 10 μm, the assumption of an isotropic kinocilium employed here seems valid. Other investigators have modeled the kinocilium as an isotropic material (Silber et al., 2004, Nam et al., 2006).

4.2.2 Fluid Drag Formulation

In the second technique for measuring flexural rigidity, the kinocilium was again modeled as a vertically oriented cantilevered beam that was mechanically fixed at the height of the tallest stereocilia. A fluid drag formulation was used to express the motion

of a cylindrical beam moving through a fluid upon release from deflection. Again, the kinocilium is assumed to be an isotropic and homogenous material with a constant EI along the length.

Figure 4-3 illustrates a vertical cantilevered beam exposed to a triangularly distributed load. This is representative of the kinocilium upon release from deflection. As the kinocilium returns to equilibrium, fluid drag (D) produces the triangularly distributed load (ω) with a maximum load (ω_o) at the tip and zero load at the insertion. We assume that the velocity vectors are not perpendicular to the kinocilium during its return. The horizontal deflection of the beam (x) at any height (y) along its length (L) can be determined from Eq. 2. The displacement at the tip of the kinocilium (x_o) is expressed by Eq. 3.

$$x = \frac{\omega_o}{EI}\left(\frac{y^5}{120L} - \frac{Ly^3}{12} + \frac{L^2y^2}{6}\right) \tag{2}$$

$$x_o = \frac{11}{120}\frac{\omega_o L^4}{EI} \tag{3}$$

The fluid drag (D) on a cylinder is given by Eq. 4 where C_D is the drag coefficient, ρ is density, A is area, and υ is velocity. The drag coefficient was determined by Oseen's drag formulation for a cylinder (Schlichting 1968)(Eq. 5). In the Reynolds number (R_e) range of the kinocilium, the coefficient of drag was approximately equal to $6/R_e$. Substituting this drag coefficient into Eq. 4 and simplifying, yields an expression for the fluid drag (D) as a function of the fluid viscosity (μ), length of the cylinder (l) and velocity (dx/dt) (Eq. 6). The triangularly distributed load is equal to the fluid drag divided by length of the cylinder, and the maximum load at the tip of the kinocilium (ω_o) is given by Eq. 7. Velocity at the tip of the kinocilium is dx_o/dt, and the viscosity of water at 25° C was used (μ = 0.89 mPa·s). Inserting Eq. 7 into Eq. 3 and solving for the resulting differential equation for displacement at the tip, yields an exponential equation with a time constant (τ) given by Eq. 8. During an experiment, the kinocilium was

released from a deflected position and the displacement at the tip of the kinocilium was tracked using high speed video. The displacement data was normalized to the initial deflection and curve fit with an exponential function to determine a time constant. The EI was then determined by applying the experimentally measured time constant and kinocilium length to Eq. 8.

$$D = C_D \frac{1}{2} \rho A \upsilon^2 \tag{4}$$

$$C_D = \frac{8\pi}{R_e\left(\log \frac{7.4}{R_e}\right)} \tag{5}$$

$$D = 3\mu l \frac{dx}{dt} \tag{6}$$

$$\omega_o = 3\mu \frac{dx_o}{dt} \tag{7}$$

$$\tau = \frac{11}{40} \frac{\mu L^4}{EI} \tag{8}$$

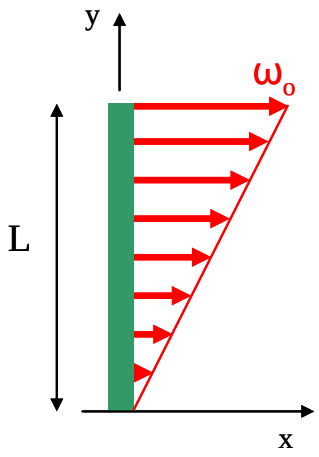

Figure 4-3. Triangularly distributed load on the kinocilium.
The kinocilium was modeled as a vertically oriented cantilevered beam. It was fixed at the height of the tallest stereocilia and the distance L projecting above the point of fixation. Upon release from deflection, fluid drag produced a triangularly distributed load with a maximum (ω_o) at the tip.

4.2.3 Rotational Stiffness

The stiffness of a rotational spring can be determined from its angular rotation due to an applied moment. Figure 4-4 illustrates a rigid bar pivoting about a rotational spring. For small angular deflections, the angle of rotation (θ) is approximately equivalent to the displacement at the tip of the bar (δ) divided by the bar's height (h). The stiffness of the rotational spring (κ) is then expressed through Eq 8. This approach has previously been used to determine the rotational stiffness of intact hair bundles (Crawford and Fettiplace, 1985, Howard and Ashmore, 1986)

$$\kappa = \frac{Fh^2}{\delta} \tag{8}$$

When the kinocilial links are broken through chemical treatment, kinocilia remain vertical though detached from the adjacent stereocilia. This suggests that the apical insertion of the kinocilia posses some inherent stiffness. When a detached kinocilium is deflected in the excitatory direction, it rotates about its insertion without bending. As a result, the kinocilium can be modeled as a rigid bar pivoting about a spring, and the rotational stiffness of the insertion can be determined through Eq. 8. It is assumed that the chemical treatment which severs the kinocilial links does not otherwise damage the kinocilia or the epithelium at the apical insertions.

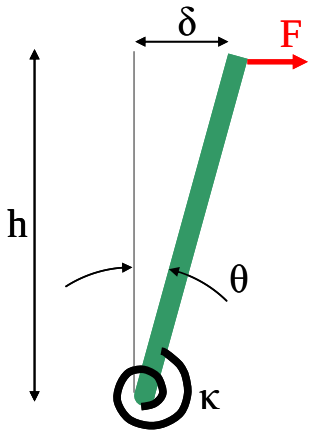

Figure 4-4. Rigid bar pivoting about a rotational spring. The kinocilium, detached from the neighboring stereocilia, behaved as a rigid bar rotating about its apical insertion. The rotational stiffness (κ) of the spring is defined by Eq. 2, for small angles of θ.

4.3 Methods

Turtle utricles were prepared and maintained as described in the methods of chapter 2. The utricles were folded along a medial to lateral transect and the otoconial membrane was peeled away. Bundles along the folded edge were viewed from the side using a Zeiss Axioskop with 100X water immersion objective and 10X oculars.

Measurements of the kinocilia properties were made from hair bundles located in the medial extrastriola of the turtle utricle. The kinocilia in this region are very tall (10 – 40+ μm) and the stereocilia are short (2 -5 μm). The portion of the kinocilium projecting above the tallest stereocilia was used to measure the flexural rigidity. The kinocilium was detached from the adjacent stereocilia, and the whole length was used for measurements of the rotational stiffness about its insertion.

4.3.1 Supporting the Kinocilium for Flexural Rigidity Measurements

For measurements of the flexural rigidity, the base of the kinocilium was backed up with a rigid glass probe mechanically fixing it between the bundle and the probe (Fig. 4-5). The supporting probe was fabricated from a solid pipette pulled and trimmed to have a flat end of 5 μm in diameter. The glass probe was positioned with its top edge at the height of the tallest stereocilia so that when the kinocilium was deflected in the excitatory direction, the exposed portion bent in flexure.

4.3.2 Separating the Kinocilium for Rotational Stiffness Measurements

To separate the kinocilia from the adjacent stereocilia, the bundles were exposed to the calcium chelator BAPTA (1,2-bis(2-Aminophenoxy)ethane-N,N,N',N'-tetraacetic acid tetrasodium salt, Sigma-Aldrich). BAPTA has been shown to sever kinocilial links in chick utricular bundles (Goodyear and Richardson 2003). A 5 mM solution of BAPTA was prepared in Ca^{2+} and Mg^{2+} free Hanks' Balanced Salt Solution with 0.9 mM $MgCl_2$ and 10mM HEPES added (HBSS: no phenol red, 5.33 mM KCl, 0.441 mM KH_2PO_4, 4.17 mM $NaHCO_3$, 137.93 mM NaCl, 0.338 mM Na_2HPO_4, 5.56 mM D-

Glucose, pH 7.2, 300 mOsm). The BAPTA solution was prepared in plastic containers hours before use and was protected from light.

To apply the treatment, a peristaltic pump was used to exchange the solution in the experimental chamber with the BAPTA treatments. Three times the volume of the experimental chamber was pumped through to ensure the treatment was not diluted due to mixing. After at least 10 minutes of BAPTA exposure, the force deflection measurements on the separated kinocilia were begun. Figure 4-6 demonstrates that the kinocilia fully detached and rigidly rotated about their insertions for large displacements. Note that the displacements of the kinocilium during actual measurements were much smaller (< 1 μm) than shown in the photograph. The angular displacements (≤0.09 rad) complied with the small angle approximation applied to obtain Eq. 8.

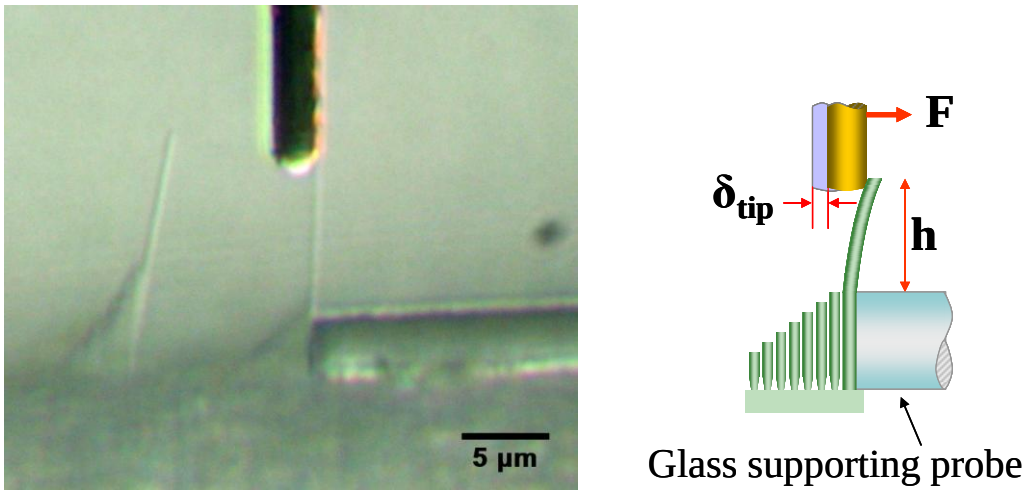

Figure 4-5. A supported kinocilium for flexural rigidity measurements.
Bundles were backed up with a supporting probe to fix the kinocilia at the height of the tallest stereocilia. When pushed in the excitatory direction with a flexible glass fiber, the exposed portion of the kinocilia bent in flexure. Measurements of the applied force (F), tip deflection of the kinocilium (δ_{tip}), and height projecting above the supporting probe (h) were used to calculate the flexural rigidity. The supporting probe was also used in the high speed video technique for measuring flexural rigidity.

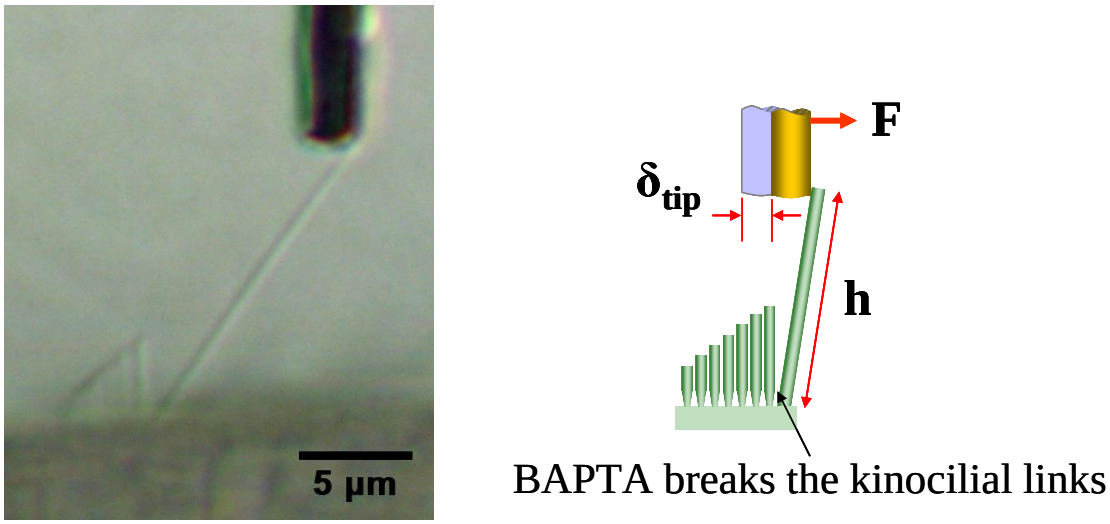

Figure 4-6. Detached kinocilium for rotational stiffness measurements.
Exposure to BAPTA broke the kinocilial links and separated the kinocilia from the neighboring stereocilia. During large deflections in the excitatory direction, the kinocilia showed no indications of bending. Instead, the kinocilia rotated about their insertions while remaining rigid. A force (F) was applied to the tip of the kinocilium with a flexible glass fiber (illustrated as a gold cylinder). Rotational stiffness was determined from the applied force and measurements of the kinocilium's tip deflection (δ_{tip}) and height (h).

4.3.3 Force Deflection Technique

For measurements of both EI and rotational stiffness, kinocilium were deflected in their excitatory directions with flexible glass fibers. The fibers were made from solid borosilicate glass rods using a microforge. The fibers were drawn perpendicular to the shank of the rod by quickly retracting a platinum heating element. The fibers had tip diameters of 2.9 – 4.2 µm, were trimmed to lengths of 2.8 – 3.5 mm, and were sputter coated with 200 Å of gold to improve their optical contrast. The stiffness of the fibers were determined by measuring the deflection of a horizontally position fiber when micro beads, 30-100 µm, were statically attached to the free end. From the bead properties, fiber length, and vertical deflection, the stiffness was determined with a cantilever beam equation. The fibers used had stiffness values of 7.6 - 24.5 µN/m.

The free end of a flexible glass fiber was brought into contact with the tip of the kinocilium such that their shafts were parallel (Fig. 4-7). The base of the fiber was displaced using a piezoelectric linear actuator, and measured using a fiber optic

displacement sensor (EFPI: extrinsic Fabry-Perot interferometer, Luna Innovations, Blacksburg, VA). Deflections at the tip of the glass fiber, in contact with the kinocilium, were measured with a dual array of photodiodes located at the camera port of the microscope (Fig. 4-7). The force applied to the kinocilium by the glass fiber was quantified by multiplying the fiber stiffness by the difference between the fiber's base and tip deflections.

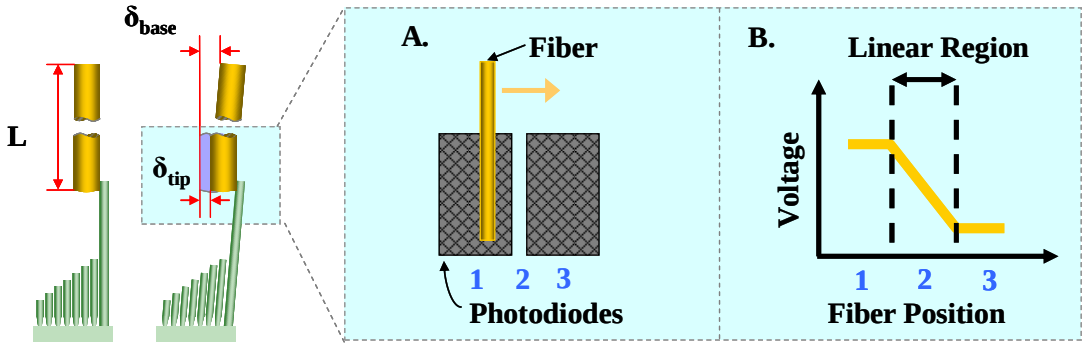

Figure 4-7. Force deflection technique incorporating dual photodiodes.
A flexible glass fiber of known stiffness is used to deflect the tip of the kinocilium. A dual array of photodiodes, positioned at the camera port of the microscope, measures the displacement of the fiber tip. **A.** Movement of the glass fiber changes the distribution of light on the photodiodes. **B.** As the whisker passes between the two diodes, the diode output voltage is linearly related to whisker position.

With the fiber contacting the tip of kinocilium, the base of the glass fiber was sinusoidally oscillated a peak-to-peak distance of 1 μm at 0.5 Hz. Signals from the EFPI and photodiodes were recorded for 30 sec. trials at a sampling frequency of 1 kHz with LabVIEW 7.0 (National Instruments). The photodiodes were calibrated at the end of each trial by positioning the oscillating fiber just above the kinocilium in the same horizontal plane. Again, the EFPI and photodiode outputs were recorded in 30 sec. trials. This was used to determine a calibration factor relating photodiode output voltage to displacements of the fiber tip.

The force applied to the kinocilium was determined from the peak-to-peak base and tip deflections of each oscillation and averaged per trial. The reported EI and rotational stiffness measurements are the averages of multiple trials. Kinocilia heights

for these calculations were measured from high resolution digital photographs using Image J software (NIH, public domain).

To ensure contact between the kinocilium and the glass fiber, the fiber was positioned 1-3 μm from the kinocilium's tip. This technique gives rise to several potential loading conditions of the kinocilium depending on the mode of contact between the two shafts during deflections. It is possible that a point load was transferred to the kinocilium from the tip of the glass fiber. Another possibility is that a triangular load was distributed along the entire distance between the kinocilium and fiber tips. Even at 1000X magnification, the actual loading condition could not be visually discerned. To examine the effect of different loading conditions, a finite element model of a medial extrastriolar bundle from a red-eared slider turtle was employed (Silber et al., 2004, Nam et al., 2006). A point load at 2 μm and triangular loads distributed over 1 and 2 μm were applied to the tip of the kinocilium. The results demonstrated that there was very little difference (8%) in kinocilium tip deflection between the extreme forcing conditions (Fig. 4-8). Consequently, we chose to incorporate a point loading condition for the EI and rotational stiffness calculations. The point load is believed to be the most likely situation, and it is also slightly less complex to implement. During measurements, a reticule with divisions equivalent to 1 μm was used to measure the distance of the fiber's tip from that of the kinocilium for each trial. This distance was subtracted from the kinocilium length prior to calculations with Eq. 1 and 2.

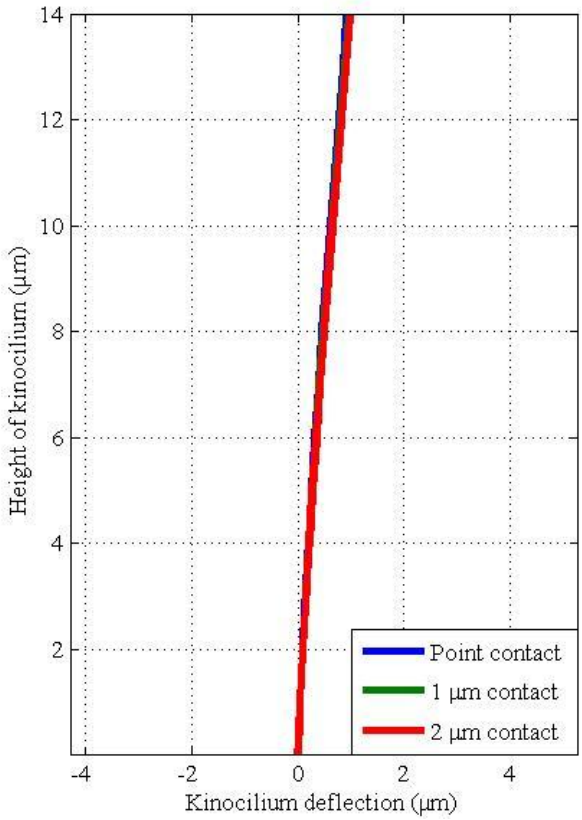

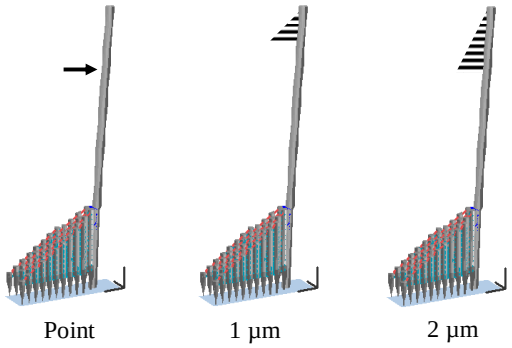

Figure 4-8. Effect of kinocilium loading condition.
A finite element model of a medial extrastriola hair cell was used to investigate 3 forcing conditions: a point load 2 µm from the kinocilium tip and triangularly distributed loads over 1 and 2 µm from the tip (distance from the tip is exaggerated in the illustrations). The impact of the loading conditions on the kinocilium tip deflection was minimal.

4.3.4 High Speed Video Technique

A high speed digital camera (AxioCam HSm, Zeiss) was used to capture video of kinocilia following release from large deflections. With the supporting probe in place, the kinocilium was deflected with a glass fiber. The kinocilium was pushed in the excitatory direction until contact with the glass fiber was lost. The maximum deflections ranged from 1 to 13 µm.

Monochrome video was taken of the kinocilium's return to equilibrium at rates of approximately 7 ms/frame (143 frames/sec) (Fig. 4-9). The video acquisition speed was increased through two means: restricting the field of view and incorporating binning. The field of view was slightly greater than the height of the kinocilium. Thus, the entire bundle was imaged to visually ensure the base of the kinocilium was fixed by the supporting probe. Binning is a process which combines adjacent pixels on the camera's

sensor to improve the speed of data transfer. It increases the speed of the video but slightly decreases the spatial resolution of the image. For these tests, 2 x 2 binning was used which essentially combines four adjacent pixels into one. This binning level provided adequate speed with enough resolution to clearly detect the edge of the kinocilium during motion. With binning, the spatial resolution of the video was 198 nm/pixel.

Video of the kinocilium's return to equilibrium was analyzed using Axiovision software (release 4.6, Carl Zeiss). A particle tracking feature enabled manual frame-by-frame tracking of the kinocilium position. The kinocilium was tracked several microns (2-5 μm) from the tip to avoid visual interference from the glass fiber. The tracking height and the height of the kinocilium projecting above the supporting probe were measured in Axiovision. The equations presented in the theory section were adjusted to account for the height at which the kinocilium was tracked.

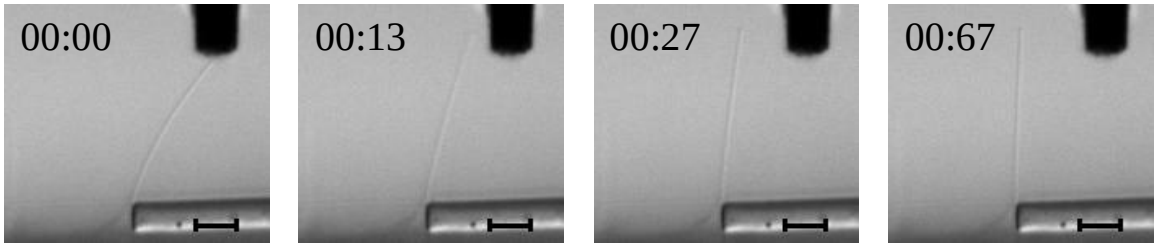

Figure 4-9. Kinocilium return to equilibrium.
While backed up with a supporting probe, the kinocilium was displaced in the excitatory direction and released. Four frames from a high speed video of the kinocilium's return to equilibrium are shown. The frame rate of this particular video was 6.7 sec/frame. The Time stamps in the upper left of the images are in ms (seconds:milliseconds). The scale bars represent 5 μm.

4.4 Results

4.4.1 Verification of High Speed Video Technique

The high speed video technique incorporating the fluid drag formulation was validated by measuring the EI of glass fibers with constant diameters. Because the Young's modulus (E) is known and the diameters (d) measurable, the EI of the glass fibers was easily calculated (Eq. 3). The measured and calculated values were compared to determine the accuracy of the high speed video technique.

$$EI = E\frac{\pi d^4}{64} \tag{3}$$

Glass fibers with constant diameters of several microns are difficult to obtain. The techniques for pulling glass fibers used in our laboratory were insufficient at producing fibers of constant diameter. The best source we found for appropriately sized fibers of approximately constant diameter proved to be fiberglass insulation. The insulation was soaked in acetone to dissolve the pink coating, and glass fibers were extracted. The fibers were glued orthogonally to glass pipettes and trimmed. Diameter was measured in 1 mm increments along the length of the fibers and averaged for use in the EI calculations. There were small variations in the diameter of each fiber with the maximum standard deviation reaching ±0.34 μm. The Young's modulus for general purpose E-glass fibers, like those used in fiber glass insulation, is 76-78 GPa (Wallenberger and Watson, 2001). A modulus of 77 GPa was used in our EI calculations. The EI of the glass fibers was experimentally measured using the same procedure described for the kinocilium. Young's modulus was also calculated as the measured EI divided by the moment of inertia determined from the measured diameter. The calculated Young's modulus was compared with the known value for glass.

The results demonstrated that the high speed video technique for measuring EI is reasonably accurate (Table 4-1). For the two fibers tested, the percent difference between calculate and measured values of EI were 1.5 – 18.6%.

	Fiber 1	Fiber 2
Dimensions		
Diameter (μm)	9.22 ± 0.34 (8)	10.13 ± 0.24 (5)
Length (mm)	5.91± 0.10 (3)	4.50 ± 0.01 (3)
Flexural Rigidity ($N \cdot \mu m^2$)		
Calculated	27.3	39.8
Measured	27.7 ± 3.5 (7)	32.4 ± 4.0 (15)
% difference	1.5	18.6
Young's Modulus (GPa)		
Known	77	77
Calculated from measured EI	78.2 ± 9.9	62.8 ± 7.7

Table 4-1. Measured and calculated properties of constant diameter glass fibers.
Two fibers of approximately constant diameter were extracted from fiber glass insulation. Their EI was calculated from the measured diameter and known modulus of glass (77 GPa). EI was also measured using the high speed video technique. The percent difference of the measured value from the calculated value is given. Young's modulus was calculated by dividing the measured EI with the moment of inertia determined from the measured fiber diameters.

4.4.2 Properties of the Kinocilium

The measured values of the kinocilia flexural rigidity and the rotational stiffness are presented in Table 4-2. Using the force-deflection technique, the average flexural rigidity measured from 11 kinocilia was 2580 ± 670 pN·μm^2. The average flexural rigidity of 13 kinocilia measured from the high speed video technique was slightly higher at 3510 ± 1310 pN·μm^2. The two techniques for measuring flexural rigidity yielded comparable results. Measurements with high speed video demonstrated larger variance which is attributed to the wide range of kinocilia heights examined with this approach (discussed further below). Rotational stiffness of the kinocilia about their apical insertion was measured for 5 kinocilia giving an average value of 120 ± 17 pN·μm/rad. As shown in Fig. 4-6, the kinocilia remained rigid while pivoting about their insertions. Following large deflection, the detached kinocilium snapped back to an upright position.

Occasionally, an unusual kinking behavior was observed for large deflections of the kinocilium. When large deflections were applied to a kinocilium several microns from its tip, the kinocilium sometimes bent so that the upper section was parallel to the epithelium. The upper portion remained horizontal but shortened as the kink propagated to the tip of kinocilium. The tip of the kinocilium did not traverse a radial arc as the shaft returned to equilibrium.

	avg ± std dev (n)	**range**
Flexural Rigidity (pN·μm^2)		
Force-deflection	2580 ± 670 (n=11)	1470 - 3490
High speed video	3510 ± 1310 (n=13)	1460 - 6150
Rotational Stiffness (pN·μm/rad)		
Force-deflection	120 ± 17 (n=5)	106 - 150

Table 4-2. Measured mechanical properties of the kinocilium.
Results are given as the mean ± standard deviation (number of samples). The flexural rigidity of the kinocilium measured through two techniques yielded comparable results. The rotational stiffness of the kinocilium about its apical insertion was measured through a single force deflection technique.

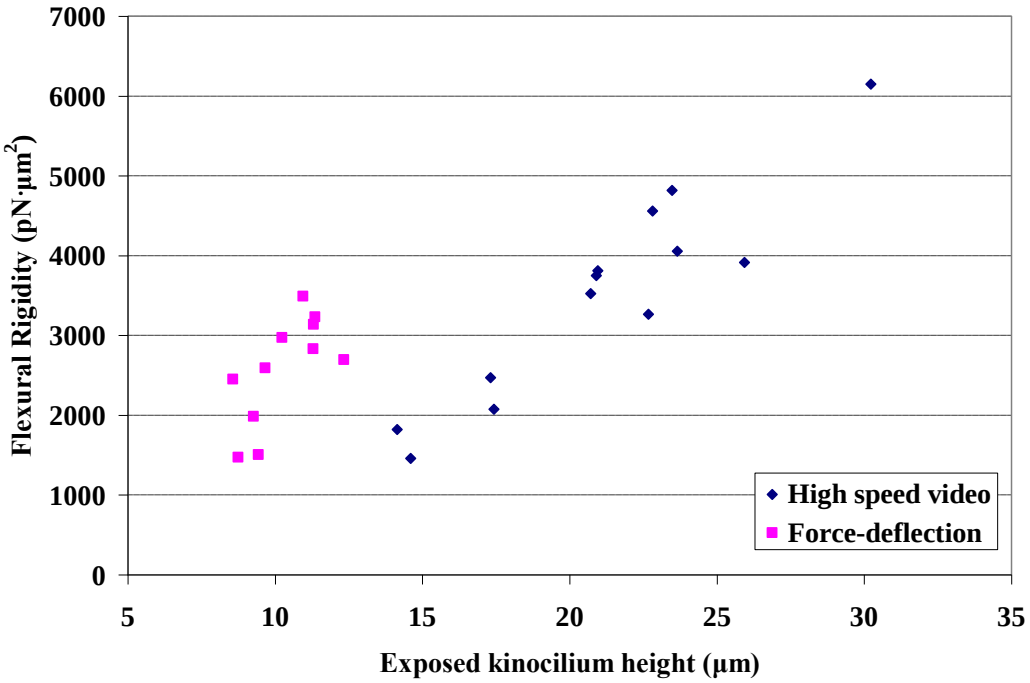

Figure 4-10. Measured flexural rigidity vs. kinocilium height.
The measured values of flexural rigidity were dependent on the kinocilium height. Both techniques of measuring EI demonstrated an increase in EI with increasing kinocilium height. Exposed kinocilium height is the length of the kinocilium projecting above the tallest stereocilia.

4.5 Discussion

In theory, a homogenous beam with isotropic material properties and constant cross sectional area should have the same EI regardless of its length. We expected the kinocilium to demonstrated similar behavior. However, measurements of EI were found to increase with the height of the kinocilium (Fig.4-10). Two possible explanations for the observed dependence are 1) that assumptions regarding the isotropy and homogeneity of the kinocilium introduced an error or 2) the structure of kinocilia vary with height.

As discussed earlier, the kinocilium is not a homogenous material and likely demonstrates anisotropic behavior due to sliding of the microtubules. A computational model of a single stereocilia demonstrated that for heights greater than 10 μm, tip deflection was 10% greater with transversely isotropic as opposed to isotropic properties

(Cotton and Grant, 2004). Our measurements were made on kinocilia ranging in height from 8.6 to 30.2 μm suggesting that isotropy was a reasonable assumption. A 10% alteration in measured tip deflection does not account for the ~4500 $pN \cdot \mu m^2$ range in EI measured experimentally.

If the observed EI dependence on height is correct, it suggests that either the moment of inertia (ie., the diameter) or the effective modulus is greater for tall kinocilium. Since the microtubules provide the structural integrity of the kinocilium, EI dependence on height suggests the structure of the axoneme might change along the length of a kinocilium or between kinocilia of different heights. This might be observed if the spacing, inter connections, or consistency of the microtubules varied with kinocilium height. These suggestions, however, are mostly speculative. There is no reported observations of variations in spacing or inter connections between the microtubules along the height of the kinocilium, but this has not been specifically measured. There is some evidence that the central pair of tubules do not extend the entire length of the kinocilium. This was observed in the vestibular hair cells of squirrel monkeys (Engstrom et al., 1972), and suggested from inconsistent or incomplete central tubules observed in the guinea pig utricle and mouse (Kikuchi et al., 1989, Kikuchi et al., 1988). Other work has shown that the central pair exist the entire length of the kinocilia in pigeon (Smith and Takasaka, 1971). The nine peripheral doublet tubules are consistently observed in vestibular kinocilia across species. These outer tubules are the major contributors to the flexural rigidity of the kinocilium, and alteration in their spacing would impact the EI. An increase in the doublet spacing would increase both kinocilium diameter and EI. This raises the question as to whether taller kinocilia might have larger diameters. This is something which has not been investigated to date, but could reasonable explain the experimentally observed dependence of EI on height.

From the DIC light microscope images, measurements of the kinocilia diameter in the turtle utricle were ~ 700-800 nm. The resolution was not sufficient for highly accurate measurements of diameter or changes in diameter along the length. Kinocilium diameters measured from transmission electron micrographs were reported as 350 nm in turtles (Silber et al., 2004). The turtle kinocilium has a 9+2 axoneme (unpublished, Dr. Peterson), but the consistency of the two central tubules along the kinocilium's length

and the spacing of the microtubules has not been specifically examined. At this point, an axial variation in the structure of the kinocilium can not be ruled out. If present, our data suggests that the variation would effectively increase the rigidity of taller kinocilia.

4.5.1 Comparison with Motile Cilia

Measurements have been made on the sperm flagellum of echinoderms including the star fish, sea urchin, and sand dollar (Okuno and Hiramoto 1979, Ishijima and Hiramoto 1994). The echinoderm sperm flagellum has the basic 9+2 microtuble arrangement commonly found in the kinocilium, though they differ by the presence of inner dynein arms which are integral for motility (Okuno and Hiramoto, 1979, Kikuchi et al., 1989, Cooper 2000). These particular flagellum provide a good comparison for the kinocilia because they lack course fibers that are observed in other flagellum (ex. bull sperm flagellum) which likely influence the stiffness (Okuno and Hiramoto, 1979). In one study, live echinoderm flagella were immobilized with CO_2 saturated medium. Using a flexible glass microneedle the EI was measured as 300 – 1500 $pN \cdot \mu m^2$ (Okuno and Hiramoto, 1979). Interestingly, they determined that the stiffness was uniform along the shaft except in a particular plane of bending. Within this particular plane, flexible regions were observed in ~ 10 – 15 μm intervals along the flagellum shaft that were 0.2 - 0.3 times the stiffness of the other regions (Okuno Hiramoto, 1979). This observation of weaker regions is further evidence that there are structural inconsistencies along the axoneme and may explain the occasional kinking behavior observed in the kinocilium.

Later measurements of live echinoderm sperm flagellum immobilized with CO_2 were much higher at 11,000 $pN \cdot \mu m^2$ (Ishijima and Hiramoto 1994). However, the authors cited that the sudden exposure to medium lacking CO_2 may have induced a state of "rigor" effectively increasing the EI. They also examined beating flagellum and found that the EI was 14 – 15 times greater in the plane perpendicular rather than parallel to the beating plane. Beating flagellum had an in plane EI of 420 $pN \cdot \mu m^2$ compared to 5800 $pN \cdot \mu m^2$ perpendicular to the beating plane. The authors suggested that the lower EI was attributable to a reduction in the quantity of dynein cross bridges parallel to the beating

plane. The work also demonstrated that trypsin digestion of the radial spokes and nexin connections scarcely affected the flexural rigidity.

4.5.2 Comparison of the High Speed Video and Force Deflection Techniques

The two techniques for measuring flexural rigidity yielded very similar results. In addition, the high speed video technique accurately measured the EI of constant diameter glass fibers. Kinocilia measured with the force deflection technique ranged in height from 8.6 – 12.3 μm. In comparison, the kinocilia investigated with high speed video were taller and spanned a lager range of heights, 14.1 – 30.2 μm. The high speed video technique demonstrated a greater variance in EI measurements than the force-deflection technique. In light of the observed EI dependence on kinocilium height, the larger variance is likely attributable to the wider range of kinocilium heights measured with the high speed video technique.

4.6 Conclusions

The flexural rigidity of motile cilia reported in literature are comparable with the values measured for the kinocilium. Measurements of the kinocilium EI ranged from 1460 – 6150 $pN \cdot \mu m^2$ while those reported in literature for the sperm flagellum ranged from 300 – 11,000 $pN \cdot \mu m^2$ for various conditions. The rotational stiffness of the kinocilium about its insertion has not previously been reported, and there is no data available for comparison. The evidence that the kinocilium did not bend when detached from the neighboring stereocilia suggests that a rigid bar pivoting about a rotational spring is an appropriate model of the detached kinocilium. Overall, we conclude that these measurements provide a reasonable first estimate of the flexural rigidity of the kinocilia and the rotational stiffness about their insertions.

References

Ashmore, J.F. The stiffness of the sensory hair bundle of frog saccular hair cells. *Journal of Physiology* 350(suppl):20P, 1984.

Assad, J.A., Shepherd, G.M.G., and Corey, D.A. Tip-link integrity and mechanical transduction in vertebrate hair cells. *Neuron* 7: 985-994, 1991.

Baba, S.A. Flexural rigidity and elastic constant of cilia. *Journal of Experimental Biology* 56: 459-467, 1972.

Bagger-Sjöbäck, D. and Takumida, M. Geometrical array of the vestibular sensory hair bundle. *Acta Otolaryngology(Stockh)* 106: 393-403, 1988.

Bashtanov, M.E., Goodyear, R.J., Richardson , G.P., and Russell, I.J. The mechanical properties of chick (Gallus domesticsu) sensory hair bundles: relative contributions of structures sensitive to calcium chelation and subtilisin treatment. *Journal of Physiology* 559.1: 287-299, 2004.

Cooper, G.M. The Cell. 2nd ed., Wahinsgton, D.C., ASM Press, 2000.

Cotton, J. and Grant W. Computational models of hair cell bundle mechanics: I. Single stereocilium. *Hearing Research*. 197: 96-104, 2004.

Crawford, A.C., and Fettiplace, R. The mechanical properties of ciliary bundle of turtle cochlear hair cells. *Journal Physilogy* 364: 359-379, 1985.

Crawford, A.C., Evans, M.G., and Fettiplace, R. The actions of calcium on the mechano-electrical transducer current of turtle hair cells. *Journal of Physilogoy* 434: 369-398, 1991.

Denk, W., Webb, W.W., and Hudspeth, A.J. Mechanical properties of sensory hair bundles are reflected in their Brownian motion measured with a laser differential interferometer. *Proceedings of the National Academy of Sciences USA* 86: 5371 – 5375, 1989.

Engström, H., Bergström, B., and Ades, H.W. Macula utriculi and macula sacculi in the squirrel monkey. *Acta Otoloaryngology Suppl* 301: 75-126, 1972.

Flock, A. and Duvall, A. The ultrastructure of the kinocilium of the sensory cells in the inner ear and lateral line organs. *The Journal of Cell Biology*. 25: 1-8, 1965.

Fontilla, M.F. and Peterson, E.H. Kinocilia heights on utricular hair cells. *Hearing Research* 145: 8-16, 2000.

Géléoc, G.S.C., Lennan, G.W.T., Richardson, G.P., and Kros, C.J. A quantitative comparison of mechanoelectrical transduction in vestibular and auditory hair cells of neonatal mice. *Proceeding of the Royal Society B* 264:611-621, 1997.

Goodyear, R. and Richardson, G.P. Distribution of the 215 kD hair cell antigen and cell surface specializations on auditory and vestibular hair bundles in the chicken inner ear. *The Journal of Comparative Neurology* 325: 243-256, 1992.

Goodyear, R. and Richardson, G.P. The ankle-link antigen: an epitope sensitive to calcium chelation associated with the hair-cell surface and the calycal processes of photoreceptors. *The Journal of Neuroscience* 19(10): 3761-3772, 1999.

Goodyear, R.J. and Richardson, G.P. A novel antigen sensitive to calcium chelation that is associated with the tip links and kinocilial links of sensory hair bundles. *The Journal of Neuroscience* 23(12): 4878-4887, 2003.

Goodyear, R.J., Marcotti, W., Kros, C.J., and Richardson, G.P. Development and properties of stereociliary link types in hair cells of the mouse cochlea. *The Journal of Comparitive Neurology* 485: 75-85, 2005.

Goodyear, R.J., Kros, C.J., and Richardson, G.P. The structure and composition of the stereociliary bundle of vertebrate hair cells. Vertebrate Hair Cells. ed. Eatock, R.A., Fay, R.R., and Popper, A.N. Springer Handbook of Auditory Research 27: 20-94, 2006.

Grant, W., Spoon, C., and Nam J-H. Experimental and computational analysis of hair bundle mechanics at different macular location in the turtle utricle. *Association of Research in Otolaryngology* 736, 2007.

Hackney, C.M., Fettiplace, R., and Furness, D.N. The functional morphology of stereociliary bundles on turtle cochlear hair cells. *Hearing Research* 69: 163-175, (1993).

Hillman, D.E. New ultrastructural findings regarding a vestibular ciliary apparatus and its possible functional significance. *Brain Research* 13: 407-412, 1969.

Hillman, D.E. Morphology of peripheral and central vestibular systems. Frog Neurobiology: A Handbook. Springer-Verlag, Berlin ed. R.Llinás, W. Precht,1976

Howard, J. and Ashmore, J.F. Stiffness of sensory hair bundles in the sacculus of the frog. *Hearing Research* 23: 93-104, 1986.

Howard, J. and Hudspeth, A.J. Mechanical relaxation of the hair bundle mediates adaptation in mechanoelectrical transduction by the bullfrog's saccular hair cell. *Proceedings of the National Academy of Sciences USA* 84: 3064-3068, 1987.

Howard, J. and Hudspeth, A.J. Compliance of the hair bundle associated with gating of mechanoelectrical transduction channels in the bullfrog's saccular hair cell. *Neuron* 1:189-199, 1988.

Hudspeth, A.J., and Jacobs, R., Stereocilia mediate transduction in vertebrate hair cells. *Proceedings of the National Academy of Sciences USA* 76(3): 1506-1509, 1979.

Ishijima, S. and Hiramoto, Y. Flexural rigidity of echinoderm sperm flagella. *Cell Structure and Function*, 19: 349-362, 1994.

Jacobs, R.A. and Hudspeth, A.J. Ultrastructural Correlates of Mechanoelectrical Transduction in Hair Cells of the Bullfrog's Internal Ear. *Cold Spring Harbor Symposium on Quantitative Biology*, LV: 547-561, 1990.

Jaramillo, F. and Hudspeth, A.J. Displacement –clamp measurements of the forces exerted by gating springs in the hair bundle. *Proceedings of the National Academy of Sciences USA* 90: 1330-1334, 1993.

Jorgensen, J.M. The sensory epithelia of the inner ear of two turtles, testudo graeca L. and Pseudemys scripta (Schoepff). *Acta Zoologica* 55: 289-298, 1974.

Jorgensen, J.M. The number and distribution of calyceal hair cells in the inner ear utricular macula of some reptiles. *Acta Zoologica* 69(3):169-175, 1988.

Kikuchi, T., Tonosaki, A., and Takasaka, A. Development of apical surface structures of mouse otic placode. *Acta Otolaryngology* 106: 200-207, 1988.

Kikuchi T., Takasaka, T., Tonosaki, A., and Watanabe, H. Fine structure of guinea pig vestibular kinocilium. *Acta Otolaryngology* 108: 26-30, 1989.

Kössl, M., Richardson, G.P., and Russell, I.J. Stereocilia bundle stiffness: Effects of neomycin sulphate, Q23187 and Concanavalin A. *Hearing Research* 44:217-230, 1990.

Langer, M.G., Fink, S., Koitschev, A., Rexhausen, U., Heinrich Hörber, J.K., and Ruppersberg, J.P. Lateral mechanical coupling of stereocilia in cochlear hair bundles. *Biophysical Journal* 80: 2608-2621, 2001.

Lewis, E.R., Leverenz, E.L., and Bialek, W.S. The Vertebrate Inner Ear. Boca Raton, CRC Press Inc., 1985.

Lewis, E.R., and Li, C.W. Evidence concerning the morphogenesis of saccular receptors in the bullfrog (Rana catesbeiana). *Journal of Morphology* 139: 351-361, 1973.

Lewis, E.R., and Li, C.W. Hair cell types and distributions in the otolithic and auditory organs of the bullfrog. *Brain Research* 83: 35-50, 1975.

Merkle, A.C. Implementation of photoelectronic motion transducer for measuring sub-micrometer displacements of vestibular bundles. Virginia Tech Thesis, 2000.

Marquis, R.E. and Hudspeth, A.J. Effects of extracellular Ca^{2+} concentration on hair-bundle stiffness and gating-spring integrity in hair cells. *Proceedings of the National Academy of Sciences USA* 94: 11923-11928, 1997.

Moravec, W.J. and Peterson, E.H. Differences between stereocilia numbers on type I and type II vestibular hair cells. *Journal of Neurophysiolgy* 92: 3153-3160, 2004.

Nam, J-H., Cotton, J.R., Peterson, E.H. and Grant W. Mechanical properties and consequences of stereocilia and extracellular links in vestibular hair bundles. *Biophysics Journal* 90: 2786-2795, 2006.

Okuno, M. and Hiramoto, Y. Direct measurements of the stiffness of echinoderm sperm flagella. *Journal of Experimental Biology* 79: 235-243, 1979.

Ricci, A.J., Crawford, A.C., and Fettiplace, R. Active hair bundle motion linked to fast transducer adaptation in auditory hair cells. *The Journal of Neuroscience* 20(19): 7131-7142, 2000.

Ricci, A.J., Crawford, A.C., and Fettiplace, R. Mechanisms of active hair bundle motion in auditory hair cells. *The Journal of Neuroscience* 22(1): 44-52, 2002.

Rowe, M.H. and Peterson, E.H. Quantitative analysis of stereociliary arrays on vestibular hair cells. *Hearing Research*, 190: 10-24, 2004.

Rowe, M.H. and Peterson, E.H. Autocorrelation analysis of hair bundle structure in the utricle. *Journal of Neurophysiology* 96: 2653-2669, 2006.

Russell, I.J., Kössl, M., and Richardson, G.P. Nonlinear mechanical responses of mouse cochlear hair bundles. *Proceeding of the Royal Society B* 250: 217-227, 1992.

Schlichting, H. Boundary-Layer Theory. 6^{th} ed. New York, McGraw-Hill Book Co., 1969.

Severinsen, S.A., Jorgensen, J.M., and Nyengaard, J.R.. Structure and growth of the utricular macula in the inner ear of the slider turtle Trachemys scripta. *Journal of the Association for Research in Otolaryngology* 4: 505-520, 2003.

Shi, X., Gillespie, P.G., and Nuttall, A.L. Na^{+} influx triggers bleb formation on inner hair cells. *American Journal of Physiology – Cell Physiology* 288: C1332-C1341, 2005.

Silber, J., Cotton, J., Nam, J-H., Peterson, E.H., and Grant W. Computational models of hair cell bundle mechanics: III. 3-D utricular bundles. *Hearing Research* 197: 112-130, 2004.

Smith, C.A. and Takasaka, T. Auditory receptor organs in reptiles, birds, and mammals. Contributions to Sensory Physiology, New York: Academic, ed. Neff, W.D., 5: 129-178, 1971.

Sobkowicz, H.M., Slapnick, S.M., and August, B.K. The kinocilium of auditory hair cells and evidence for its morphogenetic role during the regeneration of stereocilia and cuticular plates. *Journal of Neurocytology* 24: 633-653, 1995.

Strelioff, D. and Flock, A. Stiffness of sensory-cell hair bundles in the isolated guinea pig cochlea. *Hearing Research* 15: 19-28, 1984.

Szymko, Y.M., Dimitri, P.S., and Saunders, J.C. Stiffness of hair bundles in the chick cochlea. *Hearing Research* 59: 241-249, 1992.

Wallenberger, F.T., Watson, J.C., and Hong, L. Glass Fibers. ASM Handbook, Vol. 21: Composites, 2001.

Wersäll, J. and Bagger-Sjöbäck, D. Morphology of the vestibular sense organ. Vestibular System Part 1: Basic Mechanisms. ed. Autrum H., Jung, R., Lowenstein, W.R., Mackay, D.M., and Teuber, H.L. Handbook of Sensory Physiology VI/I: 124-170, 1974.

Xue, J. and Peterson, E.H. Spatial patterns in the structure of the otolithic membranes. *Abstract Association of Research in Otolaryngology* 1523, 2003.

Xue, J. and Peterson, E.H. Differences between hair bundles of type I hair cells in turtle utricle. *Abstract Association of Research in Otolaryngology* 1036, 2005.

Xue, J. and Peterson, E.H. Hair bundle heights in the utricle: Differences between macular locations and hair cell types. *Journal of Neurophysiology* 95: 171-186, 2006.